THESIS FOR THE DEGREE OF DOCTOR OF PHILOSOPHY

Studies of Molecular Interactions with Single Nanoparticles

Combining in Situ Plasmonic Nanospectroscopy with Transmission Electron Microscopy

SARA NILSSON

Department of Physics

CHALMERS UNIVERSITY OF TECHNOLOGY

Gothenburg, Sweden 2021

Studies of Molecular Interactions with Single Nanoparticles

Combining in Situ Plasmonic Nanospectroscopy with Transmission Electron Microscopy

SARA NILSSON

ISBN 978-91-7905-489-2

Doktorsavhandlingar vid Chalmers tekniska högskola

Ny serie nr 4956

ISSN 0346-718X

Department of Physics

Chalmers University of Technology

SE-412 96 Gothenburg

Sweden

Telephone + 46 (0)31-772 1000

Cover: An artistic illustration of carbon monoxide oxidation over an array of individually different copper nanoparticles.

Chalmers Digitaltryck

Gothenburg, Sweden 2021

Studies of Molecular Interactions with Single Nanoparticles – Combining in Situ Plasmonic Nanospectroscopy with Transmission Electron Microscopy

Sara Nilsson
Department of Physics
Chalmers University of Technology

ABSTRACT

The cyclic methanol and hydrogen economies are two viable options in the strive for clean energy production. Industrial methanol synthesis is conducted over copper (Cu)-based catalysts. However, Cu is prone to oxidation, which leads to Cu catalyst deactivation. This highlights the need to probe catalyst performance and deactivation during relevant conditions, and why methods for operando catalyst monitoring are sought after. Moreover, individual catalyst particle-specific characteristics, such as grain boundaries, are likely to affect deactivation. Secondly, in view of the expanding hydrogen economy, efficient and reliable hydrogen sensors are required. To this end, the slowing response rate of palladium (Pd)-based hydrogen sensors over extended hydrogen sorption cycling is problematic.

To enable studies of single particle-specific performance deterioration routes, I have in this thesis developed a correlative plasmonic nanospectroscopy and transmission electron microscopy approach for *in situ* studies of interactions between individual nanoparticles and molecules in the gas phase. As my main focus, I have applied the method to shed light on Cu nanoparticle oxidation, both in pure O_2 and under CO oxidation reaction conditions. As a main result, I identified a distinct dependence of Cu oxidation on single particle-specific structural characteristics, such as grain boundaries. Furthermore, with *in situ* TEM imaging temperature-dependent competing oxidation mechanisms were observed and their corresponding single particle plasmonic signatures were mapped by electron energy-loss spectroscopy.

As a second example, in hydrogen sorption cycling of polycrystalline Pd nanoparticles grain-growth was observed that slowed down sorption kinetics, whereby an explanation for the deterioration of Pd-based hydrogen sensors was identified.

Keywords: oxidation, heterogeneous catalysis, palladium hydride, single nanoparticle, plasmonic nanospectroscopy, localized surface plasmon resonance sensing, dark-field scattering spectroscopy, transmission electron microscopy, grain boundary

LIST OF APPENDED PAPERS

The thesis is based on the work presented in the following papers:

I. **Resolving Single Cu Nanoparticle Oxidation and Kirkendall Void Formation with in Situ Plasmonic Nanospectroscopy and Electrodynamic Simulations**
S. Nilsson, D. Albinsson, T. J. Antosiewicz, J. Fritzsche and C. Langhammer
Nanoscale, 2019, 11, 20725–20733.

II. **Unravelling Competing Oxidation Mechanisms in Single Cu Nanoparticles**
S. Nilsson*, M. R. Nielsen J. Fritzsche, C. Langhammer and S. Kadkhodazadeh*, (*equal contribution)
In manuscript

III. **Exploring the Role of High-Angle Grain Boundaries in the Oxidation of Single Copper Nanoparticles**
S. Nilsson, A. Posada-Borbón, A. Bastos da Silva Fanta, D. Albinsson, J. Fritzsche, H. Grönbeck and C. Langhammer
Submitted manuscript

IV. **Copper Catalysis at Operando Conditions – Bridging the Gap Between Single Nanoparticle Probing and Catalyst-Bed-Averaging**
D. Albinsson, A. Boje, S. Nilsson, C. Tiburski, A. Hellman, H. Ström and C. Langhammer, *Nat. Commun.*, 2020, 11, 4832.

V. **The Role of Grain Boundary Sites for the Oxidation of Single Copper Nanoparticles during the CO Oxidation Reaction**
S. Nilsson, D. Albinsson, J. Fritzsche and C. Langhammer
In manuscript

VI. **Grain-Growth Mediated Hydrogen Sorption Kinetics and Compensation Effect in Single Pd Nanoparticles**
S. Alekseeva, M. Strach, S. Nilsson, J. Fritzsche, V. P. Zhdanov and C. Langhammer,
Under review in Nat. Commun. since 5th of February, 2021

MY CONTRIBUTION TO THE APPENDED PAPERS

Paper I

I performed the correlative in situ single particle plasmonic nanospectroscopy measurements and transmission electron microscopy (TEM) imaging, the finite-difference time-domain (FDTD) simulations apart from building the model, the data analysis and the figure preparation, and I wrote the first draft of the paper.

Paper II

I did the nanofabrication of the samples made by hole-mask colloidal lithography on ETEM nanochips, built the FDTD model and performed the simulations, carried out the segmentation analysis, prepared the figures and wrote parts of the paper.

Paper III

I did the in situ single particle plasmonic nanoimaging measurements, all TEM and scanning TEM (STEM) imaging, the FDTD simulations, the data analysis, the figure preparation, and I wrote the first draft of the paper.

Paper IV

I did the TEM imaging and carried out the catalysis experiments on the control samples for the X-ray photoelectron spectroscopy (XPS) analysis. I contributed to the writing of the manuscript.

Paper V

I did the in situ single particle plasmonic nanoimaging experiments, all TEM and STEM imaging, the FDTD simulations, the data analysis, the figure preparation and wrote parts of the first draft of the paper.

Paper VI

I did the TEM imaging and contributed to the writing of the manuscript.

RELATED PUBLICATIONS NOT INCLUDED IN THE THESIS

I. **Shedding Light on CO Oxidation Surface Chemistry on Single Pt Catalyst Nanoparticles Inside a Nanofluidic Model Pore**
D. Albinsson, S. Bartling, S. Nilsson, H. Ström, J. Fritzsche and C. Langhammer, *ACS Catalysis, 2021, 11, 4, 2021-2033.*

II. **A Library of Late Transition Metal Alloy Dielectric Functions for Nanophotonic Applications**
J. M. Rahm, C. Tiburski, T. P. Rossi, F. A. A. Nugroho, S. Nilsson, C. Langhammer and P. Erhart, *Adv. Funct. Mater.*, 2020, 2002122.

III. **Operando Detection of Single Nanoparticle Activity Dynamics Inside a Model Pore Catalyst Material**
D. Albinsson, S. Bartling, S. Nilsson, H. Ström, J. Fritzsche and C. Langhammer, *Sci. Adv.*, 2020, 6, 7678–7697.

IV. **A Nanofabricated Plasmonic Core-Shell-Nanoparticle Library**
A. Susarrey-Arce, K. M. Czajkowski, I. Darmadi, S. Nilsson, I. Tanyeli, S. Alekseeva, T. J. Antosiewicz and C. Langhammer, *Nanoscale*, 2019, 11, 21207–21217.

V. **In Situ Plasmonic Nanospectroscopy of the CO Oxidation Reaction over Single Pt Nanoparticles**
S. Liu, A. Susarrey-Arce, S. Nilsson, D. Albinsson, L. Hellberg, S. Alekseeva and C. Langhammer, *ACS Nano*, 2019, 13, 6090–6100.

VI. **A Nanofluidic Device for Parallel Single Nanoparticle Catalysis in Solution**
S. Levin, J. Fritzsche, S. Nilsson, A. Runemark, B. Dhokale, H. Ström, H. Sundén, C. Langhammer and F. Westerlund, *Nat. Commun.*, 2019, 10, 1–8.

VII. **Heterodimers for in Situ Plasmonic Spectroscopy: Cu Nanoparticle Oxidation Kinetics, Kirkendall Effect, and Compensation in the Arrhenius Parameters**
D. Albinsson, S. Nilsson, T. J. Antosiewicz, V. P. Zhdanov and C. Langhammer, *J. Phys. Chem. C*, 2019, 123, 6284–6293.

VIII. **A Fiber-Optic Nanoplasmonic Hydrogen Sensor via Pattern-Transfer of Nanofabricated PdAu Alloy Nanostructures**
F. A. A. Nugroho, R. Eklund, S. Nilsson and C. Langhammer, *Nanoscale*, 2018, 10, 20533–20539.

TABLE OF CONTENTS

1 INTRODUCTION

Today, there is a consensus among most scientists that global warming is an anthropological effect caused by emission of greenhouse gases. The dominant greenhouse gas is carbon dioxide (CO_2), which absorbs and re-emits infrared radiation and thereby heats the atmosphere, as was first proposed by Swedish scientist Svante Arrhenius more than a century ago.[1,2] However, the idea of global warming due to human greenhouse gas emissions was still controversial when the Intergovernmental Panel on Climate Change (IPCC) was founded in 1988.[1] In fact, it was not until the IPCC report from 2014 that it was stated that the global warming we experience is extremely likely to be due to anthropogenic greenhouse gas emissions. Since then, there is keen debate about if and when we will reach a tipping point,[3] beyond which we will experience irreversible changes. Some scientists even suggest that we are already past such a tipping point.[4]

In view of the fact that the atmospheric CO_2 concentration has increased with about 30 % since the yearly CO_2 monitoring started on the Hawaiian islands in 1958,[5] it is clear that we need to decrease greenhouse gas emissions, in order to minimize the damage to vital ecosystems and to have a chance to reach the goal of maximum 2 °C global warming agreed by world leaders in the Paris Agreement[6] in 2015. In this quest, new technologies are necessary to replace fossil fuel combustion technologies. Electricity and heat generation together with transportation accounted for about two thirds of the yearly global CO_2 emissions in 2018,[7] indicating that this is where actions to decrease CO_2 emissions are needed the most. In this transition to sustainable energy economies, I would like to highlight two examples; the cyclic hydrogen and the methanol economies.

Hydrogen-powered fuel cells provide a clean energy source, considering that the emission product when converting hydrogen to electricity is pure water. Green hydrogen production routes, such as photovoltaic electrolysis,[8] are being intensely

researched and if realised, fuel cells can be considered completely emission free. Therefore, fuel cells for transportation applications have in recent years gained more attention,[9,10] and steps are taken to expand the necessary hydrogen infrastructure in Sweden and world-wide. In striving towards a hydrogen economy, the safety aspect of storing and transporting hydrogen also requires fast and accurate hydrogen sensors.[11] For this purpose, palladium (Pd) is one of the main contestant materials, due to its efficiency in breaking the hydrogen bond and form a hydride at room termperature.[12]

As the second example, I would like to discuss the concept of a closed carbon cycle, where the general idea is to achieve a net zero emission of CO_2 and CH_4 (mutually referred to as carbon emissions). Technically, this is to be realized by capturing CO_2 from powerplants or by direct-air-capture, and subsequently, from the captured CO_2 can methanol fuel be produced, known under the umbrella of carbon capture and utilization (CCU) techniques.[8] CCU technologies are proposed to be an alternative route for decreasing carbon emissions in the near future as part of the transition towards zero carbon emissions. In this context, copper (Cu) catalysts are widely used in the methanol synthesis reaction and efforts to understand the dynamic changes of the oxidation state of Cu during the reaction are ongoing.[13,14] Apart from a green hydrogen production, efficient catalysts for hydrogenation of CO_2 to methanol with high selectivity are required for the methanol fuel economy to become a viable alternative to fossil fuels.[8] To achieve high efficiency and selectivity in heterogeneous catalytic reactions, detailed understanding of the active phase along with catalyst deactivation is essential, as well as applying this knowledge to monitor the catalyst health on-line in the reactor.[15]

1.1 IN SITU CHARACTERIZATION TECHNIQUES

Even though heterogeneous catalysis has been applied industrially for over 100 years many fundamental knowledge gaps still exist, such as elucidating which the active phase during the reaction is, unravelling which the active sites are and mapping the relevance of the catalyst-support interactions, to name a few. During the second half of the last century, catalyst research saw major advance thanks to ultra-high vacuum (UHV) based surface science techniques. However, during the past two decades the importance of studying surface reactions at so-called operando conditions,[16] that is conditions close to or equivalent to, e.g. an industrial reactor, has been acknowledged. The focus on operando studies is fuelled by the understanding that reaction pathways may be significantly altered when the reactant pressures are increased. This is commonly referred to as the *pressure gap*.[17,18]

Currently, the pressure gap is shrinking thanks to recent developments of surface analysis techniques that incorporate ambient pressure gas control in the reaction chamber, such as in high-pressure scanning tunnelling microscopy (HP-STM)[18], various in situ X-ray diffraction and absorption techniques[19,20], as well as ambient pressure X-ray photoelectron spectroscopy[20] (AP-XPS). They all enable in situ characterization of functional surfaces or catalysts at atmospheric pressures. Here, by the term *in situ*, I am referring to studies probing the catalyst condition while the catalyst is working, i.e. under (close to) relevant operational conditions.[20,21] Moreover, to study the performance and deactivation of the catalyst, it is relevant to probe the catalyst in situ and simultaneously detect the reaction products, hence, this is referred to as *operando* studies.[22]

Additionally, in traditional UHV studies, as well as HP-STM and AP-XPS, mostly single crystal surfaces are probed, while industrially relevant catalysts are typically nanoparticles with sizes of a few nanometers. Hence, there is a significant *materials gap* in terms of size, shape and complexity in the structure of the catalyst materials.[23] Ultimately, in situ and operando techniques with single nanoparticle resolution are required in order to identify the performance of catalyst particles in terms of activity, selectivity and deactivation resistance.[24]

One technique for performing in situ studies is the in situ transmission electron microscope (TEM), which enables investigations of reactions on single catalyst particles of industrially relevant sizes under (close to) ambient conditions.[25] In recent in situ TEM studies, insights on catalyst structure dynamics under reaction conditions have been uncovered, which provide structure – function relations down to the single site level.[26] However, the limitation of studies under reaction conditions in TEM is the uncertainty in the effect of the electron beam on the reaction kinetics.[27] Furthermore, there is a danger in the scrutiny of only a handful of nanoparticles as is usually done in such studies. First, because such few catalyst particles cannot give a statistical representation of the real catalyst that is comprised of billions of nanoparticles, and second, due to the prevalent structural heterogeneity among the particles.[19]

On the other hand, when probing a large-scale working catalyst, potentially only the fraction that are the most active nanoparticles, or even only a couple of sites on those particles, may be contributing to the measured signal, while the rest are "silent".[28] Additionally, when probing a large ensemble of inherently different particles, the effect of particle individuality, such as size, shape, grain morphology, crystal facets and edges, are lost due to averaging over the ensemble. Hence, in the effort to bridge the materials gap, techniques which can connect the structure – function insights from

individual nanoparticle studies, such as in situ TEM, to that of the "real" catalyst particle ensemble, are highly sought after.

However, to this date there are only a couple of techniques that can fulfil both the single particle resolution requirement, as well as the operation at high pressure and elevated temperature conditions. Nevertheless, there are a range of optical microscopy techniques that fulfil these requirements since optical methods by their nature are highly suitable for operando investigations. Photon-based probes do not require UHV, and, moreover, optical photons in the visible range have relatively low energy and are therefore less invasive to the molecules participating in the reactions and the nanoparticles compared to, e.g. high-energy electrons used in TEM.[24] In this context, I would first like to mention super-resolution fluorescence microscopy (SRFM), for which the inventors were rewarded the 2014 Nobel prize in Chemistry. By SRFM, single fluorophores can be spatially resolved on a sub-particle level to map active sites. However, such investigations are depending on the light emission from fluorophores and can thus only be applied to a limited number of liquid phase reactions.[24,29] Further examples of optical techniques with individual nanoparticle resolution are Raman spectroscopies[15,30] and dark-field scattering spectroscopy (DFSS)[24].

The DFSS technique is the basis of the in situ plasmonic nanospectroscopy[31,32] approach that I have applied in this thesis to shed light on structure – function relations. Similarly to other optical microscopy techniques, plasmonic nanospectroscopy provides means for particle multiplexing in order to acquire larger single particle data sets with statistical relevance. In this way, optical microscopy can connect single particle level understanding with the industrially relevant ensemble level.[24] On the downside, however, optical techniques are in most cases lacking the ability to provide structural information about the imaged particles, and are therefore often combined with scanning or transmission electron microscopy that provide (sub-) nanometer spatial resolution. This combination of techniques is the central theme of my thesis, where I have combined the particle-specific in situ signals from plasmonic nanospectroscopy with the individual particle structure information obtained ex situ from TEM. In order to correlate these two separately obtained pieces of information, I have simulated the optical response of the particles by finite-difference time-domain (FDTD) electrodynamic simulations. FDTD has thus provided a means to identify and quantify the physical origin of the experimentally measured plasmonic response, and thereby enable the translation of the structural information acquired from TEM to the in situ plasmonic nanospectroscopy readout. The combination of these three components; in situ plasmonic nanospectroscopy, TEM imaging and FDTD simulations, has proven paramount to, with combined strengths, shed light on the

significance of particle-specific traits in the metal nanoparticle – gas molecular interactions studied in this thesis.

After this short introduction to the state-of-the-art of in situ and operando experimental techniques that are of relevance for my thesis, I would like to take a step back and highlight that we today actually can fabricate and manipulate materials on the nanoscale – with objects one thousand times smaller than a single strand of hair. In addition, we have tools to probe and to visualize events and reactions on these nanoscale materials in real time. To me, from the start this was one of the most attractive aspects that motivated me to take on the challenge of this thesis project. I still find it a truly astonishing scientific achievement, and personally, I feel grateful to have had the chance to explore the possibilities presented by these methods.

1.2 THE SCOPE OF THIS THESIS

My ambition with this thesis is to address both structural and chemical phase transitions of individual metal nanoparticles using plasmonic nanospectroscopy in combination with transmission electron microcopy as the main tools. By employing these methodologies, I have been able to unravel structure – function relations of individual metal nanoparticles. These relations are exemplified largely in my studies of the oxidation mechanisms of single Cu nanoparticles in pure oxygen and during the catalytic CO oxidation reaction, as well as the hydride formation kinetics in polycrystalline single Pd particles.

In **Paper I,** I explored the correlative plasmonic nanospectroscopy and TEM approach to monitor the oxidation of individual single crystalline Cu nanoparticles. Specifically, I demonstrated that the formation of a nanoscale void can be probed in situ in individual Cu nanoparticles by their intrinsic localized surface plasmon resonance response. The formation of the Kirkendall void was signaled in the optical readout as a split into two resonance modes, due to the induced asymmetry of the remaining Cu core, which I unravelled by comparing the experimental single particle data with corresponding FDTD electrodynamic simulations.

In a collaborative effort together with Shima Kadkhodazadeh at the Technical University of Denmark (DTU), I further investigated the oxidation mechanisms of individual Cu nanoparticles in **Paper II**. Specifically, we were able to map the competing oxidation mechanisms in differently sized Cu nanoparticles oxidized at temperatures between 50 - 200 °C by imaging and using electron energy-loss spectroscopy (EELS) in an environmental TEM. The study revealed the occurrence of four parallel mechanisms, i.e., the oxide nucleation and growth, the Cabrera-Mott

mechanism at 50 °C, and the Valensi-Carter mechanism together with the nanoscale Kirkendall void growth at higher temperatures.

In **Paper I and II**, I observed indications that high-angle grain boundaries may influence the oxidation mechanism – a hypothesis I further explored in **Paper III**. By resorting to density functional theory calculations in the collaboration with Alvaro Posada-Borón, we could identify the Cu atom extraction from the metal lattice as the rate limiting step during oxidation at 150 °C. This provided an explanation for why enhanced diffusion in polycrystalline nanoparticles does not lead to a faster oxide growth rate during the initial phase of oxidation. The influence of the grain boundaries was instead manifested as an attenuation of the plasmon resonance proportional to the grain boundary density likely caused by Cu vacancy accumulation at the grain boundaries.

As a slightly different application, in **Paper IV** together with David Albinsson, we used the single particle plasmonic nanospectroscopy readout to monitor the oxidation state of individual model Cu catalyst nanoparticles during the catalytic carbon monoxide (CO) oxidation reaction inside a nanofluidic reactor, revealing that the decrease in CO oxidation activity is accompanied by Cu particle oxidation. Furthermore, we observed striking differences in the individual Cu nanoparticle responses during reaction, speculatively attributed to different particle morphology. Therefore, in **Paper V**, I further explored the implications of single Cu nanoparticle grain morphology during the oxidation of a Cu model catalyst under CO oxidation reaction conditions and identified preferential nucleation of the oxide at grain boundary – particle surface intersections.

Finally, in **Paper VI** together with Svetlana Alekseeva, significant grain growth in single polycrystalline Pd nanoparticles was observed, resulting in a significant decrease of the rate of hydrogen absorption and desorption. To unravel the impact of grain growth on hydrogen sorption rates, the simultaneous measurement of a large number of individual nanoparticles enabled by plasmonic nanoimaging was crucial. The collection of a large particle data set enabled a rigorous assignment of grain growth as the physical origin of the observed kinetic compensation effect – an effect which usually is attributed to statistical error. This variant of the plasmonic single particle approach was also used in **Paper III-V**, where it proved critical for the production of statistically significant single particle data sets. The large data sets are necessary for the rigorous investigation of intimate details in structure-function relationships of the interaction between molecules and metal nanoparticles, and to connect the observations with the ensemble response relevant for the technical applications of the investigated nanoparticles.

2 CRYSTAL GRAIN BOUNDARIES

In simplified terms, one can divide solids into either amorphous or crystalline forms. For example, many polymers are amorphous, whereas metals commonly are crystalline. Other materials, like silicon dioxide (SiO_2), can be found in either amorphous forms, commonly known to us as glass, or crystalline forms, of which quartz is an example. Amorphous materials are lacking long-range order, whereas in crystalline structures, the atoms are arranged in a lattice of a certain periodicity with long-range order.

The arrangement of the atoms in the crystal lattice is commonly classified from the smallest unique building block, the primitive cell.[33] Here, the most basic geometry one can think of for a cell in three dimensions is probably the cube. The simple cubic (sc) lattice structure, however, is not very common in nature because it is not close-packed, that is, the atoms have few neighboring atoms. To achieve a higher close-packing, one can add atoms either in the center of the cube, yielding what is known as the body-centered cubic (bcc) lattice, or on the faces of the cube to form the face-centered cubic (fcc) lattice. These three lattice structures are illustrated in **Fig. 2.1**, however, these are not the primitive cells, because it includes several atoms which if translating the cube are identical.

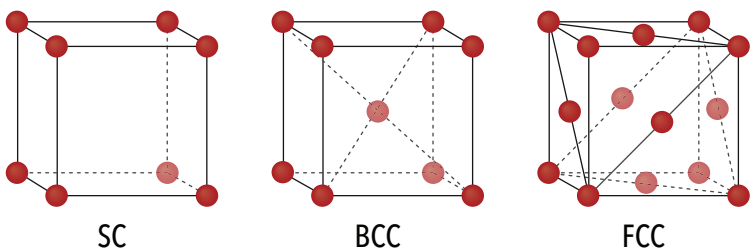

Figure 2.1: The cubic crystal structures: *simple cubic (sc), body-centered cubic (bcc) and face-centered cubic (fcc).*

The fcc crystal structure, together with the hexagonal close-packed structure (hcp), are as well-packed as one can achieve with spherical objects (atoms) in three dimensions and fill 74 % of the total volume.[34] For example, Cu, silver (Ag), gold (Au) and Pd all have fcc structure, whereas ruthenium (Ru) is an example of a hcp crystal, and iron (Fe) is an example of a bcc crystal.[35] There exist also more complex crystal structures, which commonly form when two or more atoms of different types are combined.

The lattice of a crystal is built up by the primitive cell, where the translation from one primitive cell to the next can be described by a set of vectors, $\boldsymbol{a_1}$, $\boldsymbol{a_2}$ and $\boldsymbol{a_3}$. A common way of describing the various planes in the crystal found by different combinations of the vectors is to use Miller indices (**Fig. 2.2**). To find the Miller index (hkl) of a lattice plane one should first find the intercept of the plane with the translation vectors [e.g. (1,∞,∞)], take the reciprocal of these numbers [i.e. (1,0,0)] and reduce by a common factor to the smallest possible integer.[34]

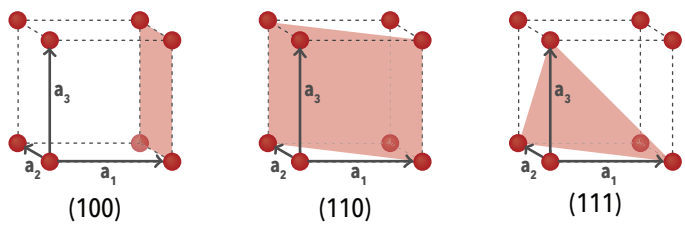

Figure 2.2: The three simplest cubic lattice planes: (100), (110) and (111). *Examples of three lattice planes (pink surfaces) in a simple cubic unit cell and their Miller Indices: (100), (110) and (111), respectively.*

Similar to interference patterns obtained from optical photons diffracted by a grating, diffraction of electrons or X-ray photons can occur on the lattice planes of a crystal. This interaction is possible because the wavelengths of high energy electrons and X-rays are comparable to the size of the atoms (~ Å). This phenomenon is explored in order to characterize crystalline materials by means of methods employing X-ray diffraction or electron diffraction. I will introduce some common methods of electron diffraction for characterizing the crystal orientation in Chapter 7.

2.1 CRYSTAL GRAINS

So far, we have discussed that in solids, and in particular metals, the atoms are often arranged in crystalline lattices, and we have assumed ideal single crystals. However, "real" crystals commonly contain defects. With increasing size, it is likely that the material is comprised of several smaller crystallites. Such a material is known as a

polycrystal and the crystallites are referred to as *crystal grains*. The interface between two crystal grains, the *grain boundary*, is of interest because even though it only constitutes a small part of the total volume, it can significantly influence physical properties, such as the electronic conductivity[36], the specific heat capacity[37], the strength[37], the ductility[37,38], as well as the self- and impurity-diffusivities[37].

When combining two crystals, it is easy to imagine that there is an infinite number of possible combinations by either translating, tilting or twisting the crystals, and thereby exposing different lattice planes at the boundary. In fact, there are five macroscopic degrees of freedom to describe a grain boundary, whereof three are related to the translational misorientation between the crystal lattices and two are related to the inclination of the boundary plane.[39] Furthermore, there exist microscopic degrees of freedom, such as atomic relaxation.[40]

Because of the complexity in grain boundaries, in a summarizing review of the history of crystallographic research, David Brandon starts out by claiming ”Any attempt to summarize the concept of ‘grain boundaries’ in a short article is destined to fail”.[41] Therefore, I will here not attempt anything close to that, but merely state that there are several ways of characterizing grain boundaries, either from their excess volume[42], energy[40] or the coincident site lattice (CSL).[43] The CSL model provides a common way of categorizing grain boundaries in cubic lattices by the Σ value. When combining two crystal lattices, one can find overlapping lattice sites, as illustrated in **Fig. 2.3** for two lattices which share every third lattice site. The Σ value is the reciprocal of the number of coinciding sites between the lattices, hence, the grain boundary in **Fig. 2.3** is a coherent twin boundary with $\Sigma = 3$. The CSL is a purely geometrical model that tells how much the lattices overlap. Furthermore, a high Σ value does not necessarily mean that it is a high-energy grain boundary, which is somewhat misleading and is one of the criticisms of the model.[43,44]

In general terms, one can say that the energy associated with a grain boundary is increasing with the tilt or twist angle of the boundary plane between the crystal lattices, with some local energy minima exceptions, such as the coherent twin boundary.[39,40] However, any grain boundary model is bound to be a simplification of the real boundary, since most real boundaries are not as simple as a symmetrical tilt with respect to the plane boundary, but are rather asymmetrical and curved. To this end, molecular dynamics simulations have proven useful in revealing how the grain boundary affects material properties, such as diffusion, impurity segregation, strength and grain growth.[45]

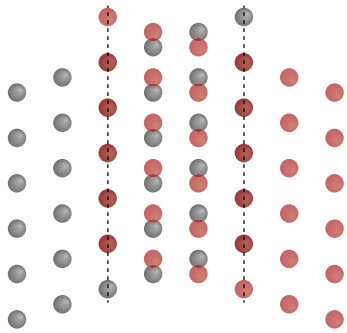

Figure 2.3: The coincident site lattice. *Two overlapping crystal lattices (red and gray), if counting only the red atoms, we can see that every third red atom overlaps with a gray atom (marked by dashed lines), hence, this grain boundary has Σ = 3 and is a model of a coherent twin boundary.*

Historically, micrometer-sized grains have been the focus of most studies in order to reveal relations between functions and grain size. One example is the Hall-Petch relation, which states that the mechanical strength increases as the grain size decreases.[38] However, when reducing the size of objects to the nanometer scale, also the grain size is reduced, and one approaches the regime of *nanocrystalline* materials. At this "new" length scale, the relations of micrometer-sized grains are not always valid. As is evident from the example of the mechanical strength; below a certain critical grain size specific to each material, e.g. 19 and 11 nm for Cu and Pd,[38] respectively, the relation is reversed and the strength starts to decrease, as the grain size is further reduced.

2.2 RECRYSTALLIZATION AND GRAIN GROWTH

The common method of shaping metal pieces through cold working introduces a high density of defects, such as dislocations, vacancies and interstitials, as well as new interfaces in the form of deformation twinning. Hence, with increased defect density, the energy stored in the material is increased. The strength is increased but ductility is reduced, therefore, to enhance the ductility and softness of the metal, it is usually thermally treated, i.e. heated to a temperature where the atoms become slightly mobile.[46] This method of cold working bulk metal might seem far away from the topic of my thesis, but the grain morphological dynamics observed during the thermal treatment have implications also for nanocrystalline materials, even if there exist some differences, which I will discuss after introducing the general concepts.

In the highly distorted polycrystals obtained from cold working, diffusion and annihilation of point defects (drawn as red dots in **Fig. 2.4a**) and dislocations start

already at relatively low temperatures in order to release local strain. These processes are collectively known under the term *recovery*.[46] The recovery of dislocations results in formation of low-angle boundary sub-grains (drawn as a honeycomb pattern in **Fig. 2.4b**), without altering the overall grain size.

At temperatures of 30 - 50 % of the melting temperature, the recrystallization process is actuated. Specifically, this means that sub-grains in recovered areas start to grow by forming mobile high-angle grain boundaries. The driving force for recrystallization is to minimize the energy stored in the material, which means that crystallites with distorted grain boundaries, high density of dislocations and high strain gradients will start the recrystallization process.[46] The recrystallization is nucleated at the some sub-grain and continues through grain boundary motion.[46] During the nucleation phase, recrystallization is slow, after which it proceeds at a higher rate, therefore the complete grain structure transition follows a sigmoidal function with time. This tells us that after some critical time, increasing the annealing time further will not significantly change the grain morphology, hence, increasing the annealing temperature is more important for the final structure.[47,48]

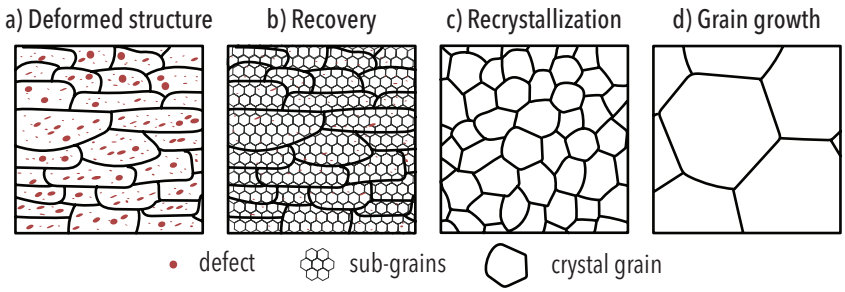

Figure 2.4: *The steps of morphological transitions of deformed polycrystals subject to thermal treatment include; a) a structure with deformed grains formed by cold working (red dots are illustrating defects), b) recovery through decreasing defect density and sub-grain nucleation (drawn as a honeycomb lattice), c) recrystallization of the grain morphology and d) competitive grain growth. Figure is adapted from reference* [46].

At some point, only reshaped low-strain grains separated by mainly high-angle boundaries remain and at this point the process of competitive grain growth is dominating. This means that the largest grains are growing further at the expense of the smaller grains to minimize the overall high-angle grain boundary length. This grain growth is sometimes not desired in engineering applications since it decreases the strength of the material.[38,46] However, the electric conductivity is lower along high-angle grain boundaries compared to twin boundaries and across the bulk lattice, which

is an incentive to endorse grain growth.[36] Yet another property of the grain boundaries, which we observed explicitly in **Paper VI**, is the enhanced diffusion of sorbates along the grain boundaries, such as hydrogen in highly polycrystalline Pd. Unfortunately, the Pd polycrystallinity is reduced due to the grain growth induced in the Pd by hydrogen sorption cycling, which reduces the hydrogen diffusivity.

The grain size in the as-deposited Pd nanoparticles in **Paper VI** is only a few nanometers and can thus be categorized as truly nanocrystalline. Grain growth in nanocrystalline Pd has been observed even at room temperature and has been demonstrated to follow a non-linear growth rate,[49] diverging from the parabolic growth rate of what is referred to as *normal* grain growth commonly observed in coarse-grained systems.[50] The *abnormal* grain growth, often observed in nanocrystalline systems,[47] means that the grain sizes do not follow a normal distribution but are instead divided into two distinct size distributions.[50]

Moreover, grain growth in nanocrystalline Cu thin films studied by in situ TEM, has been observed to have a lower apparent activation energy, E_a ~ 0.35 eV, compared to coarse-grained films (micrometer-sized grains), E_a ~ 1 eV.[47] This implies that the recrystallization of nanocrystalline films starts at a lower temperature compared to coarse-grained films. Two reasons have been suggested to explain this discrepancy; i) a higher defect density in nanocrystalline films and ii) a higher probability of grain boundary movement since the grain boundary is shorter and therefore requires fewer atoms to jump over the boundary in order for it to move. Furthermore, it has been observed that the density of annealing twins formed in a nanocrystalline film increased with time and annealing temperature.[47] By molecular dynamics simulations, both the lower activation energy of grain growth in nanocrystalline Cu films and the formation of annealing twins have been suggested which agrees with the experimental results,[51] proving the strength of combining experiments and simulations to understand the properties of grain boundaries.

3 METAL OXIDE AND HYDRIDE FORMATION

We recognize metal and gas interactions in our daily life, for example, in the form of metal corrosion, as seen on rusty cars and green copper roofs. These two are perhaps the most well-known types of metal corrosion. Chemically, rust is an iron (Fe) oxide compound, which is comprised of several iron oxide forms, out of which hematite (Fe_2O_3) and magnetite (Fe_3O_4) are two well-known examples.[52] The oxidation of iron can proceed until the metal is completely consumed and disintegrated.

Cu, however, as most metals, does not disintegrate upon oxidizing, but rather forms a self-limiting oxide film on the surface, which is protecting the bulk from further oxidation. The dark orange color commonly seen on copper pipes is often mistaken to be the color of copper but is, in fact, the color of copper oxide. Surprisingly, the true color of copper is brightly pink, but it is rarely seen because in air, copper surfaces are rapidly covered with a thin layer of the oxide, Cu_2O.[53] Copper is also often associated with the green patina of copper roofs, for example. Here, the color comes from copper salts, which form in reaction between Cu and various species present in the atmosphere, such as sulphur, chloride and different carbonaceous molecules.[53,54]

In macroscopic applications of Cu, its corrosion might not be too problematic. However, on the nanoscale the situation is different, since the excellent electronic conductivity of Cu[55] deteriorates dramatically when Cu micro- and nanostructures used in microelectronic circuits oxidize and thus transform into semiconducting oxides. Similarly in catalytic applications, where metallic Cu is an efficient catalyst for CO oxidation to CO_2 (as I will discuss in Chapter 4),[56] the formation of oxide phases can be problematic since it reduces catalyst activity. Hence, it is important to develop methods that enable the mapping of oxidation conditions for Cu nanostructures, and to understand the underlying mechanisms.

In this chapter, I will discuss the interaction of molecules with metal surfaces in detail by both touching upon the key aspects of adsorption, and by specifically discussing the details of the oxidation process for the case of Cu, with particular focus on nanostructures. Furthermore, I will briefly discuss the interaction of hydrogen gas with Pd nanostructures, which is of great relevance for applications in hydrogen sensor technologies,[57] where the miniaturization of the active material to the nanoscale has proven critical for decreasing sensor response times.[58]

3.1 SURFACE ADSORPTION

In most processes involving interactions between metal surfaces and molecules in the gas phase, surface adsorption is the natural first elementary step, since the surface is the interface between the solid and the gas. When the gas molecule approaches the surface, the first interaction is by van der Waals attraction, which leads to *physisorption* of the gas molecule without any chemical bonds (first potential well in **Fig. 3.1**). When the gas molecule is physisorbed, it is staying at a constant distance of a few Ångström from the surface, equal to the van der Waals radii of the surface atom plus the gas atom.[59] Physisorption is a result of the attractive van der Waals interaction and the repulsive potential due to the Pauli principle when the molecular electrons interact with the electrons of the surface atoms.[35] Furthermore, the interaction between the electrons of the molecule and the surface can also lead to *associative chemisorption* (second potential well in **Fig. 3.1**), i.e. a covalent bond is formed with the surface atom, without breaking the molecular bond.[35]

A molecule in the gas phase is unlikely to overcome the dissociation barrier, which, as an example, for the oxygen molecule (O_2) is about 500 kJ/mol[60]. However, when adsorbed on the surface of a transition metal, the energy barrier for dissociation is usually lower than the barrier for desorption from the surface. Hence, it is likely that the molecular bond is broken and that each atom becomes covalently bound to a surface atom - this is known as *dissociative chemisorption* (third potential well in **Fig. 3.1**). A dissociatively adsorbed species can, in some cases, diffuse into the metal lattice, where each diffusion jump is associated with an activation energy.[59] This so-called lattice diffusion is discussed below in Section 3.2.

Concerning adsorption of the two most relevant gases for my thesis, the adsorption and bond breaking of H_2 on Pd is facile at room temperature and hydrogen atoms easily diffuse into the Pd lattice to occupy interstitial lattice sites.[59] In the second relevant case, the adsorption of O_2 molecules on Cu surfaces is fast. As an example, the barrier for dissociative chemisorption of O_2 on Cu(100) is less than 0.1 eV.[61]

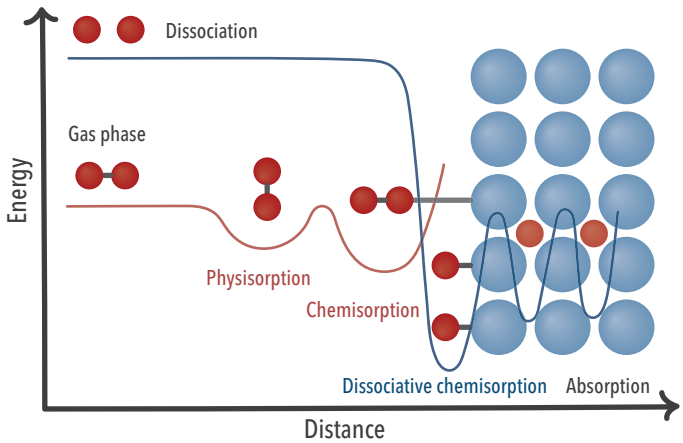

Figure 3.1: Surface adsorption. *The energy landscape of molecular surface adsorption is dictated by the van der Waals attraction and Pauli repulsion (red line), and the dissociation barrier (blue line). Surface adsorption occurs either through molecular physisorption without breaking molecular bonds or through associative or dissociative chemisorption, which entails the formation of covalent bonds with surface atoms. Dissociated species may also diffuse into the lattice, where a diffusion jump is associated with a specific energy barrier. Figure adopted from reference* [59].

In reality, at ambient temperature and pressure, metal surfaces are always covered by adsorbates. Thus, for a gas molecule to be adsorbed on the surface it has to take the place of another already adsorbed species. However, some species which form strong bonds to the surface, such as CO on Pd, are not easily removed by other gas molecules impinging on the surface. Therefore, the "blocking" of surface atoms by strongly-bonded species is referred to as surface poisoning. This effect is of particular relevance in catalysis, where the poisoning effect deactivates catalyst surfaces at certain reaction conditions.[11,62,63]

3.2 DIFFUSION IN SOLIDS

If the gas – metal interaction is not limited to the topmost atomic surface layer, atoms can enter and diffuse through the solid either interstitially or by a vacancy jumping mechanism. Apart from absorbate or impurity diffusion, there is also self-diffusion of atoms within their own lattice, such as diffusion of Cu atoms in the Cu lattice. Concerning absorbate diffusion, I will discuss oxygen ion diffusion in the Cu and Cu oxide lattices, and interstitial diffusion of hydrogen in the Pd lattice. However, it

should be mentioned that there are also other types of diffusion, for example in alloys, or of impurities, where metal atoms diffuse in a host lattice.

Generally, diffusion can be described by Fick's law, which states that the direction of diffusion is in the opposite direction of a concentration gradient. For a one-dimensional system in equilibrium, the flux of a species can be written as

$$J = -D\frac{dC}{dx} \tag{3.1}$$

where D is the diffusion constant, C is the concentration of the species and x is the spatial coordinate.

Considering again the situation of the gas-metal interface, the adsorbed gas atoms/molecules can diffuse on the surface. As in the case of the copper – oxygen system, oxygen adatom surface diffusion is associated with small barriers, thereby locally forming small oxide islands on Cu,[64] as discussed in Section 3.3.1. Cu atom diffusion on the Cu surface, on the other hand, is slower, with an activation barrier for surface diffusion of 0.69 eV[65].

In the lattice, diffusion of atoms can follow different routes; i) jumping to a vacant lattice site, ii) interstitial diffusion, iii) direct position interchange, that is, two atoms change positions in the lattice, or iv) ring diffusion, where three or four atoms next to each other change positions by permutation.[66,67] The vacancy jumping mechanism and interstitial diffusion are probably the two most common mechanisms for lattice self- or impurity-diffusion.[68] Interstitial diffusion is common for impurity atoms that are smaller than the lattice atoms, since it results in a smaller perturbation of the lattice.[68] One example of interstitial diffusion is when hydrogen diffuses by occupying interstitial sites in Pd. In the relevant example of Cu self-diffusion, this is suggested to be dominated by vacancy diffusion at moderately high temperatures (> 200 °C),[66] and is associated with a diffusion activation energy of 2.1 eV.[69] In **Paper III**, we discuss that the diffusion of Cu atoms through the bulk is mainly by vacancy diffusion based on density functional theory (DFT) calculations. At lower temperatures (< 100 °C), it is suggested that interstitial diffusion is dominating.[66]

Generally, diffusion along grain boundaries and other defects, such as dislocation lines/planes or phase boundaries, is termed short-circuit diffusion. This refers to that it provides a faster route compared to lattice diffusion.[67] Mechanistically, diffusion along grain boundaries can either happen by the vacancy jumping mechanism or by interstitial migration, depending on the type of grain boundary.[70] Due to the direct relevance for my work, I will focus here on grain boundary diffusion, for which the

rate is highly depending on the type of grain boundary.[71,72] Again focusing on Cu, in coherent twin boundaries, the defect density is low and the diffusion activation energy is close to the one for lattice diffusion.[70] In grain boundaries with a high misorientation between the crystallites, associated with higher interfacial energies, the diffusion activation energy is comparable to that of surface diffusion.[65,70,72] Furthermore, the diffusion rates are increasing with temperature and there is a critical temperature for which the difference in the rates of grain boundary and lattice diffusion becomes negligible, and diffusion will take place mainly through the lattice.[66] Because diffusion is temperature-activated, the diffusion rate can be described by an Arrhenius-type equation;

$$D(T) = D_0 e^{-\frac{E}{k_B T}} \tag{3.2}$$

where D_0 is the diffusion rate constant, k_B is the Boltzmann constant and E the diffusion activation energy.[68] To accommodate vacant site jumping, the vacancy first needs to be created by overcoming the vacancy creation barrier E_{vac}, in addition to the jump activation energy E_{jump}. Yielding the total activation energy of $E = E_{vac} + E_{jump}$.[66] Commonly, in the metal lattice there is an inherent abundance of defects, such as vacancies, and in particular at elevated temperatures, which readily enables vacant site diffusion jumping.[66]

3.2.1 The Kirkendall effect

Until the mid of last century, the common perception was that in a binary system both elements A and B are diffusing at the *same* rate and can be described by a common interdiffusion coefficient.[67] When it was first reported that elements A and B in a binary system can diffuse with *different* rates, it was highly controversial and met by significant skepticism.[73] In the renowned, but at first questioned, report by Smigelskas and Kirkendall[74], they studied diffusion in a copper-plated brass volume by the copper – zink (Zn) diffusion couple. The interface between Cu and brass was marked by inert molybdenum (Mo) rods. The Mo markers were observed to move inward, as a consequence of the shrinking brass volume, which was attributed to the higher diffusion rate of Zn compared to Cu in brass. This is now referred to as the Kirkendall effect and the shifting plane of the inert markers is commonly called the Kirkendall plane (marked in **Fig. 3.2**).[66,67]

In the case of the ideal Kirkendall effect, the original interface is shifting due to the net mass transport in the interdiffusion zone (marked by the gray area in **Fig. 3.2**). Furthermore, there is a net vacancy flux, J_V, to accommodate for the volume change from the unequal diffusion rates, which in the ideal case is $J_V = J_B - J_A$. This was

observed for the Cu (material B) – Zn (material A) diffusion couple in brass.[67] However, often the vacancy flux is not enough to accommodate the volume change, and it leads to pore formation and/or volume shrinkage on the side of the faster diffuser (material B in **Fig. 3.2**), and to swelling on the slow diffuser side (material A). Furthermore, stress develops on each side of the interface, that is, tensile stress in the lattice where atoms are missing (element B) and compressive stress where there are more atoms than in the original lattice (element A).[67] Pore formation is for example observed in the copper – tin (Sn) diffusion couple, where Cu is the high diffuser (material B) and Sn is the slow diffuser (material A).[67]

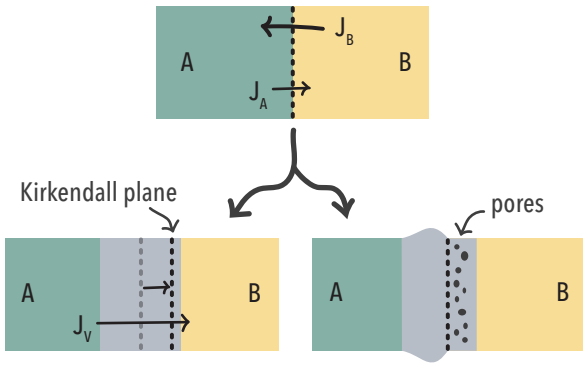

Figure 3.2: The Kirkendall effect. *A diffusion couple, A and B, where the diffusion coefficient of B is higher than A, leads to a shifting Kirkendall plane accommodated by vacancy diffusion, but not to volume expansion, in the case of ideal Kirkendall effect. If the vacancy diffusion is absent, it leads to a volume expansion on the side of the slow diffusing material (A) and to pore formation or shrinking on the side of the faster diffuser (B).*

In this Section, my intention was to give a short introduction to diffusion theory. For more in-depth reading, I recommend two books[67,68]. After this introduction of the general concepts of surface adsorption, diffusion and the Kirkendall effect, we can now take a closer look at the oxidation of surfaces in the next Section.

3.3 METAL BULK AND THIN FILM OXIDATION

From a chemical point of view, oxidation is removing electrons from an atom or a molecule. Therefore, the oxidation of metals is promoted by oxidative reagents, molecules or atoms, that accept electrons, such as oxygen, sulfur or dissociated water.[66] Removing one electron from a metal atom (M) yields a metal ion M^+ in the first oxidation state, M(I). Further removing one electron yields M(II), and so forth.

For the example of Cu, the first and second oxidation states are stable and are stoichiometrically written as Cu_2O, which is known as *cuprous oxide*, and CuO, *cupric oxide*.[54] Furthermore, there is an intermediate crystal form, Cu_4O_3, constituent of a mix of both copper oxidation states. It is less well-known and has only been observed for thin films.[75] Commonly, the outer most layer of the Cu oxide is comprised of CuO, whereas the thicker underlying oxide is Cu_2O.[76,77] As a side note, under certain intermediate copper oxidation temperatures around 450 °C, CuO needles have been demonstrated to grow from the underlying Cu_2O film.[66,78]

Let us now turn to the mechanistical understanding of the surface oxidation of metals, which was a field of intense research during the last century. These efforts have resulted in a couple of mechanistic models, out of which the most widely accepted one is the Wagner model. In this model, the oxidation rate is suggested to follow a parabolic rate law[66]

$$\frac{dL}{dt} = \frac{k}{L} \tag{3.3}$$

where L is the oxide thickness and k is the parabolic rate constant. The rate is controlled by the diffusion rate of ions through the oxide, which gives the parabolic rate.[66,79] The Wagner model is valid in the limit of thick oxide films, on the order of micrometers.[79]

In the limit of thin oxide films < 100 Å, the situation is different. Many metals, such as aluminum, readily form self-limiting thin oxide layers at room temperature and atmospheric oxygen pressure, which prevent further bulk oxidation. In the model suggested by Cabrera and Mott, the growth of this thin oxide film at ambient temperature is promoted by a static electric field, which is induced due to electrons that are traversing the oxide, either by tunneling or thermionic excitation to the oxide conduction band.[80] At the oxide-gas interface, the adsorbed O_2 is dissociated and in ionic form, thereby creating an electrostatic potential between the negatively charged oxide-gas interface and the positively charged metal-oxide interface, the so-called Mott field.

The field strength is inversely proportional to the oxide thickness L. Hence, the oxide growth rate will decrease exponentially with increased oxide thickness and is, therefore, following an inverse logarithmic rate law described by

$$log\left(\frac{dL}{dt}\right) = B_1 + \frac{B_2}{L} \tag{3.4}$$

where B_1 and B_2 are rate constants.[79] As a consequence, the oxide growth stops at some critical thickness for which the field strength is too weak to drive the metal ion diffusion.

An important conclusion from the above discussion is that one single model cannot describe the oxidation process in both the thin and thick film regimes. Therefore, it is useful to employ different rate laws, depending on the oxide thickness at hand. At the same time, the different mechanisms make the modelling of the oxidation process in the intermediate oxide thickness regime difficult. Accordingly, this regime is still poorly understood. For Cu alone, there are experimental reports which suggest the oxidation in the intermediate regime to follow either linear, cubic, parabolic, direct or indirect logarithmic rate laws.[81] At least in part, the divergence in the oxide growth rates can be attributed to slight differences in experimental conditions, impurity concentrations, surface facets and crystal grain morphology in the different studies. A unified theoretical model has nevertheless been suggested.[79] The model connects the Cabrera-Mott and Wagner mechanisms by modelling the field in the oxide between these two regimes by including the Debye-Hückel screening length. This results in a combination of a parabolic and direct logarithmic rate law in the intermediate thickness regime.

3.3.1 Oxide nucleation on copper surfaces

I start this section by looking into the nucleation of the oxide phase on Cu surfaces. Both kinetic Monte Carlo (KMC) simulations and experimental in situ TEM and scanning electron microscopy (SEM) studies show evidence for the nucleation of oxide islands on Cu(100) and Cu(110) facets.[61] The oxide islands form either as nanorod or pyramid shapes, as evidenced by the TEM and SEM studies. The pyramid and nanorod shapes are also predicted by the KMC model, which incorporates both surface strain and a step diffusion barrier.[61] The diffusion barrier for O adatoms to descend surface steps are by molecular dynamics simulations found to be higher than the barrier for ascending steps, which leads to directional diffusion of O adatoms and a higher oxidation rate at the top compared to the bottom-terraces.[61] Furthermore, the oxide nucleation is observed to preferentially take place at the terrace in the vicinity of a step. Here, the function of the step edge is to act as a reservoir of Cu atoms.

As the initial oxide islands are nucleated, the continued oxidation on Cu(100) takes place through expansion of the islands, promoted mainly by the surface diffusion of oxygen adatoms.[82] At the Cu(111) facet on the other hand, the initial oxide formation is observed to be flat two dimensional rafts, rather than the three dimensional rods and pyramids observed on Cu(100) and (110).[61] Moreover, when comparing the oxidation

rates of the facets, at low oxidation temperatures the oxidation is suggested to proceed the fastest on Cu(100) and the slowest on Cu(111) facets, however, at elevated temperatures (> 600 K) this difference evens out.[61]

To this end, the general model of nucleation processes in material phase transitions, named after Johnson-Mehl-Avrami-Kolmogorov (JMAK),[83] has been applied to describe oxide island nucleation and growth on Cu surfaces[84] and Cu nanoparticles[85]. It captures well the initial superlinear oxide growth rate during nucleation and coalescence of the oxide islands. When we in **Paper III** explore the role of the grain boundaries in individual Cu nanoparticles for the oxidation during the early oxide growth regime, we find that the JMAK model indeed can describe the oxide growth on single crystalline Cu nanoparticles very well, for which we observe a superlinear oxide growth rate.

In the Cabrera-Mott model, it is assumed that the oxide film grows with uniform thickness. The adequacy of this assumption is questioned in the initial oxidation of Cu surfaces in the form of nucleation of oxide islands, which takes place over a large oxygen pressure range (0.5 mTorr - 760 Torr).[86] Instead, Yang et al. suggest that the initial thin film oxide growth is coming to a halt because of the coalescence of the oxide islands, thereby obstructing the oxygen surface diffusion, which they argue is the main promotor of oxide island growth.[86]

3.3.2 Crystal grain boundary influence on oxidation rates

The presence of crystal grain boundaries has been proposed to increase the oxidation rate in Cu due to the enhanced diffusion rate of Cu atoms along the grain boundaries.[65] Specifically, this effect has been observed to increase the oxidation rate of nanocrystalline Cu films compared to coarse-grained films above 300 °C, since at intermediate temperatures the self-diffusion rate of Cu is significantly lower in the Cu lattice compared to along the grain boundaries.[87] However, at high enough temperatures, diffusion through the lattice will become equally fast and therefore, the impact of grain boundaries becomes less significant.[65,66] Furthermore, an enhanced rate of oxidation in nanocrystalline Cu thin films has been observed in oxide films thicker than 20 nm.[88]

The studies mentioned above[87,88] were performed at relatively high oxygen pressure, i.e., 760 Torr and 76 Torr, respectively. This is noteworthy because the oxide island nucleation density is suggested to depend on oxygen pressure, and in the low O_2 pressure regime around 0.5 mTorr, the nucleation of oxide islands has been reported to be preferential to the grain boundaries and to sequentially be followed by a faster oxide growth at the surface-grain boundary intersection.[89] This is in line with our

observations in **Paper V,** where we report a preferential oxide nucleation and increased oxide growth rate at high-angle grain boundaries in Cu nanoparticles during the CO oxidation reaction at low oxygen partial pressure.

To this date, the role of the grain boundaries and whether they either enhance or slow down oxidation kinetics, seems to not be fully understood. Diverging trends are reported for different metals and alloys,[77,90,91] where the oxide growth rate either is increased or decreased with the grain size. Furthermore, oxide growth along the grain boundaries has also been reported, and found to increase the oxide growth rate in the intermediate oxide thickness regime.[88] However, the diversity of grain boundary types, and other system-specific details, such as impurities, diffusion rates or oxygen pressure, may explain why such results cannot easily be translated between systems and studies. Therefore, the partly contradicting results reported for the oxidation of polycrystalline films highlight the importance of studying these effects systematically over a wide temperature and pressure range, as well as for controlled grain boundary types and densities.

My aim of this Section was to give a short but nuanced introduction to some widely accepted concepts, which can be used to describe the oxidation of metal surfaces, and to some more recent developments regarding the validity of these, in some ways, simplistic models. I have tried to cover all ranges of oxidation, from oxide nucleation to thick films, with the focus mainly on nucleation and thin film growth, as well as with the focus on grain boundary effects on oxidation. The introduced models include the Wagner model for diffusion-limited growth, the Cabrera-Mott field approach and the Kirkendall effect arising from the inequality in diffusion rates in a diffusion couple. However, numerous other models exist, about which I have excluded more details for the sake of not being too lengthy. For the interested reader, I strongly recommend the book by Hauffe[66], which provides a comprehensive description of the historically significant findings in the field and the review by Zhu et al.[61] that summarizes recent results on the topic of oxide nucleation.

3.4 OXIDATION OF METAL NANOPARTICLES

The concepts and theories introduced above can be adapted to model also the oxidation of nanoparticles. On a macroscopic scale, the metal bulk is assumed to extend into infinity. However, as we shrink the metal volume, the surface-volume ratio increases dramatically and as such also its significance. As a consequence, the end geometry of an oxidized nanostructure will be determined by its initial morphology and the dominating oxidation mechanism.

A second result of shrinking the size of the structures to the nanometer range, is that the surface curvature of the nanoparticle is of increasing importance and it is therefore predicted to have an influence on the oxidation mechanism.[92] To this end, a curvature effect has been established in nickel (Ni) nanoparticles of sizes below 9 nm, where the larger area of the oxide-gas interface compared to the metal-oxide interface is suggested to promote increased oxygen inward diffusion and oxide growth.[93]

In this Section, I will describe the nanoparticle oxidation models I find most commonly referred to in the literature, i.e., the Cabrera-Mott model for nanoparticles, the adaptation of the Kirkendall effect to nanoparticles, and the Valensi-Carter model for spherical nanoparticles (**Fig. 3.3**).

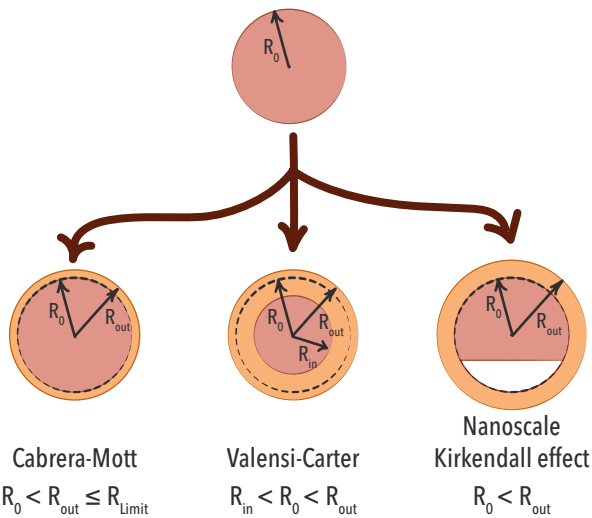

Figure 3.3: Three different pathways for the oxidation of metal nanoparticles. *In the Cabrera-Mott model, a thin, self-limiting (R_{limit}) oxide layer is formed at room temperature due an electric field established across the oxide that drives ion diffusion. The Valensi-Carter model describes the oxidation of a nanoparticle with a net inward mass transport, and thereby a shrinking metal core (R_{in}). The nanoscale Kirkendall effect is characterized by the void formed inside the nanoparticle due to net outward mass transport and the outward growing oxide (R_{out}).*

3.4.1 Cabrera-Mott oxidation model for nanoparticles

The Cabrera-Mott oxidation mechanism introduced above is a concept that can also be considered to describe the oxidation of nanoparticles (**Fig. 3.4**). However, some modifications have to be made to be able to take into account the effect of surface

curvature for nanoparticles with radius $R_0 < 10$ nm. Specifically, it is suggested that the initial oxidation rate of nanoparticles with $R_0 < 10$ nm is increased either due to i) a field strength increase across the oxide due to the spherical geometry,[92,94] or ii) the outer oxide interface area being significantly larger than the inner interface, yielding a higher inward oxygen diffusion rate.[93] Both effects are resulting in a higher net oxidation rate for small nanoparticles compared to larger ones.

In **Paper II**, we have observed the Cabrera-Mott regime during the oxidation of individual Cu nanoparticles ($R_0 \sim 35$ nm) oxidized at 50 °C, where the oxide reaches a limiting thickness of about 5 nm. This is in agreement with previous reports of the self-limiting oxide thickness (R_{limit}) on Cu nanoparticles in the thin film regime.[81,88]

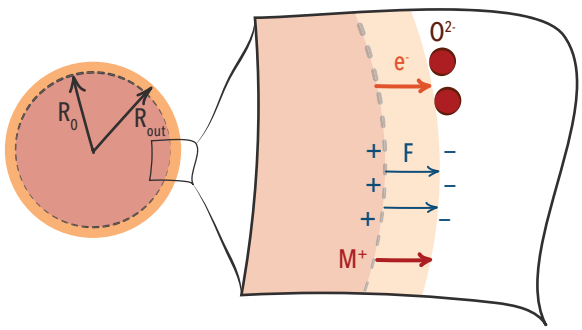

Figure 3.4: The Cabrera-Mott oxidation mechanism for a spherical nanoparticle. *Electrons (e^-) are transported from the metal to the oxide-gas interface, generating an electric field (F) across the oxide, which drives metal ion outward diffusion and promotes outward oxide growth, thereby increasing the particle metal/oxide radius to $R_{out} \leq R_{limit}$.*

3.4.2 Valensi-Carter nanoparticle oxidation mechanism

In the model for diffusion limited oxidation proposed by Valensi and Carter[95], it is assumed that the reactant is diffusing inward through the product. In other words, for the case of oxidation at hand, the oxygen ions diffuse through the oxide to facilitate further oxidation at the oxide-metal interface (**Fig. 3.5**). Hence, it is assumed that the metal particle initially is a sphere with radius R_0, which during oxidation decreases its radius from R_0 to zero.[95] The particle remains solid, since oxidation takes place mainly through inward oxygen diffusion.

In **Paper II**, one of the three oxidation mechanisms we observe for Cu nanoparticles is indeed an inward growing oxide, promoted by the temperature driven diffusion of oxygen ions through the copper oxide according to the Valensi-Carter mechanism.

Furthermore, I would like to mention that there are a couple of reported cases, where this model has been successfully applied to describe the oxidation of spherical micrometer-sized (rather than nanometer) Ni[95] and Pd[96] particles.

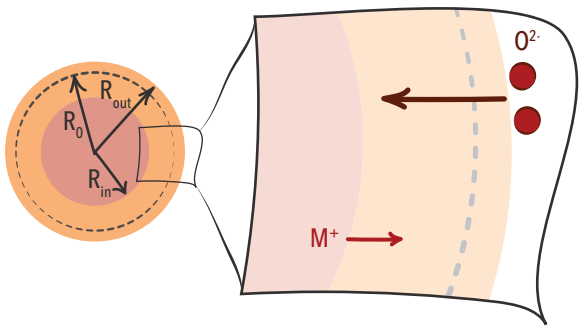

Figure 3.5: The Valensi-Carter mechanism for a spherical nanoparticle with radius R_0. *When the net inward diffusion of oxygen ions (R_{in}) is larger than the net outward metal ion diffusion (R_{out}) through the oxide, the inward growing oxide will constitute the main fraction of the formed oxide shell.*

3.4.3 The nanoscale Kirkendall effect

As discussed above for bulk metals, the Kirkendall effect is a result of the difference in the diffusion rates between two ionic atomic species. In the case of metal oxidation, the oxygen ions usually have a lower diffusion rate through the oxide compared to the metal ions. This is exemplified in **Fig. 3.6** for the case of Cu, where the Cu^+ diffusion is one order of magnitude higher through Cu_2O than the O^{2-} diffusion.

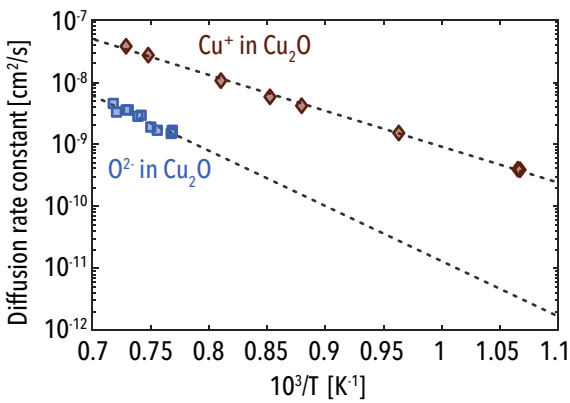

Figure 3.6: Diffusion rate constants of oxygen and copper ions in Cu_2O. *The diffusion rate constant for copper (Cu^+, red diamonds) and oxygen ions (O^{2-}, blue squares) in Cu_2O*

plotted as a function of inverse temperature, indicates an Arrhenius behaviour for the diffusion. Note that the Cu^{+} diffusion rate constant is at least one order of magnitude larger compared to the O^{2-} one. Data for Cu^{+} from ref. [97] and O^{2-} from [98].

For a metal nanoparticle-oxide core-shell geometry, such as that of Cu with a Cu_2O shell where the metal ions diffuse faster through the oxide compared to the O^{2-} species, continued oxidation leads to depletion of metal ions from the metal particle due to the net outward transport of atoms. As a consequence, one or several nanoscale voids form in the core of the nanoparticle (**Fig. 3.7**), this is known as the nanoscale Kirkendall effect (NKE). It was first observed in cobalt (Co) nanoparticles[99] and has since been observed in, among other, Fe[100,101], Ni[93,102], and Cu[103].

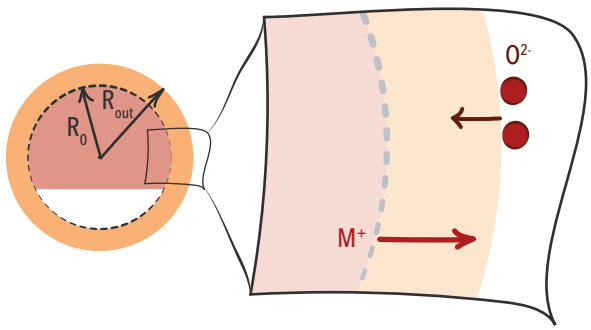

Figure 3.7: The nanoscale Kirkendall effect for a spherical nanoparticle with radius R_0. *For metal nanoparticles where the metal ion diffusion dominates over the oxygen ion diffusion through the oxide, there will be a net outward transport of metal ions, resulting in the formation of a nanoscale Kirkendall void and an outward growing oxide shell (R_{out}).*

During the initial oxidation phase before the formation of a void visible by, for example, TEM, the metal vacancies formed at the metal-oxide interface are likely to form small clusters to reduce the overall interface energy.[103] In **Paper III,** we suggest that in the presence of grain boundaries in Cu nanoparticles, the vacancies likely accumulate at the grain boundaries, and areas of high-grain boundary density that act as nuclei for the formation of nanoscale Kirkendall voids.

From these observations, it becomes clear that at the nanoscale the dominating oxidation mechanism not only determines the rate of oxidation, but also the end morphology of the oxidized nanoparticle. This is exemplified by comparing the NKE during oxidation of Cu and Ni nanoparticles. In Cu nanoparticles, the oxidation results in a homogenous oxide shell thickness all around the nanoparticle (**Fig. 3.8**). However, in Ni nanoparticles, the oxide shell thickness is demonstrated to grow thicker on the side opposite of the initial void nucleation site[93], as sketched in **Fig.**

3.8e.[93] The reason behind this discrepancy is not fully clear to-date. However, it is speculated to be a consequence of the difference in the metal ion diffusion in the oxide between the Ni and Cu systems.[102]

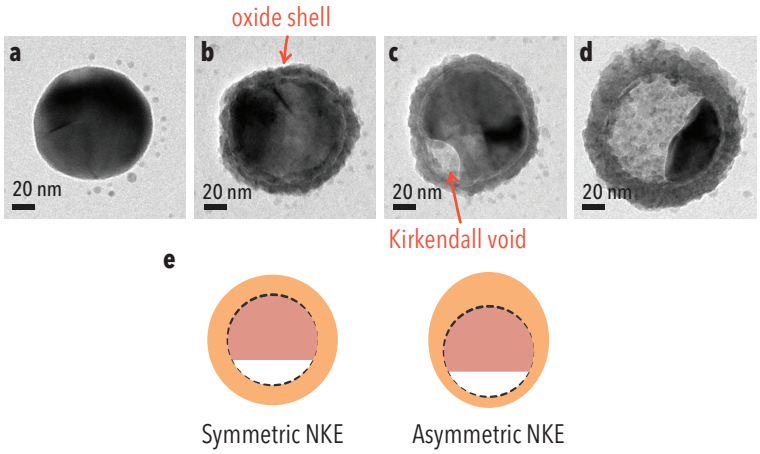

Figure 3.8: Cu nanoparticles at different stages of oxidation. *a) A metallic single crystalline Cu particle. b) An oxide shell has grown on the particles. c) The Kirkendall void has nucleated, and started to grow at the interface between the oxide shell and the metal core. d) The void has grown dramatically and consumed almost the entire Cu particle. e) Schematics illustrating the symmetric NKE, that applies to Cu, and the asymmetric NKE, that applies to Ni nanoparticles.*

The NKE does not only apply to oxidation of symmetric nanoparticles, but as well to other structures, such as nanowires, for which it provides a fabrication protocol for the creation of hollow nanotubes.[104,105] Furthermore, it is not restricted to metal oxidation, but applies to any system where there is a significant difference in the diffusion rates of two elements. In addition to oxidation, the NKE has been demonstrated to occur for reactions between metal nanoparticles and sulfur, selenium and phosphorus.[106] Furthermore, the NKE, together with other fabrication routes for achieving hollow nanostructures, such as galvanic replacement and anion exchange[107], has been explored to produce high-surface-area nanostructures that can find applications in catalysis and nanomedicine.[108]

As far as I know, studies of the role of grain boundaries in nanoparticles and nanostructures during oxidation are scarce, compared to oxidation studies of nanocrystalline metal thin films. In fact, the only study I am aware of focuses on the role of twin boundaries in Cu nanowires.[109] As the main result, it is suggested that

coherent twin boundaries can suppress the formation of Kirkendall voids in Cu nanowires by instead facilitating the oxide growth via a shift of the Kirkendall plane.[109]

The majority of the papers concerning the oxidation of Cu nanoparticles report NKE void formation[103,110–114], similarly to what we report in **Paper I and II**. However, there is one interesting exception in a recent paper employing in situ scanning TEM (STEM) to study the oxidation of Cu nanoparticles at low oxygen pressure,[115] where no NKE is observed. In this study[115], single crystalline nanoparticles of sizes between 6 to 80 nm, were oxidized in 2 Pa O_2 at temperatures between 300 – 500 °C. At these conditions, they observe that the oxide is nucleating at one single site only. The oxidation progresses from this site by a straight oxide-metal interface that is moving across the particle. This alternative oxidation mechanism probably originates from the low oxygen pressure in the experiment. In agreement with the discussion above on oxygen island nucleation, when the oxide is nucleated in one site only, the continued oxidation from this site is energetically favorable.[61]

In **Paper V**, we do observe a similar oxidation pathway with oxide nucleation at only a couple of sites per particle during CO oxidation reaction conditions, with an overrepresentation of grain boundaries as the nucleation sites. As we discuss, this is either a consequence of the low *local* oxygen partial pressure in our experiment due to the continuous oxygen conversion to CO_2 by the CO oxidation reaction, or of the fact that some sites are more catalytically active, meaning that as soon as the surface oxide is formed, it is again reduced to supply oxygen for the catalytic reaction.

As the final comment, I would like to highlight that there are a number of attempts in the literature, which aim at combining several of the mechanisms described above to achieve a more generalized model that can describe the competition of oxidation mechanisms observed experimentally. To this end, both the combination of the Kirkendall and the Cabrera-Mott models[116], and of the Kirkendall and Valensi-Carter models[117] have been suggested for describing the case when both oxygen inward and metal outward diffusion contribute to the oxide growth.

3.5 HYDRIDE FORMATION IN PALLADIUM

As the last part of this Chapter on metal oxide and hydride formation, I would like to focus on the hydride formation process in Pd. This process is highly relevant because of the fast and accurate detection of hydrogen (H_2) required in the ongoing implementation of hydrogen energy solutions. H_2 gas has a wide flammable concentration range in air (4 - 75 %), additionally, it is color and odorless. Hence, a leak cannot be detected by human senses and other means need to be put in place

since it is crucial to detect H_2 leaks early to avoid any accidents.[12] This is where the H_2 sorption and hydride formation process comes into play, since the absorption of H into interstitial lattice sites significantly affects the properties of the host, such as electric conductivity, optical properties and volume expansion. These material property changes observed upon hydride formation makes hydride forming metals, and Pd in particular as discussed below, very interesting materials for H_2 sensors.[57]

I started this Chapter by introducing the concept of surface adsorption of gas molecules on metal surfaces, a process that is also the first elementary step during hydrogen sorption in Pd. Specifically, the adsorption and dissociation of the H_2 molecule has a low barrier and is immediate at room temperature, which is one reason why Pd has become a very popular metal to use in H_2 sensors.[57] The dissociative adsorption is followed by diffusion of the hydrogen atoms into the Pd lattice. The diffusion into the Pd lattice is also rapid at room temperature, and provides the second reason why Pd is chosen for H_2 sensors to be operated at ambient conditions. Other hydride-forming metals, such as titanium (Ti) and magnesium (Mg),[58] does also absorb H_2, however, at much slower rates due to high activation barriers for H diffusion through the metal.

During the early phase of uptake, H occupies interstitial lattice sites in a sparse manner and spreads out evenly in the lattice, essentially without H-H interactions. This stage is known as the α-phase and is depicted in the top left of **Fig. 3.9a.** Subsequently, upon increasing the H_2 pressure, more H will be absorbed into the Pd lattice, eventually giving rise to sizable attractive H-H interactions mainly via strain fields, which leads to the clustering of H. This process constitutes the nucleation of the hydride or the β-phase. The phase transformation is of first order, as reflected by the two-phase coexistence plateau apparent from the corresponding H sorption isotherms (**Fig. 3.9a.**) This plateau exists at temperatures up to the critical temperature of 295 °C,[57] above which the phase transition becomes continuous.

Another effect related to the hydride formation process is the presence of hysteresis between H absorption and desorption. It is the consequence of lattice strain induced by the volume expansion enforced by the H atoms in the interstitial lattice positions.[118] This hysteresis is troublesome for designing H_2 sensors, as it leads to an uncertainty in the sensor readout because in the H_2 pressure range between the ab- and desorption plateaus the senor response will depend on the history of H_2 pressure, i.e., whether the sensor is on the ab- or desorption branch of the hysteresis (**Fig. 3.9b**).

One route that has been explored in recent years to overcome the hysteresis issue in Pd-based H_2 sensors is to alloy Pd with other elements, such as Au. The effect of alloying on the hysteresis is that it can pre-strain the Pd lattice by incorporating the larger Au

atoms. In this way the need to further expand the lattice to accommodate the hydrogen atoms is minimized, and thus the strain-induced energy barrier for forming the hydride phase is reduced compared to pure Pd.[119,120]

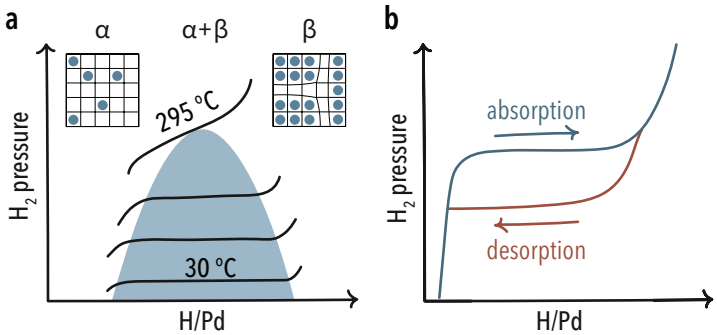

Figure 3.9: Hydrogen sorption in Pd. *a) The phase diagram of hydrogen in Pd indicates that there is an intermediate regime when the α and β phase can coexist in the Pd lattice. When increasing the temperature, the range of coexisting phases shrinks until it disappears at the critical temperature, where the phase transition is no longer first order and becomes continuous. The figure is adopted from ref [57]. b) Hysteresis upon hydrogen absorption and desorption.*

Finally, it is of interest to consider the impact of grain boundaries on the H diffusion in Pd. To this end, the diffusion of H along grain boundaries in nanocrystalline Pd has been reported to be faster in the low H/Pd regime[121] and the α/β-phase transition is reported to extend over a smaller H/Pd solubility range.[31] Hence, higher grain boundary densities lead to increased H sorption rates and the α/β-phase transition onset is shifted to lower hydrogen pressures, and is in this way decreasing the hysteresis. This effect has previously been demonstrated by my colleague Svetlana Aleekseva[31] and in **Paper VI**, we further explore the effect of the grain boundaries on the rate of hydrogen sorption in Pd and demonstrate that the crystallite grain growth induced by multiple hydrogenation cycles can explain the observed slowing of the sorption kinetics over time.

4 HETEROGENEOUS CATALYSIS

When mentioning catalysts, the catalytic converter of internal combustion engines in cars might come first to mind, as it is a frequently used application of catalysis in everyday life. However, there are numerous products we use that are produced partly or entirely using catalysts. Indeed, as much as 90 % of chemical processes employ catalysts to some extent, in order to form products that include fuels, fertilizers and plastic materials, to name a few.[122]

The term *catalysis* was first coined by Jöns Jacob Berzelius in 1835[123], by which he intended to explain the phenomenon that had been observed by several other researchers, among them Elizabeth Fulhame, who in 1794 was first to report observations of a catalytic process.[124] Berzelius proposed that a catalyst exerts an action which "produce decomposition in bodies, and form new compounds into the composition of which they do not enter".[125]

Today, the term catalysis includes both enzymes, that are bio-catalysts which split and create molecular bonds to produce biomolecules in living organisms, and homogeneous and heterogeneous catalysts. The homo and hetero prefix refers to if the phase of the catalyst is equal to that of the reactants or not. Specifically, in heterogeneous catalysis, we most commonly refer to gases (or liquids) that are catalysed over solid surfaces, in particular of transition metals.[35]

In this Chapter, I will limit the discussion to heterogeneous catalysis and briefly introduce the common concepts often referred to in catalysis research. For more in-depth reading on the fundametals of catalysis, I highly recommend the book by Chorkendorff and Niemantsverdriet[35]. I will conclude by discussing the current understanding of the carbon monoxide (CO) oxidation reaction with focus on Cu catalysts, since this is a system relevant to my thesis work.

4.1 CATALYSIS

The basic working principle of the catalyst is to change the pathway in between the initial and final states of the reaction. Physically, this means that a catalyst changes the kinetics of the reaction and not the thermodynamics.[35] A simplified picture of the effect of the catalyst is illustrated in **Fig. 4.1.** The gas phase reaction $A_2 + B_2 \leftrightarrow 2AB$ has a high energy barrier associated with breaking the molecular bonds. In contrast, on the catalyst surface adsorption and dissociation of the gas molecules is facile. The adsorption is followed by the surface reaction, in which the adsorbed species can form product molecules by forming new bonds. As the final step, the newly formed species are desorbed. In this process, the surface atoms provide electrons for breaking and creating molecular bonds, which results in that the activation energy is significantly decreased. Instead of only one reaction step to form the product directly from the gas phase, the reaction undergoes multiple elementary steps, each with an activation barrier that is significantly lower than the gas phase activation energy (E_1 in **Fig. 4.1**). Hence, the catalyst speeds up the reaction rate, typically by several orders of magnitude.[35] The second aspect of the catalyst is that it provides the surface for the reaction to take place. In other words, it limits the reaction space to two dimensions, and thus, the probability of the atoms to meet is greatly increased.

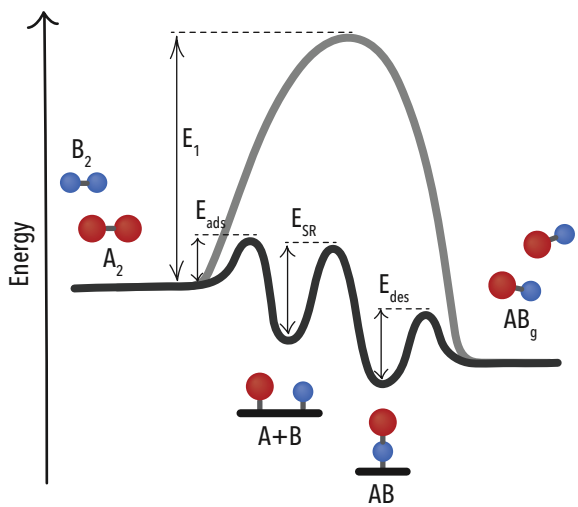

Figure 4.1: The catalytic reaction pathway. *The catalyst lowers the activation energy compared to that of the gas phase reaction, E_1. On the catalyst, the reaction exhibits multiple elementary steps, such as adsorption with activation energy E_{ads}, surface reaction with E_{SR}, and desorption, E_{des}. Figure adopted from reference [59].*

The height of the activation barriers can be calculated by density functional theory (DFT), by which commonly a transition state at the top of the barrier is considered. This transition state is half-way in between two elementary steps, and is obtained by taking into account the vibrations and rotations of the molecular bonds.[35] The reaction rate of an elementary step, $k(T)$, can be described by the Arrhenius equation

$$k(T) = Ae^{\left(-\frac{E_a}{k_B T}\right)} \tag{4.1}$$

where A is a pre-exponential factor, E_a is the activation energy and k_B the Boltzmann constant.[35] Experimentally, an apparent activation energy can be obtained from eq. 4.1. The apparent activation energy is a consequence of different aspects, such as the activation energies of each elementary step and the surface adsorbate coverage. Hence, the apparent activation energy can to some extent depend on the specific reaction conditions.[35]

Based on the above discussion, there are a few basic aspects to consider when choosing a catalyst material. First of all, the *activity* of the catalyst for the specific reaction, which is governed by the interaction between the catalyst surface and the reactants. The interaction has to be strong enough to dissociate the molecular bonds. However, if the interaction between the adatoms and surface atoms is too strong, the adsorbed species will not desorb from the surface, and it leads to so-called surface poisoning. This trade-off is known as the Sabatier-principle.[35] Moreover, often several reaction products can form from the same reactants. The activation energies to form each product over the catalyst surface can be tuned in such a way to selectively produce one product to a larger extent than the other(s).[59] This concept is referred to as the *selectivity* of the catalyst for the specific reaction product.[35]

The concept of surface poisoning connects to the topic of the next Section, as CO poisoning is a well-known phenomenon of platinum (Pt) catalysts in the CO oxidation reaction at low temperatures.

4.2 CARBON MONOXIDE OXIDATION REACTION

As I mentioned in the introduction of the Chapter, the catalytic converter provides an example of a catalyst that we encounter in our daily life. Its purpose is to oxidize carbon monoxide (CO) along with remaining hydrocarbons from the fuel, as well as to reduce nitric oxides (NO_x) to nitrogen gas (N_2). Since both CO and NO_x are poisonous gases, the catalytic converter is crucial for reducing the air pollution from combustion engines.

The elementary steps of the CO oxidation reaction according to the Langmuir-Hinshelwood (LH) mechanism, as is illustrated in **Fig. 4.2**, include:

$$CO + * \leftrightarrow CO^* \quad (4.2)$$

$$O_2 + 2* \leftrightarrow 2O^* \quad (4.3)$$

$$CO^* + O^* \leftrightarrow CO_2^* + * \quad (4.4)$$

$$CO_2^* \leftrightarrow CO_2 + * \quad (4.5)$$

where $*$ denotes an empty surface site and A^* is an adsorbed species. On a Pd catalyst, for example, the surface reaction (eq. 4.4) is the rate determining step at temperatures above the CO desorption temperature.[35] Typically, the surface reaction of CO oxidation has a barrier of about 100 kJ/mol.[35]

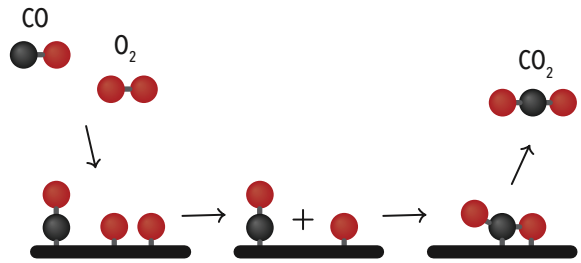

Figure 4.2: CO oxidation elementary reaction steps. *The CO oxidation reaction on a catalyst follows the steps; dissociative surface adsorption of O_2 and associative adsorption of CO, oxidation of the CO molecule into CO_2, and desorption of the newly formed CO_2 molecule. Figure adopted from reference [35].*

Pt, Pd and rhodium (Rh) are all efficient catalysts for CO oxidation and are therefore the main constituents of the active material in three-way catalytic converters.[35,62] However, CO poisoning of the surface due to the high adsorption energy of CO on Pt (> 109 kJ/mol[126]) and Pd (> 142 kJ/mol[126]) surfaces lowers the reaction rate at low temperatures.[35] This problem, in addition to that these metals are rare and thus expensive, opens up for other more abundant metals, such as Cu, to be a viable option for the oxidation of CO at low temperatures.

4.2.1 CO oxidation reaction over copper catalysts

At low temperatures, the CO oxidation reaction can be more efficient using Cu,[56] since the surface does not get poisoned by CO as it does for Pt and Pd, due to the weaker bond between CO and Cu surface atoms [51 kJ/mol on Cu(111)[126]]. The lower adsorption energy also lowers the activation energy of CO oxidation on Cu compared to Pt at low temperatures.[56] In addition to emission control, oxidation of CO is relevant also for the water gas shift reaction[127], which supplies H_2 as one of the reactants in methanol synthesis. Industrially methanol synthesis is conducted over $Cu/ZnO/Al_2O_3$ catalysts[128–131]. However, even though methanol synthesis is a highly relevant topic when discussing reactions over Cu catalysts, I will focus on the CO oxidation reaction only, since I only have studied this reaction in my thesis work.

Due to the ease of oxidation of Cu, it is challenging to characterize the active phase of Cu catalysts during a catalytic reaction. This is likely the reason for the inconsistent reports on the active phase of the CO oxidation reaction over Cu catalysts in the literature. For this reaction, both metallic Cu[56,132] and the first oxidation state (Cu_2O)[133,134] have been reported to have highest activity. However, these observations have to be discussed in terms of the probed reaction conditions. In the first report of Cu oxidation over Cu at atmospheric pressure by Jernigan and Somorjai[56], it is suggested that metallic Cu is the most active phase under conditions when Cu can remain metallic and that the CO_2 conversion decreases when the surface oxidizes. Recently, the same observation was confirmed by in situ UV-vis spectroscopy.[132] In contrast, Huang et al.[133] report that Cu_2O is more active at lower temperatures and at other CO/O_2 ratios, in good agreement also with a more recent study at similar conditions[134].

To this end, recent efforts to better understand the reaction mechanisms of CO oxidation over Cu surfaces, have revealed that CO adsorption reconstructs the Cu surface by pulling out Cu atoms and forming clusters[135,136], in this way activating the surface to allow O atoms to diffuse in under the surface layer.[137] Moreover, the surface can change dynamically during the reaction, to from a thin oxide overlayer, which then is dynamically reduced.[137,138] Hypothetically, we can thus consider a case where the reaction conditions vary slightly over time and the CO content in the gas mixture may increase from stoichiometric to CO-rich to reduce the thin surface oxide to metallic Cu. Alternatively the temperature is (locally) slightly increased and yields a higher oxidation rate and a surface oxide growth. This leads us to the conclusion that depending on the local reaction conditions the catalyst phase may change dynamically and vary across the catalyst bed, similarly to what we suggest in the **Paper IV**, where

we observe Cu particles in a nanoreactor to oxidize at different rates, depending on the local reaction conditions.

As a further aspect, I want to highlight that depending on the exposed surface phase, the CO oxidation reaction may follow different mechanisms. On the metallic Cu surface, the reaction is suggested to follow the LH mechanism (eqs. 4.2 - 4.5)[56,138]. In the LH mechanism, both CO and O_2 adsorb on the Cu surface from where they react to form the product. In contrast, on the oxidized Cu surface, oxygen can be supplied from the surface oxide to form CO_2. Therefore, it is suggested that CO adsorbs on the oxide surface and reacts with an O atom in the oxide surface layer before desorbing and leaving an oxygen vacancy, which is filled by a new oxygen atom.[133,138] This is known as the Mars-van Krevelen (MvK) mechanism. For the MvK mechanism, one step needs to be added after eq. 4.3 to form the surface oxide

$$O^* \leftrightarrow O_{ox} \tag{4.6}$$

and the surface reaction in eq. 4.4 and desorption in eq. 4.5 is combined as

$$CO^* + O_{ox} \leftrightarrow CO_2 + 2* \tag{4.7}$$

where CO_2 is assumed to desorb immediately.[139]

As an alternative route for CO oxidation on Cu_2O, it is suggested that both CO and O_2 adsorb on the oxide surface and that CO reacts with an adsorbed O atom with a lower activation barrier compared to one in the oxide lattice. This would mean that the reaction follows the LH mechanism.[140] Furthermore, it is suggested that lattice strain may change the reaction mechanism.[141] However, as observed in the ETEM study by Luo et al.[137], the reaction on Cu_2O cannot be viewed as simply occurring along one single mechanism, since exposure to CO/O_2 readily converts the crystalline oxide into an amorphous phase, thereby increasing the undercoordination of surface Cu atoms and in doing so also increasing the reaction rate.

In analogy with the previously reported higher CO oxidation rate of metallic Cu surfaces, in **Paper IV** we observe a trend of decreasing CO_2 conversion upon oxidation of the Cu model catalyst. Furthermore, we observe indications of particle-specific behavior despite equivalent reaction conditions. Therefore, we wanted to further corroborate the role of grain morphology during the CO oxidation reaction on single Cu nanoparticles. Hence, in **Paper V** we study the oxidation of Cu nanoparticles during the CO oxidation reaction as a function of their grain morphology and attempt to identify corresponding trends from large single-particle data sets.

5 NANOPLASMONIC SENSING

The research field of nanoplasmonic sensing has emerged over the past few decades, and refers to utilizing the colorful light scattering of metal nanoparticles at their plasmonic resonance for sensing applications. However, practical expertise about how to exploit this beautiful property of metal nanoparticles has existed for thousands of years. For example, this phenomenon is observed in a relic from the time of the Roman empire, the Lycurgus cup (**Fig. 5.1**).[142] It is a beautiful example in which we can observe plasmonic gold and silver nanoparticles, which grant the stained glass its color. Interestingly, they are perceived either as red or green, depending on if the cup is illuminated from the inside or the outside. The reason is that these nanoparticles scatter strongly at the wavelength of green light, and therefore, the green color is lacking in the transmitted light but visible in the scattered light.

Figure 5.1: The Lycurgus cup. *The stained glass appears green when illuminated from the outside (left image) and red when illuminated from the inside (right image). Reprinted from the British Museum.*[143]

In this chapter, I will introduce the phenomenon giving the metal nanoparticles their colorful appearance, which is commonly referred to as localized surface plasmon resonance (LSPR). The corresponding research field is called *plasmonics*. I will then connect the short fundamental description of the LSPR to numerous applications of

nanoplasmonic sensing within materials and catalysis research, and exemplify how I have applied the technique in the study of oxidation of individual Cu nanoparticles.

5.1 LOCALIZED SURFACE PLASMON RESONANCE

The surface plasmon resonance (SPR), also known as the surface plasmon polariton, is a harmonic oscillation of the metal conducting electrons propagating along a metal surface. In a metal nanoparticle, however, the surface plasmon resonance is limited by the geometrical boundaries. Hence, it can no longer propagate and will stay confined within the geometrical boundaries of the nanoparticle as LSPR.

An alternating external electromagnetic field that matches the LSPR frequency of a nanoparticle can couple to its conduction electrons, as illustrated in **Fig. 5.2**, and by collectively displacing them create a dipolar mode (or higher order modes). The dipolar polarizability, α, of a spherical particle can be expressed as[144]

$$\alpha = 4\pi r^3 \frac{\varepsilon - \varepsilon_m}{\varepsilon + 2\varepsilon_m} \qquad (5.1)$$

where r is the particle radius, ε_m is the dielectric constant of the surrounding medium and $\varepsilon(\lambda) = \varepsilon_1(\lambda) + i\,\varepsilon_2(\lambda)$ is the complex dielectric function of the metal. The expression for the polarizability in eq. 5.1 is valid in the limit of small particles[144], i.e. a particle diameter $d \ll \lambda$, where λ is the wavelength of the incident light. In this limit, the applied optical electromagnetic field can be approximated to be static over the particle, and the corresponding theoretical description is commonly referred to as the electrostatic approximation.

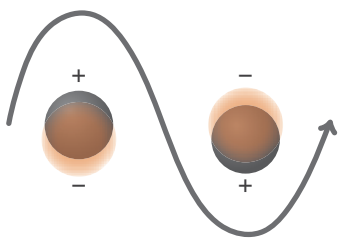

Figure 5.2: The plasmon dipole. *The LSPR in a metal nanoparticle is the collective oscillation of the conduction electrons that is excited by an external electromagnetic field.*

The plasmon dipolar resonance can decay either through radiative scattering or non-radiative (absorption) relaxation routes, such as intra- and interband transitions.[144] The

scattering and extinction cross-sections of the dipole mode in a spherical particle can be derived as[145,146]

$$\sigma_{sca} = \frac{32\pi^4 \varepsilon_m^2 V^2}{\lambda^4} \frac{(\varepsilon_1 - \varepsilon_m)^2 + \varepsilon_2^2}{(\varepsilon_1 + 2\varepsilon_m)^2 + \varepsilon_2^2} \tag{5.2}$$

$$\sigma_{ext} = \frac{18\pi \varepsilon_m^{3/2} V}{\lambda} \frac{\varepsilon_2}{(\varepsilon_1 + 2\varepsilon_m)^2 + \varepsilon_2^2} \tag{5.3}$$

where V is the particle volume. The resonance wavelength of the dipole, for which the extinction and scattering is at its maximum, is found by minimizing the denominator in eq. 5.2 and 5.3 with respect to λ. The damping of the plasmon, described by the imaginary part of the dielectric function $\varepsilon_2(\lambda)$, is small in the visible spectral range for most noble metals (**Fig. 5.3b**)**.** Therefore, only the real part of the metal dielectric function $\varepsilon_1(\lambda)$ is relevant for the resonance condition, which from the denominator gives[144,145]

$$\varepsilon_1(\lambda) = -2\varepsilon_m \,. \tag{5.3}$$

From the resonance condition, we realize that it requires $\varepsilon_1(\lambda)$ to be negative, which is the case for metals (**Fig. 5.3a**) as opposed to insulators/semiconductors, which have a positive dielectric function and cannot support plasmon resonances.

Above, I mentioned that two damping routes of the LSPR are electronic inter- and intraband transitions. This provides us with the explanation for the low plasmon damping in noble metals, since Au, silver (Ag) and Cu have completely filled d-bands that lie well below the Fermi level. Hence, the intraband transition route is not possible. The interband transition energy from the d-band to the Fermi level is 3.9 eV for Ag, 2.4 eV for Au and 2.1 eV for Cu.[147] Therefore, the damping of Cu is slightly larger than for Au and Ag in this spectral range, which we can see as an increase in the imaginary part of the dielectric function. Curiously, the interband transition is also giving bulk Au and Cu its characteristic colors, because most photons below the interband transition energy are reflected by the screening of the electrons. Pd on the other hand, has an unfilled d-band at the Fermi level and lower-energy intraband transitions within the d-band give rise to damping also at lower energies (**Fig. 5.3b**). This inherently higher damping gives a wider line-width of the resonance and shorter lifetime of the plasmon (on the order of a few femtoseconds)[144] compared to Au and Ag, why the latter are the most widely employed metals for plasmonic sensor applications.[145]

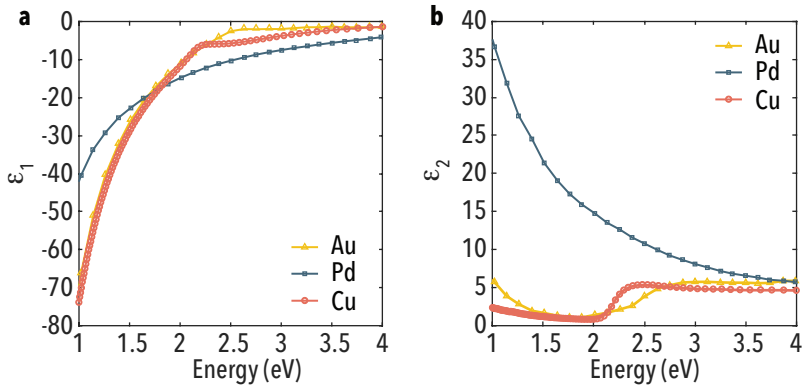

Figure 5.3: Dielectric functions of Au, Pd and Cu. *a) The real and b) the imaginary part of the dielectric function for Au, Pd and Cu. We note that the real part, ε_1, is negative for all three metals, and that the imaginary part, ε_2, of Pd is higher compared to Au and Cu. The dielectric data of Au, Pd and Cu are taken from references* [148–150].

Apart from the intrinsic electronic properties of the metal, scattering of electrons at surfaces and at grain boundaries also contributes to LSPR damping. For example, thermal annealing of metallic nanoparticles to induce recrystallization and grain growth (as discussed in Chapter 2) can increase the line-width of the plasmon resonance. The effect of the annealing is twofold; by grain growth the total grain boundary length is decreased, and during the annealing the volume density of atoms at the grain boundary increases, which gives lower electron scattering probability at the grain boundary.[151] In a similar manner, surface roughness also contributes to stronger damping of the plasmon resonance,[152] which can also be decreased by thermal annealing. In **Paper III**, we suggest that the accumulation of defects, in particular Cu vacancies, at the grain boundaries in polycrystalline Cu nanoparticles as a result of oxidation, is detected as a decrease in the LSPR scattering intensity.

5.1.1 Size and shape effects

So far, we have only considered spherical nanoparticles. With the multitude of nanofabrication and synthesis techniques available, such as colloidal synthesis or electron beam lithography (as is discussed in Chapter 6), it is also interesting to consider how more exotic particle shapes enabled by these techniques affect the LSPR. In extending the scope to more complex shapes, a natural first step from the sphere is to look at ellipsoids, commonly referred to as nanorods.

When illuminating a single nanorod with unpolarized light, the light can couple with two dipole plasmon modes, one along the short and one along the long axis of the nanorod (**Fig. 5.4a**).[145] In **Paper I and II**, we suggest that this dependence of the LSPR

on the shape of the nanoparticle is the explanation for the appearance of the double or even multiple LSPR modes during the oxidation of the Cu nanoparticles, which are induced by increasing the asymmetry of the Cu core during Kirkendall void expansion.

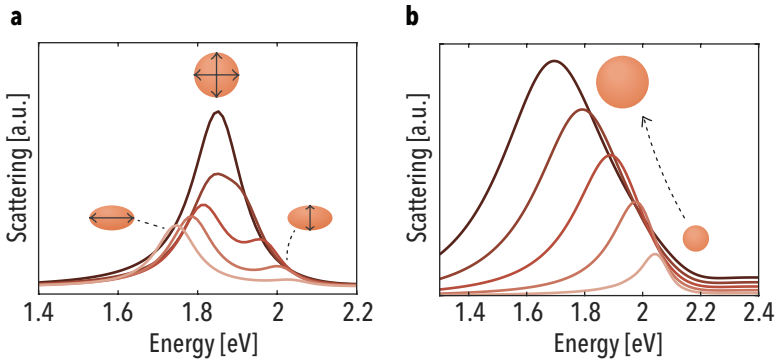

Figure 5.4: LSPR dependence on shape and size. *a) Simulated scattering spectra of a Cu ellipsoid with aspect ratio, AR = 1 and successively increasing AR to a rod-shape of AR = 1.8 that exhibits two distinct resonance modes. b) Increasing scattering cross-section and spectral red-shift of the resonance upon increasing the radius of a simulated Cu disk from 40 to 80 nm.*

When increasing the size of the particles, the assumption $d \ll \lambda$ does no longer hold and the applied electromagnetic field cannot be considered static over the particle. Therefore, phase retardations in the polarized dipole are introduced in particles with $d \gtrsim 100$ nm. These retardation effects are in general inducing a red-shift of the resonance energy, as indicated in **Fig. 5.4b**.[144,153,154]

Furthermore, we can see from eq. 5.2 and 5.3, that the extinction cross-section scales with V and the scattering cross-section scales as V^2. In other words, for small particles with diameter $d \ll \lambda$ absorption is dominating the extinction, but as the particle size increases the scattering cross-section is increasing at a higher rate. Thus, for larger particles with $d \approx 100$ nm, scattering is the dominating factor to the extinction.

As I have demonstrated here in **Fig. 5.4**, finite-difference time-domain (FDTD) electrodynamic simulations are useful for predicting the LSPR of more complex geometries than spheres. I will discuss the FDTD simulation approach more thoroughly in Section 5.3.

5.2 LSPR SENSING

SPR and LSPR based sensing techniques were initially developed from existing biosensing techniques, such as ELISA protocols, that utilize antigen functionalization

to detect specific antibodies.[145] These sensing applications exploit the strong extinction of coupled light at the plasmon resonance and in particular the dependence of the resonance condition $\varepsilon_1(\lambda) = -2\varepsilon_m$ on the surrounding medium. From the Drude model of the dielectric function, the wavelength at the resonance condition λ_{peak} is approximated as[145]

$$\lambda_{peak} = \lambda_p\sqrt{1 + 2\varepsilon_m} \tag{5.5}$$

where λ_p is the bulk plasma wavelength. The dielectric constant relates to the refractive index, n, of the medium as $\varepsilon_m = n^2$. Hence, $\lambda_{peak} \propto n$, and changes in the surrounding medium's refractive index (RI) can be detected as a shift of the resonance wavelength.

Experimentally, the LSPR is measured as a peak in the extinction spectrum, and three peak descriptors are commonly employed to quantify the changes in the LSPR during a sensing experiment, namely the resonance wavelength λ_{peak}, the extinction at the resonance peak and the damping by measuring the line-width (**Fig. 5.5**). When employing LSPR for example in biosensing, an increase in the RI of the medium surrounding the plasmonic nanoparticle is detected. Typically, Au or Ag nanoparticles are employed in biosensing applications, as they support strong plasmon resonances in the visible region of the spectrum. Au is specifically preferred thanks to its chemical inertness.

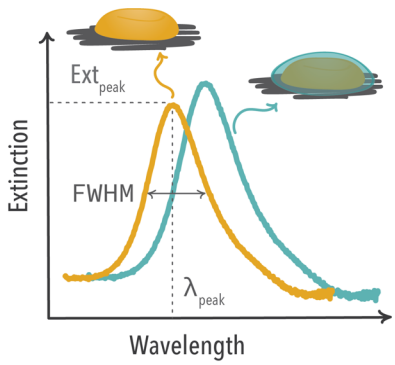

Figure 5.5: The LSPR sensing principle. *Either the peak wavelength λ_{peak}, the peak extinction (Ext_{peak}) or the fullwidth-at-half-maximum (FWHM) can reflect a change in the surrounding of the nanoparticle.*

Practically, the light extinct at the plasmon resonance of an ensemble of millions of plasmonic nanoparticles is sizable enough to be detected by a low power light source and a simple spectrometer to enable efficient quantitative analysis of changes to the

LSPR peak. Even a simple light emitting diode and a CMOS or CCD chip for photodetection can be used and enable handheld sensing devices.[155]

However, when for example attempting to use plasmonic sensing for the detection of single molecules, it is necessary to isolate the readout from individual plasmonic nanoparticles. Thanks to their large scattering cross-section at the LSPR this is possible by means of DFSS using an optical microscope.[156] However, as the scattering cross-section scales as V^2, the amount of scattered light decreases fast with the particle size, which limits the study of individual plasmonic nanoparticles by DFSS to particle sizes > 50 nm.

5.2.1 LSPR sensing on single plasmonic nanoparticles

As was exemplified above for biosensing, it is also in materials and catalysis research of interest to study individual nanoparticles to avoid ensemble averaging of particle-specific morphological properties, such as size, shape and faceting or as of interest in my thesis, crystal grain morphology, to establish single particle morphology - function relations. Hence, in the following Section, I will introduce a couple of techniques, that make it possible to probe the LSPR of individual nanoparticles and apply single particle plasmonic sensing in the context of materials science and catalysis.

Techniques to probe the plasmon resonance (of single nanoparticles) are categorized either as far-field or near-field techniques, depending on how they couple to the plasmon resonance. The near-field techniques are characterized by a high spatial resolution. Some commonly applied near-field techniques include; i) scanning-tip optical near-field microscopy[157,158] (SNOM), which applies plasmon excitation by light illumination from a tip in the near-field and provides spatial resolution of 50 – 100 nm[159], ii) photoelectron emission microscopy[160] (PEEM), which employs ultraviolet and X-ray photons to excite the plasmon and the emitted photoelectrons from the plasmon relaxation are detected, iii) cathodoluminescence[161,162] (CL) and iv) electron energy-loss spectroscopy[163,164] (EELS) where both employ plasmon excitation from an electron beam and thus achieve high spatial resolution. In the CL technique, the photons from radiative plasmon decay are probed, whereas in EELS it is the electron energy-loss due to excitation of the plasmon resonance that is probed (EELS is further discussed in Chapter 6).

In contrast, far-field techniques couple to the plasmon resonance in the far-field and are, thus, inherently diffraction limited. Hence, the spatial resolution is limited to a few hundred nanometers. Examples of commonly used far-field techniques are; i) photothermal imaging[165], by which light absorption is probed by thermal imaging of the surface, ii) surface enhanced Raman spectroscopy[166,167] (SERS) where the plasmon

is coupled to in the far-field, however, the near-field enhancement is exploited in order to increase the Raman scattering, and iii) DFSS, where only light scattered from the nanoparticles is collected by means of a dark-field condenser and dispersed into its spectral components.

DFSS and DF imaging are the optical techniques that we have employed to study individual Cu and Pd nanoparticles in the majority of my thesis work. Therefore, I will discuss these techniques in more depth in Chapter 7. These techniques are applied in all papers, except for **Paper II,** where we study the LSPR of oxidizing Cu nanoparticles by means of EELS. When comparing the results from coupling to the LSPR, both by optical photons in the far-field (**Paper I**) and by high energy electrons in the near-field (**Paper II**), we find that the probed plasmon resonance signals during Cu nanoparticle oxidation agree nicely between both methods.

5.2.2 LSPR sensing of metal-gas interactions

The ability of noble metal nanoparticles to support plasmon resonances is not limited to Au and Ag. Other metals, such as Cu[168], Pt[169], Pd[169], aluminum (Al)[170] and magnesium (Mg)[171] can also support plasmon resonances in the visible spectrum. The plasmon resonances of these more "unconventional" plasmonic metals have been exploited for bringing LSPR sensing into the field of materials research and catalysis, with one of the earliest applications being the sensing of hydrogen sorption in Pd nanoparticles.[172] Hydrogen sorption in Pd has since then been extensively studied in our research group in order to optimize Pd-based H_2 sensors.[119,173] In this quest for more efficient hydrogen sensors, plasmonic nanoalloys have been developed and found to have interesting properties, such as suppressed hysteresis, enhanced H_2 absorption and desorption kinetics,[119,120] as well minimized CO poisoning.[174]

More recently, LSPR sensing has also been explored in efforts to track the oxidation in ensembles of Cu nanoparticles in situ, both by using the plasmon resonance of the Cu nanoparticles themselves (direct sensing)[110,175] or using an inert nanoparticle with stronger plasmonic resonance as adjacent optical transducer (indirect sensing)[111] (**Figure 5.6**)**.** For studying Cu oxidation, an inert plasmonic "antenna" can be added to retain a strong plasmonic signal when the Cu nanoparticles "lose" their plasmonic properties (and thus their large scattering cross-section) when the metallic Cu is transformed into oxide. Moreover, using an optical antenna opens up to study smaller particles (~ 10 – 20 nm).[111] The indirect sensing approach has also been applied for studying hydrogen sorption in Pd[176], as is illustrated in **Fig. 5.6**, and in catalysis[177,178].

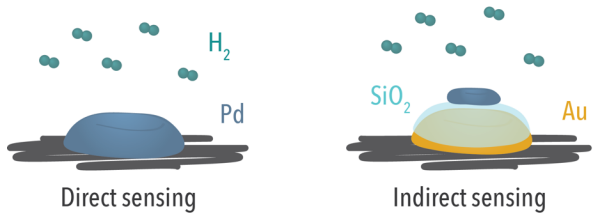

Figure 5.6: Direct and indirect LSPR sensing. *The direct sensing approach (left) – any changes in or in the close vicinity of the particle are monitored, here exemplified by hydrogen sorption in Pd. The indirect sensing approach (right) – an inert antenna particle (typically Au) is probing changes in a closely adjacent, usually smaller, second nanoparticle (here Pd) that is separated from the antenna by a thin dielectric layer, which typically consists of SiO_2.*

In this thesis, I have exclusively used the direct sensing approach, since it is more sensitive to minute changes in the studied particles, as exemplified in **Paper III**, where we detect vacancy accumulation at the grain boundaries of single Cu nanoparticles during the initial phase of oxidation. Another advantage of studying metal-gas interactions in situ using LSPR sensing is that it is minimally invasive, e.g., compared to electron microscopy, which makes it very suitable to study reaction kinetics. At the same time, as a major drawback, it often requires complementary experiments with other techniques since the LSPR readout is non-specific (i.e. just a change of the peak in a spectrum). In principle, the non-specificity means that several different morphological changes could give approximately the same response. Therefore, the use of complementary methods, specifically TEM, which is discussed more deeply in Chapters 7 and 8, together with electrodynamic simulations to quantitatively reproduce the optical response of the structural transitions observed by TEM is essential.

5.3 FINITE-DIFFERENCE TIME-DOMAIN SIMULATIONS

One tool that I have applied widely in this thesis work to generate understanding of the unspecific readout of plasmonic sensing is electrodynamic simulations using a finite-difference time-domain (FDTD) solver. To this end, the scattering and extinction cross-sections calculated by Mie theory can analytically describe the interaction of a spherical nanoparticle with electrodynamic fields.[147] However, Mie theory cannot explicitly describe more complex particle shapes, which means that to understand and validate the LSPR response of other particle shapes and sizes, numerical electrodynamic simulations are necessary and commonly applied to both qualitatively and quantitatively analyze experimentally observed plasmonic sensing response.[179]

Two commonly applied methods for simulating the interaction of nanoparticles or other nanoarchitectures with electromagnetic fields are the FDTD approach and the discrete dipole approximation (DDA)[180]. DDA is thoroughly explained elsewhere[180,181], but in simple terms, it means to model the interaction of a single nanoparticle or an array of nanoparticles with the electric field by a finite set of coupled discrete dipoles. In the FDTD approach, however, both the interaction with the electric and the magnetic field are calculated from Maxwell's curl equations. The FDTD method separates the differential equations of the magnetic and the electric fields both in space and time.[182] In employing a leapfrog stepping method in time, the magnetic and electric field interactions are calculated alternatingly. The electric field is in this way calculated from the magnetic field response in the previous step, and vice versa. For an in-depth reading on the FDTD method, I recommend the book chapter by Taflove et al. [182]

In my thesis, I have used FDTD as a tool for validating and characterising experimentally observed features in the plasmonic response of the single nanoparticles I have investigated (**Paper I-V**)**.** As an example, I would like to highlight the oxidation of individual single crystalline Cu nanoparticles (**Fig. 5.7**), for which I in **Paper I** tracked the entire oxidation process by employing in situ nanoplasmonic sensing. By then qualitatively and partly quantitatively reproducing the experimental results by FDTD simulations, I was able to explain the experimentally observed plasmon mode splitting as the consequence of an increasing asymmetry in the Cu core of the oxidizing particle, due to the growth of a Kirkendall void.

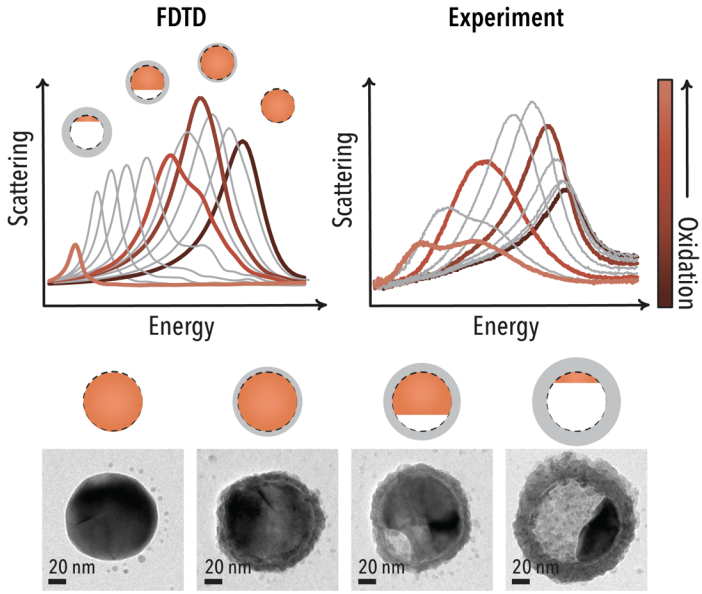

Figure 5.7: FDTD electrodynamic simulations. *When attempting to unravel the physical significance of an LSPR readout obtained during an experiment, FDTD simulations can provide valuable guidance. Here this is illustrated for the spectral LSPR evolution of a single Cu nanoparticle characteristic to the specific geometrical evolution during the oxidation process, where the FDTD results to the left exhibit at first an increasing scattering intensity due to oxide shell growth, followed by mode-splitting and decreasing scattering intensity due to the Kirkendall void expansion – in good agreement with the experimental spectral evolution depicted to the right.*

6 NANOFABRICATION

Through discoveries in the field of nanofabrication, the size of our computers has decreased from filling a whole building to something you can hold in your hand, at the same time as the computer power has increased by more than a million times.[183] This has been possible due to the tremendous development of nanofabrication techniques, some of which I will touch upon in this chapter. This development is something Richard Feynman was calling for already in 1959, when he asked why it was not already possible to write "the entire Encyclopaedia of Britannica on the top of a pin" in his famous talk *There is plenty of room at the bottom*.[184] At this time, the TEM was already invented, and had enabled imaging of structures far smaller than a bacteria.[185] Nonetheless, he had to wait more than two decades until the first scanning tunnelling microscope was developed and opened the door to the world of nanofabrication.[186] Since then, the nanofabrication techniques and instruments have been refined over and over again, in the quest to reach ever-higher control and resolution in terms of feature size.

Fundamentally, one can divide all nanofabrication techniques into two different approaches, that is, either adding structures to a flat substrate, known as *bottom-up* fabrication, or sculpturing structures out of a surface, known as the *top-down* approach. Both fabrication principles have been employed in my thesis work. It has, however, not been focussed around developing nanofabrication techniques and protocols, but rather employing already existing protocols for bottom-up fabrication. Hence, this is where I will put the emphasis of this chapter.

6.1 LITHOGRAPHY

In both bottom-up and top-down nanofabrication, a commonly used fabrication technique is lithography, which in general terms means to reproduce a patterned mask on the substrate, either by depositing new material or etching material. Fabrication

steps common to lithographic methods are; i) spin-coating of a polymeric mask, ii) patterning of the mask by exposing parts of the mask to electrons or photons, or depend on self-assembly of colloidal beads to produce a pattern and iii) wet or dry etching holes through the polymer film to expose the substrate. One example of bottom-up fabrication is to deposit material through a mask to reproduce the pattern on the substrate, followed by mask removal, commonly known as lift-off.

Three common methods of producing a patterned mask are; (i) photolithography, (ii) electron-beam lithography (EBL) and (iii) colloidal lithography. The two former methods provide more precise control of the pattern, whereas in the latter method one is trusting the self-assembly of colloidal beads to produce the pattern, either in the shape of a close-packed array or a less dense quasi-random array. The advantage of using colloidal lithography is that it provides a fast and simple way of covering large areas with arrays of nanoparticles.

Two lithographic techniques, EBL and the specific branch of colloidal lithography known as hole-mask colloidal lithography (HCL), were used to fabricate the samples I have studied in this thesis. Therefore, I will give a more detailed explanation of these techniques following the natural order of the processing steps.

6.1.1 Hole-mask colloidal lithography

The HCL protocol developed by Fredriksson et al.[187] produces quasi-random particle arrays of tapered nanodisks or cones. Impressively, the HCL approach has been further developed to yield also more advanced structures such as layered cones[188], dimer[111] and multimer[189] constellations of particles or core-shell architectures[190]. It was used in this thesis mainly for the samples studied in **Paper II**, which were fabricated on commercial in situ TEM chips (Wildfire, DENS Solution). Typical substrates for HCL made particle arrays are fused silica substrates for visible light transparency or ~ 25 nm thin silicon nitride membranes (referred to as TEM membranes) for electron transparency.

The processing steps of a typical HCL protocol I applied on TEM substrates are pictured in **Fig. 6.1** and include:

a) Cleaning the substrate to remove dust and organic contaminations, typically in acetone, isopropanol (IPA) followed by water or methanol. During cleaning, fused silica substrates are ultrasonicated, which is not applicable and therefore omitted for TEM substrates since the vibrations can tear the silicon nitride membrane.

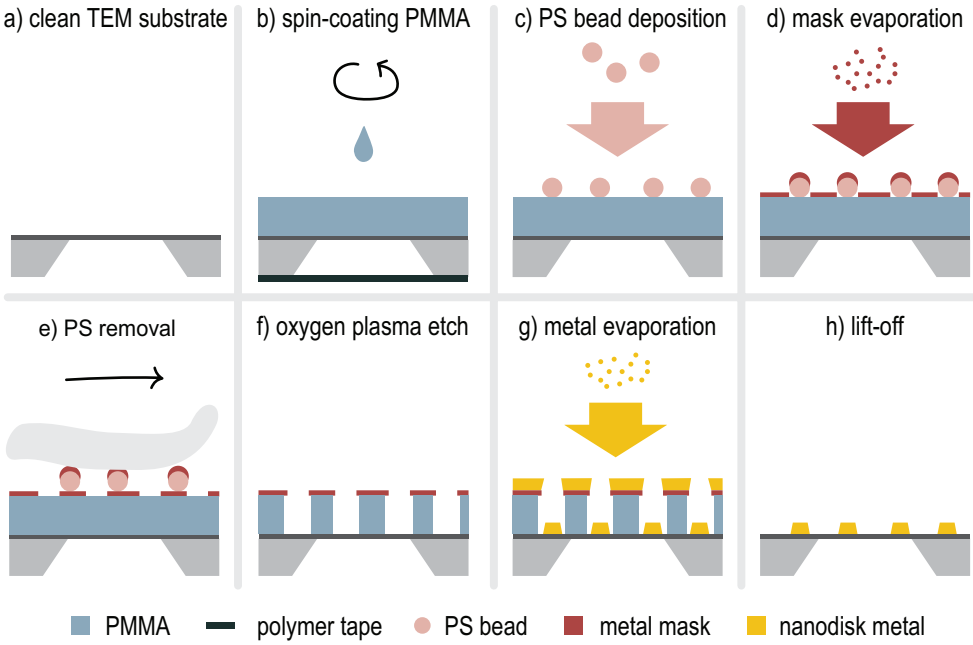

Figure 6.1: The hole-mask colloidal lithography protocol. *In short, the HCL protocol is comprised of the following sequential steps; a) a clean (TEM) substrate, b) polymer mask spin-coating, c) PS bead electrostatic self-assembly, d) metal mask evaporation, e) PS removal by tape-stripping or tissue-wiping followed by f) oxygen plasma etching, g) metal disk evaporation and finally, h) mask lift-off.*

b) Depositing the sacrificial polymeric mask (polymethyl methacrylate (PMMA) A4, MicroChem AB), by spin-coating. On flat substrates, typically 60 s spinning at 2000 rpm are appropriate parameters to achieve an about 200 nm thick film. However, due to the surface topography of the resistive heating film on the in situ TEM substrates, a slightly lower spin rate of 1500 rpm and slow acceleration (500 s^{-2}) are necessary. During spinning, the samples are immobilized by vacuum. Here, the TEM substrates require a rigid polymer film (e.g. thermal tape) to be attached from the backside to enable vacuum immobilization without breaking the membrane. The polymer film is soft-baked at 170 °C for 5 min to evaporate the solvent.

c) Drop-coating to achieve a positively charged polyelectrolyte layer (typically 0.2 wt% poly(diallyldimethylammonium chloride) (PDDA), incubated for 40 s). Analogously, the negatively charged polystyrene (PS) beads (0.2 wt%, 3 min) are drop-coated and attach electrostatically. The beads will distribute randomly with a maximum density defined by the electrostatic repulsion

between the beads. To achieve more sparsely populated particle arrays the PS concentration in solution can be reduced.

d) Growing the 15 nm metal (typically chromium) hole-mask by electron beam physical vapor deposition. The shadowing effect of the PS beads will leave the metal mask with holes defined by the dimensions of the beads.

e) Removing the PS beads to expose the holes in the metal mask, normally by tape-stripping, but due to the fragility of the TEM substrate, it has to be replaced by 20 strokes over the TEM substrates with a wet tissue.

f) Oxygen plasma etching for 5 minutes (50 W, 250 Torr and 10 sccm) to expose the substrate and yield a slight undercut in the PMMA film compared to the metal mask.

g) Thin film deposition of the final nanodisk material, resulting in tapered disks grown directly onto the substrate. The tapering is a result of the shrinking of the holes in the metal mask during evaporation.

h) Lift-off in acetone, for high-density particle arrays this step requires a few minutes, for sparse arrays about 12 h.

6.1.2 Electron-beam lithography

The advantage of beam-writing techniques, compared to colloidal lithography, is that an *a priori* defined pattern can be written with high control. Electron-beam lithography also has higher resolution compared to photolithography, as a consequence of the shorter wavelength of high-energy electrons compared to visible light. EBL enables to focus the electron beam to a spot of a few nanometers[191]. Despite the small probe, the resolution of written features is ~ 10 nm because the resolution is limited by the interaction volume of the electrons scattered in the resist. This effect is known as the proximity effect.[192] Recent development of alternative nanofabrication techniques with resolution comparable to EBL have resulted in nanoimprint lithography, stencil lithography and X-ray lithography, to name a few.[192]

At the general level, the processing steps of EBL (**Fig. 6.2**) are similar to those in the HCL protocol, with the exception being the patterning technique and the chemical development of the mask. Starting from a clean surface, a polymer resist is spin-coated on the substrate. There are two categories of EBL resists; in positive resists the solubility is increased by the e-beam exposure, which results in the exposed areas being removed by the developer. Oppositely, exposure of negative resists increases the polymer cross-linking and decreases solubility, resulting in that the unexposed areas

are removed. After spinning of the resist, it is typically soft-baked to evaporate the solvent.

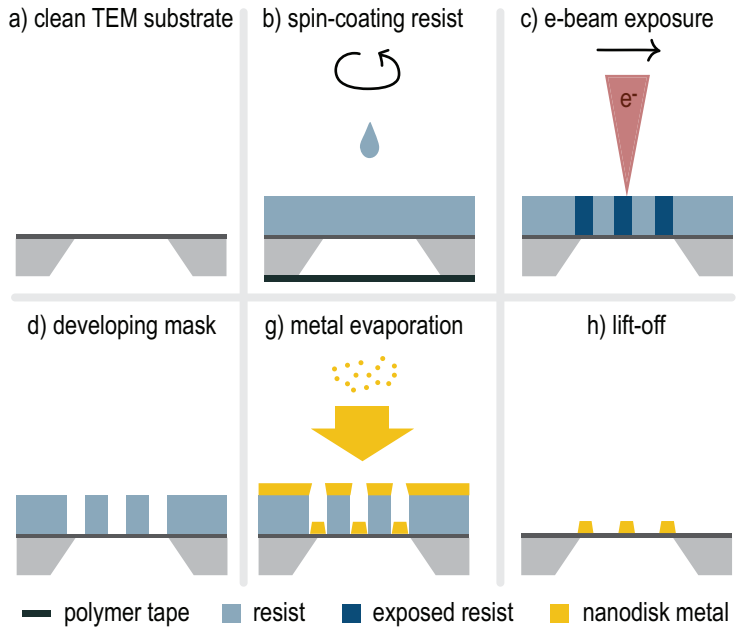

Figure 6.2: The electron-beam lithography technique. *In general, the steps of electron beam lithography are; a) cleaning the substrate, b) spin-coating of a polymer resist, c) e-beam exposure following a pre-programmed pattern design, d) developing the exposed polymer areas, e) metal thin film growth through the mask and f) lift-off.*

During e-beam exposure (**Fig 6.2c**), the *a priori* designed pattern is written into the resist by raster-scanning the e-beam over the substrate. In this way, a highly controlled pattern is obtained, with the possibility of writing practically any two-dimensional feature (> 10 nm). This trait, however, comes at the cost of writing time. Due to the serial nature of the writing process, the areal patterning throughput of EBL is orders of magnitudes lower than with HCL.

The mask is chemically developed by dissolving the (un)exposed areas (**Fig. 6.2d**), through the obtained mask can any material of choice be deposited to achieve the final nanoarchitecture. Analogous to the HCL protocol, typically physical or chemical vapor deposition techniques (discussed in Section 6.2) are employed for the growth of the targeted nanostructures, followed by lift-off of the mask.

The EBL nanofabrication technique has served as a vital tool for the sample fabrication in my thesis, and samples made by EBL are employed in the majority of the papers.

The technology enables well-aligned arrays of particles that increase the throughput of single particle plasmonic nanospectroscopy, which inherently has two requirements; i) the particles need to be well separated to be resolved as individual point sources (a few micrometers apart) and ii) positioned in a straight line. A second advantage of EBL is the ability to fabricate particles of different sizes or shapes on a single substrate, providing the possibility to study them simultaneously, which is exploited in **Paper III**.

In **Paper IV**, the nanochannel architecture was also written by EBL and etched with reactive ion etching. Hence, this is an example of top-down fabrication. Inside the nanochannels, nanoparticles are placed with high precision by EBL. The fabrication protocol of the nanochannel samples are outside of the scope of my thesis and I instead refer the reader to the corresponding papers by my colleagues.[32,193]

6.2 THIN FILM DEPOSITION

Generally speaking, there are two main categories of thin film growth techniques; chemical and physical vapor deposition. The appropriate method to choose depends on the material and the thickness of the targeted deposition. Chemical vapor deposition (CVD) relies on introducing gas phase reactants into the reaction chamber, where the reactants deposit on the substrate and react to form a solid thin film. This is suitable for growing films of dielectric materials, such as nitrides and oxides. As an example from my thesis, the in-house fabricated silicon nitride TEM membranes[194] I widely used, were grown by plasma enhanced CVD.

Metal thin films are usually deposited by physical vapor deposition (PVD), of which the most common techniques are evaporation and sputtering. Evaporation can either be achieved by heating a target by an electron-beam focused onto it or by resistive heating (**Fig. 6.3**). When heated above a critical temperature, the source material evaporates either directly from the solid state, known as sublimation, or from the liquid state, and then moves towards the substrate where it condensates. Moreover, evaporation requires vacuum to reduce the number of collisions of the evaporated species with gas molecules on the way to the substrate and to increase the purity in the grown thin film.

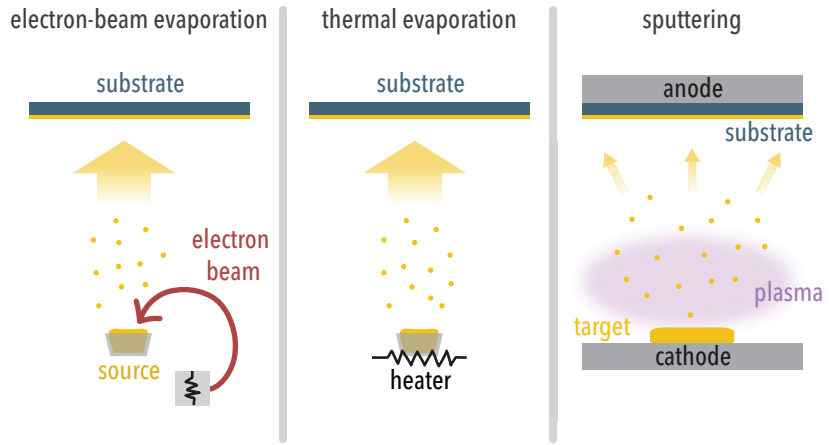

***Figure 6.3: Physical vapor deposition techniques**. Three common methods for physically depositing thin films are electron-beam evaporation, resistive thermal evaporation and sputtering.*

Sputtering is a second commonly used PVD technique (**Fig. 6.3**). Its working principle is based on ionizing an inert gas to a plasma and accelerating it towards a target material, where target atoms are ejected in all directions upon collision. Hence, sputtering is not directional and yields a higher deposition rate than evaporation. By sputtering, a variety of materials can be deposited, such as metals, insulators or alloys. Alloys can with convenience be deposited using a target comprised of two or more materials.[195]

7 MICROSCOPY

Diffraction-limited optical microscopes have been used for several centuries to study biological specimens. However, as nanofabrication techniques have developed to miniaturize electronics and sensors as two examples, together with the quest to detect single molecules has created a need for imaging of objects smaller than bacteria or cells. To this end, various optical microscopes that can image beyond Abbe's diffraction limit have been developed over the past decades, such as the super-resolution fluorescence microscope.

While the development of optical microscopy techniques is impressive, they are still far from the resolution required to resolve single atoms. To eventually achieve this, the electron microscope, which was invented almost one hundred years ago[185], is the technique of choice. With the development of the aberration correction, today, it reaches below 1 Å in resolution, indeed enabling the imaging of single atomic columns and even single atoms[196–198].

Nevertheless, the basic principles of optical and electron microscopy are in many aspects similar. However, fundamentally they are significantly different in the sense that electrons have much shorter wavelengths than optical photons, thereby enabling higher resolution, since the diffraction limit decreases linearly with the wavelength. In this analogy, I have depicted the beam being transmitted through the specimen for both optical and electron microscopy in **Fig. 7.1**. This is true in many optical microscopes, but not in all cases, as we will see in the next section, where I will introduce the dark-field scattering spectroscopy (DFSS). The DFSS is an optical microscopy technique specialized for visualizing the light backscattered from single nanoparticles, and one of the main techniques I have employed in this thesis work.

In transmission electron microscopy (TEM) and scanning TEM (STEM), the electrons are transmitted through the specimen as depicted in **Fig. 7.1**. I have applied both these techniques for nanoparticle imaging in combination with additional analysis methods

available on electron microscopes, namely energy-dispersive X-ray spectroscopy (EDX), selected-area electron diffraction (SAED) and electron energy-loss spectroscopy (EELS). In scanning electron microscopy (SEM), the electrons backscattered from a (bulk) specimen are collected (also diverging from the schematics in **Fig. 7.1**). Nonetheless, I will introduce below a variant of SEM analysis where transmitted electrons are analyzed.

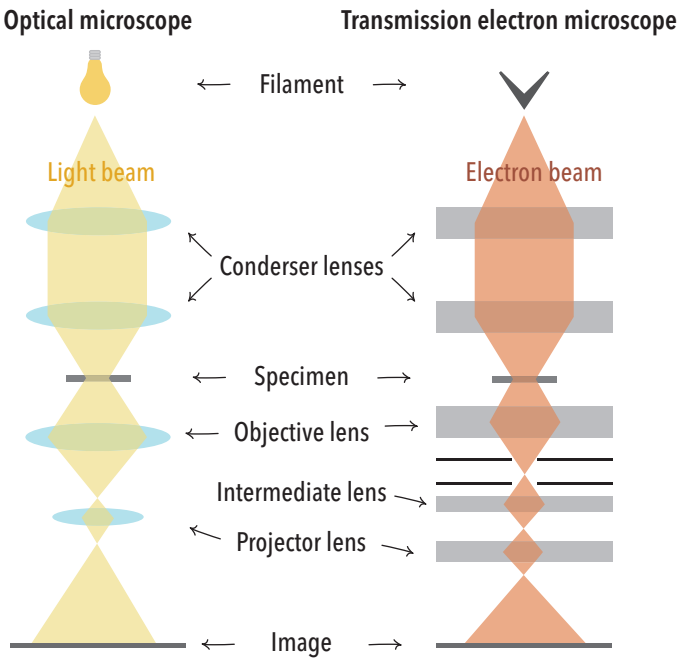

Figure 7.1: The principles of transmission optical and electron microscopy. *The basic principles of transmission optical and electron microscopy (TEM) are fairly similar. In simple terms, the light or electron beam is collimated and focused onto the sample, an image is formed by the objective lens, which is magnified and projected onto a camera or viewing plane by the projector lens. The TEM also commonly features an intermediate lens for switching between the imaging and diffraction mode.*

7.1 DARK-FIELD SCATTERING SPECTROSCOPY

When employing the plasmonic resonance of metal nanoparticles in sensing applications, its spectral change is recorded over time. Typically, in ensemble experiments with samples containing millions of nanoparticles, the plasmon resonance is excited by polychromatic visible light over an area of several mm^2 and the transmitted light is analyzed by a spectrophotometer in the UV-vis-NIR spectral range.

In this way, the extinction of light by the particles, i.e., the sum of absorption and scattering, is analyzed as discussed in Chapter 5. When instead using an optical microscope, the spatial resolution can be increased down to a few hundred nanometers. Hence, the optical microscope enables to analyze light that is scattered from individual nanoparticles, in order to employ plasmonic detection or "sensing" of events as tiny as the binding of a single protein onto the surface of a single plasmonic nanoparticle.[156]

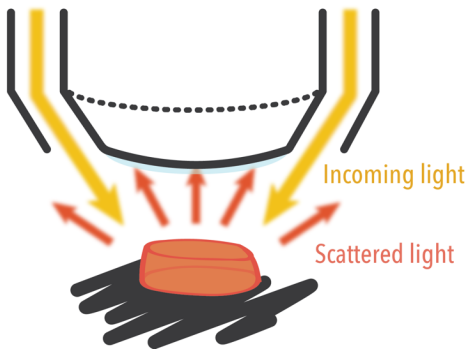

Figure 7.2: Illustration of a dark-field microscope objective for epi-illumination. *The light is incoming towards the nanoparticle at a high angle (high NA of the objective) compared to the normal of the surface. Hence, only light scattered backwards is collected by the objective and the objects that scatter light appear on a dark background.*

The essential ingredient that has to be added to the optical microscope to provide single nanoparticle plasmonic microscopy/spectroscopy, is a dark-field condenser or objective (**Fig. 7.2**). Here, 'dark-field' is referring to that only light backscattered (or emitted, e.g., by fluorescence) from the sample is collected in the objective. Any light that has not interacted with the sample will not be part of the obtained image seen in the eyepiece or collected on the CCD chip. In practice, this is realized by illuminating at a high angle from the surface normal using an objective/condenser with high numerical aperture (NA), as is illustrated in **Fig. 7.2.** In this way, a dark background is achieved in the image and the objects appear as bright point sources of light. The strength of this dark-field scattering imaging method for the detection of small and weakly scattering objects (compared to, e.g., stained cells), such as metal nanoparticles, is exemplified by a true-color dark-field micrograph of seven Cu nanoparticles in **Fig. 7.3a**.

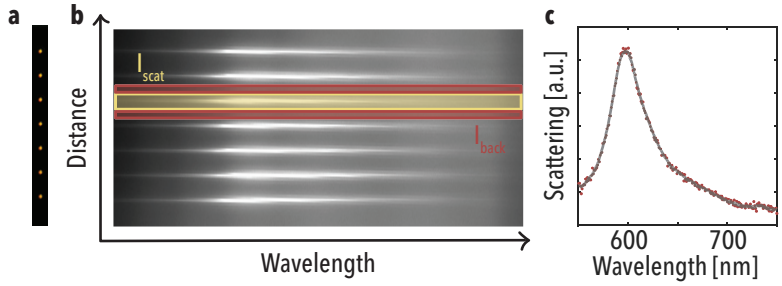

Figure 7.3: The working principle of DFSS. *a) A micrograph of the light scattered from seven Cu nanoparticles with diameter 100 nm and height 40 nm, collected through a dark-field objective of an optical microscope at 50x magnification. b) The light from each particle is dispersed into its spectral components by the grating and collected on a CCD chip, thereby providing an image where the intensity corresponds to the scattered light intensity at each wavelength. c) A scattered light spectrum collected from a single Cu nanoparticle, extracted from the image in (b) using eq. 7.1.*

To enable DFSS, the scattered light collected by a dark-field microscope is coupled to a spectrophotometer with a grating that disperses the collected light into its spectral components. The light is dispersed along one direction on the grating and as such collected horizontally on a CCD chip. Therefore, to measure scattering spectra of several single nanoparticles simultaneously, they need to be aligned in a vertical column aligned to the slit of the spectrometer (**Fig. 7.3b**). From the obtained spectral image, the scattering spectrum of each individual particle is summed in a box termed I_{scat} in **Fig. 7.3b**. The background light scattered by the substrate next to the particles, I_{back}, is extracted from the image and subtracted from the scattering signal of the particle (I_{back} is extracted either from a box below, or by summing a box below and above the particle as in **Fig. 7.3b**). Furthermore, any real light source has a non-uniform distribution of intensity over the wavelength spectrum and the CCD chip can have wavelength dependent sensitivity. Hence, the lamp emission spectrum needs to be deconvoluted from the light scattered by the nanoparticles, I_{scat}. To achieve this, the spectrum of the light source, I_{lamp}, is collected by illuminating a diffuse reflectance standard and used to normalize the light scattered by the nanoparticles. Therefore, we extract the scattered light spectrum from a single nanoparticle as

$$I_{part} = \frac{I_{scat} - I_{back}}{I_{lamp}} \qquad (7.1)$$

The scattering spectrum from a single Cu nanoparticle calculated using eq. (7.1) is depicted in **Fig. 7.3c**. For LSPR sensing applications as discussed in Chapter 5, the descriptors of the resonance peak; the peak wavelength, the peak intensity and the line-

width can be tracked analogously in the scattering spectrum of a single particle as in the extinction spectrum of a particle ensemble.

To obtain the scattering spectrum, the illumination of the grating is required to be along one dimension. Hence, particles have to be placed along a line if multiple spectra are to be measured simultaneously, which limits the number of addressable particles. In practice, this means that a maximum of between 10 – 20 particles can be spectroscopically addressed simultaneously, depending on the size of the CCD chip. For multiplexing purposes, however, this is not enough to gain a good statistical ground. Therefore, with some smart adaptations of the optical setup, spectroscopic measurements of up to 100 particles simultaneously have been demonstrated.[199] Furthermore, by instead resorting to imaging-type readout and analysing changes in spectrally integrated light intensity scattered from the particles, one can simultaneously track the optical response of several hundred particles. For example, the 25 Cu particles imaged in **Fig. 7.4a**, cover less than 1 % of the pixels on the CCD chip of the camera I have used. Hence, there is potential to analyse more than a thousand particles at once, as we demonstrate **in Paper IV**. Here, the temporal evolution of the integrated scattering intensity, ΔI, from the 25 Cu particles demonstrates how the plasmonic nanoimaging approach can be applied in a Cu nanoparticle oxidation experiment (**Fig. 7.4b**), which is one of the focus areas of this thesis.

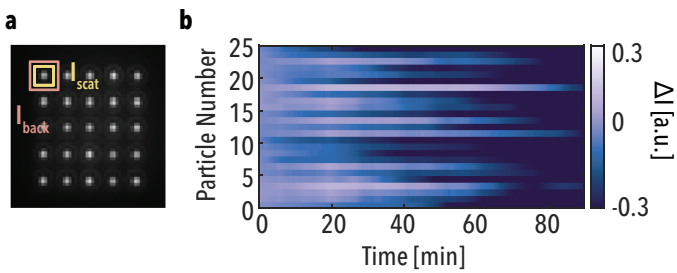

Figure 7.4: Plasmonic nanoimaging. *a) 5 x 5 particle array of 150 nm diameter Cu nanoparticles, where the pixel boxes for intensity integration (I_{scat} and I_{back}) are indicated. b) Time evolution of the integrated scattering intensity change, ΔI, of the 25 Cu nanoparticles during 90 minutes oxidation in 1 % O_2 at 150 °C.*

Finally, I would like to briefly mention that instead of a fixed-grating spectrometer, spectral analysis of the light scattered from single nanoparticles can also be achieved by means of dynamic filters[200], a monochromator[201] or an interferometric optical path[202] that enable to sweep over the relevant wavelength span, in the so-called hyperspectral imaging approach. Therefore, alternatively, either DFSS or hyperspectral imaging can

be applied, depending on if there is a need for high spectral resolution or a high temporal resolution and/or large particle data sets.

In my thesis I have utilized both plasmonic nanospectroscopy by means of DFSS and plasmonic nanoimaging in different papers, dictated by the purpose of the work. In **Paper I**, I wanted to corroborate the spectral evolution of the single Cu nanoparticles until full oxidation. Hence, it was relevant to have high spectral resolution to follow the evolution of the scattering spectra during oxidation. In **Paper III-VI**, it was necessary to study a large particle data set in order to reveal trends in the particle – gas interaction dependence on the particle morphology. Hence, I used the nanoimaging concept.

7.2 ELECTRON MICROSCOPY

To visualize objects is indisputably helpful for revealing more details about their morphology, shape and size. Therefore, electron microscopes are frequently employed for imaging of nanometer-sized objects. Moreover, the instruments can provide a spectrum of additional analysis techniques besides imaging, such as chemical analysis and lattice diffraction. In this chapter, I will introduce some of these analysis techniques, which are of relevance for my thesis. Since I will only be able to give a short introduction to the relevant instruments and operational modes, for the reader interested in more in-depth information, I recommend the pedagogical book by Williams and Carter[203].

As visualized in the conceptual schematic introducing the Chapter topic (**Fig. 7.1**), we can in simplified terms consider the working principles of the optical and electron microscope to be fairly similar. The lenses above the sample in the beam path serve to collimate and focus the beam, whereas the objective and projector lenses serve to image, magnify and project the image onto the camera or eyepiece/viewing screen.

As already mentioned, electron microscopy has an inherently higher spatial resolution compared to optical microscopy. This is because the resolution is diffraction limited by the so-called Airy disk, whose size depends on the wavelength of the beam.[203] Accordingly, since electrons accelerated to energies of tens or hundreds of kilo electron volts (keV) have wavelengths in the picometer regime, this length scale is comparable to the size of atomic nuclei and atomic resolution can be achieved.[203]

The electron beam is interacting with the specimen either through elastic or inelastic scattering, which is mainly directed forward in thin samples and backward in thick or bulk specimen. The interaction can result in a number of processes (**Fig. 7.5**). First, an atomic core-electron can be excited or ejected from the atom, as a result of the

interaction with the beam. The eject electron is known as a secondary electron. Sequentially, an Auger electron or characteristic X-ray photon is emitted when the excited electron is relaxed or the hole after the secondary electron is filled from a higher electron shell.[204] Additionally, interaction between the beam electrons and the atomic nuclei results in a continuum of X-rays, known as Bremsstrahlung. Other interactions, such as plasmon excitation, interband transitions or excitations above the band gap in semiconductors may result in emission of UV-vis photons. The cross-sections for these interactions decrease as the energy of the beam increases. The interaction depth of 10 keV electrons (usual SEM beam energy) in bulk Au has been calculated to about 100 nm by Monte Carlo simulations (CASINO v2), compared to > 10 μm at 200 keV (common beam energy in TEM).

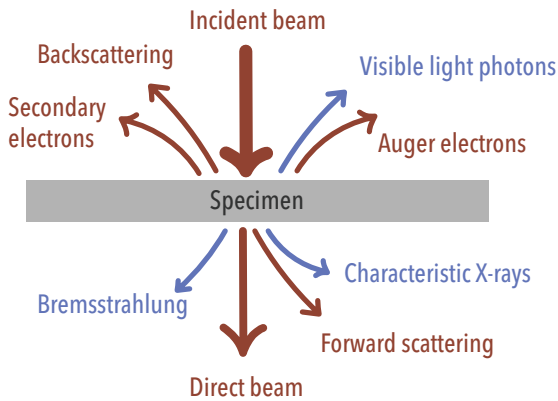

Figure 7.5: Emissions from electron – matter interaction. *Beam electrons (red lines) can both scatter elastically and inelastically upon interaction with the specimen. Secondly, inelastic interactions can result in ejected electrons (secondary or Auger electrons) from the specimen or emitted photons (blue lines), with energies either in the X-ray or optical spectral range.*

Secondly, the interaction cross-section with the incoming electron beam increases with the atomic mass in the specimen. Hence, lighter elements have a lower scattering cross-section, therefore, common materials employed as substrates for TEM studies are holey carbon grids and thin membranes of Si_3N_4 or SiO_2. The interaction depth in Si_3N_4 of a 200 keV electron beam is > 100 μm, one order of magnitude larger compared to Au. However, the more the beam interacts with the sample, the more the spatial resolution is decreased and therefore one usually strives for as thin TEM samples as possible, preferably < 50 nm.[203] At the same time, the interaction of the electron beam with the sample is not entirely undesired, since it enables chemical analysis by electron energy-loss spectroscopy (EELS) or energy dispersive X-ray spectroscopy (EDX), as well as

various electron diffraction methods. In this Section, I will briefly introduce the different electron microscopy techniques and analysis methods that I have employed.

7.2.1 Transmission electron microscopy

In a TEM, magnetic lenses bend the path of the electrons similarly to how optical lenses bend light rays.[203] The magnetic lenses usually consist of a copper coil and iron pole pieces, the pole pieces are the inlet and outlet holes of the lens. The number of lenses varies between different microscope models. The basic lenses, as depicted in **Fig. 7.1,** are the condenser lenses to collimate and focus the beam from the electron gun and the objective lenses used for imaging. Commonly, there is one objective lens above and one below the specimen holder stage. In connection to the lower objective lens, there is the objective aperture, by which one can chose to collect only the direct beam or scattered beam paths, respectively. Below that aperture, the so-called intermediate lens is localized, which is used to shift between the two operational modes; imaging and diffraction. At the bottom of the column, there is a set of projection lenses to view the image either on a fluorescent screen or on a CCD camera.[203]

The TEM image is built up of the electrons transmitted through the sample. As already discussed, the extent of the interaction with the specimen depends on the atomic number and the thickness of the specimen. Hence, thin areas with light atoms transmit more electrons and appear bright in the image. Oppositely, thick areas or areas with heavy atoms, appear dark. The third factor that affects image intensity is electron diffraction. Specifically, diffraction of the electron beam on a crystal lattice gives rise to interference patterns, which at high resolution become visible as so-called "lattice fringes", which is the image of atomic columns in the crystal lattice. Moreover, dislocations, stacking faults, grain boundaries, thickness variation[205] and strain[206] can result in diffraction of electrons and thus give rise to different contrast in a TEM image. We can see examples of diffraction contrast from probable grain boundaries and strain in the polycrystalline Cu nanoparticle depicted in **Fig. 7.6a,** and at high magnification (1 Mx) we observe lattice fringes, revealing an interplanar distance of around 2.08 Å from diffraction in the Cu(111) plane (**Fig. 7.6b**).

In a crystalline sample, electron diffraction follows Bragg's law for diffraction in periodic lattices, which reads as

$$n\lambda = 2d\ sin\,\theta_B \qquad (7.2)$$

where the n is the order of the diffraction, λ is the wavelength, d is the interplanar distance and θ_B the diffraction angle.

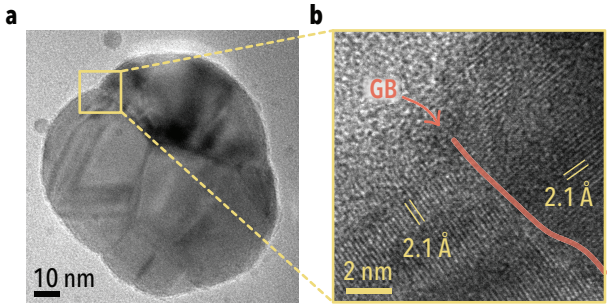

Figure 7.6: A TEM image of a polycrystalline Cu nanoparticle. *a) A 100 nm Cu nanoparticle imaged in bright-field TEM mode. b) A high magnification zoom-in at the position marked by the yellow box in a), displaying closely the grain boundary (red line) at the center and lattice fringes in both grains, with a distance corresponding to the interplanar distance of 2.08 Å in the Cu(111) lattice planes.*

One method for studying the diffraction pattern of a crystalline sample is to insert an aperture beneath the objective lens (in the back focal plane) to select the diffraction from a specific area. Hence, this technique is known as selected-area electron diffraction (SAED). Single crystalline samples exhibit a single spot diffraction pattern and polycrystalline samples display rings around the direct beam, with distances corresponding to the interplanar distances of the possible diffraction planes. A second method is the convergent beam electron diffraction (CBED), which by means of a focused beam results in diffraction from an even smaller area. The obtained diffraction pattern from CBED is more complex compared to SAED and contains more information about the crystal than a spot diffraction pattern.[207]

The magnetic lenses used in a TEM, in analogy to optical lenses, experience some aberration effects. Specifically, since the lens is finite in size, rays refracted at the edge of the lens are more strongly focused compared to those refracted at the center. The result is that the focused spot is a disk with some finite radius. This is known as spherical aberration and is limiting the resolution of the TEM. However, nowadays there exists spherical aberration correction, which is working as a concave lens that diverges the off-axis rays. In reality, this is achieved by a set of computer-controlled quadrupoles and hexa/octupoles. The aberration correction is necessary to achieve sub-Ångström resolution.[203,208]

The second type of lens aberration, chromatic aberration, is the frequency-dependence of the focal length.[203] Again, since aberrations distorts the focus spot, the resolution of the instrument is decreased. However, most of the chromatic aberration arises when the beam interacts with the specimen, and as such it is most easily averted by decreasing the sample thickness. The exception is that when employing electron

energy-loss spectroscopy (EELS, as discussed in the following Section) monochromators are useful to achieve a higher energy resolution in the EEL spectrum. Furthermore, imperfections in the lenses and apertures lead to astigmatism. However, fortunately, this is dealt with by the stigmators, where one is commonly found among the condenser lenses and one among the objective lenses.[203]

7.2.2 Scanning transmission electron microscopy

In addition to the standard TEM imaging mode, by which the image is acquired by a close-to parallel beam, there is the scanning TEM (STEM) imaging mode. In contrast to the TEM mode, in STEM mode images are acquired by scanning a tightly focused beam over the sample and the electrons making up each pixel are collected in a sequential fashion. In this way, no lenses are involved in obtaining and magnifying the image, only for focusing the beam. Therefore, no chromatic aberrations occur in STEM, which is advantageous for imaging thick samples.[203]

With STEM, it is also possible to acquire both bright-field and dark-field images, by either collecting the direct beam or the diffracted beam with an annular dark-field (ADF) detector. In ADF-STEM imaging, the diffraction contrast is less than in TEM images (**Fig. 7.7**), and to achieve only thickness and atomic number (Z) contrast, the electrons scattered at even higher angles are collected by a high-angle ADF (HAADF) detector.

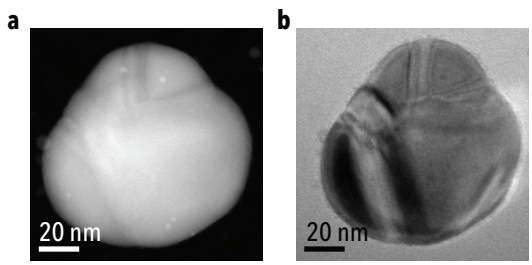

Figure 7.7: Dark-field and bright-field imaging. *a) A dark-field image acquired by ADF-STEM of a Cu nanoparticle. b) A TEM bright-field image of the same nanoparticle, displaying more diffraction contrast in form of darker and brighter areas compared to the ADF-STEM image in a).*

Thanks to the STEM scanning the beam across the specimen, it can provide mapping of chemical phases with high spatial resolution using either energy-dispersive X-ray spectroscopy (EDX) or electron energy-loss spectroscopy (EELS). By the EDX technique, the characteristic X-rays are detected. These X-rays are emitted either as a consequence of the relaxation of an excited core-electron or when the hole after a

secondary electron is filled from an outer shell. Hence, the energy of the X-ray photon is specific to each element and can be used for identification and quantification of elements in the specimen with nanometer spatial resolution. The spatial resolution is limited by having a large enough STEM probe to detect enough X-rays and by the X-ray interaction volume.[203] In **Fig. 7.8a**, we can see an example of an EDX spectrum obtained from an alloy AuPd nanoparticle. By collecting the X-ray spectra while scanning the beam, an elemental map of an area of the specimen can be obtained (**Fig. 7.8b,c**). The emission of characteristic X-rays is more likely from heavy atoms. Hence, EDX elemental analysis is not appropriate for detecting light atoms. In addition to the characteristic X-rays originating from the sample, one will also observe the continuum Bremsstrahlung background in the X-ray spectrum and eventual artifact X-rays from the sample holder or other parts surrounding the sample.

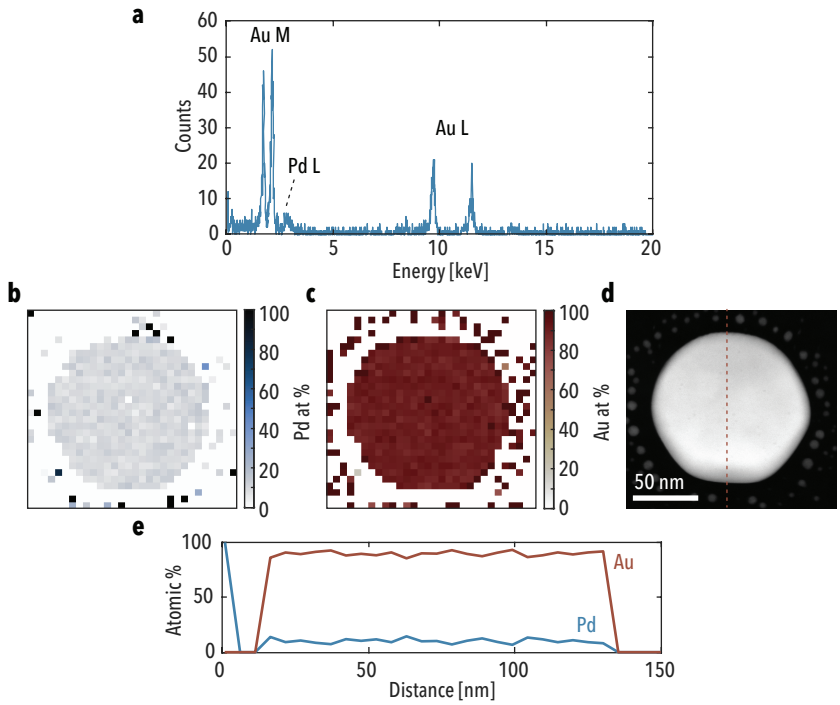

Figure 7.8: EDX analysis of an AuPd alloy particle. *a) EDX spectrum obtained from one point in the map of an Au 90 % / Pd 10 % alloy particle. b) The Pd and c) Au atomic percentage maps obtained by EDX analysis from the particle in d). e) The atomic ratio in a line scan across the particle as indicated by the dashed line in d).*

Elemental analysis similar to EDX is also possible to achieve with EELS, by which, instead, the electron energy-loss of the forward scattered electrons are analyzed. The

zero-loss peak in the EEL spectrum is most prominent (inset in **Fig. 7.9a**), and stems from the direct beam and elastically scattered electrons. Next to the zero-loss is the low-loss part of the spectrum (< 50 eV, **Fig. 7.9a**), where energy losses from interaction with inter- and intraband transitions, band gap excitations in semiconductors and excitations of plasmon resonances are observed. In the high-loss region of the spectrum, we find energy losses from interaction with specimen core-shell electrons that are either excited to higher shells or ejected (**Fig. 7.9b**), which can provide elemental mapping similarly to that obtained by EDX. The core-loss is observed in the EEL spectrum as an edge, rather than as a peak with a decreasing background, this is because electrons may be subject to multiple inelastic scattering events. Due to the background of plural-scattering events, the EELS elemental analysis is more complex compared to EDX. However, as the X-ray yield of light elements is very low, EELS is still the best option for mapping of light elements.[203] Finally, fine structure peaks due to chemical bond effects or oscillations of neighboring lattice atoms can also be resolved. Hence, in addition to elemental quantification, the core-loss edge can provide information about chemical bonds and the oxidation state(s) of the specimen. Consequently, there is more information contained in the EEL spectrum compared to the EDX spectrum.

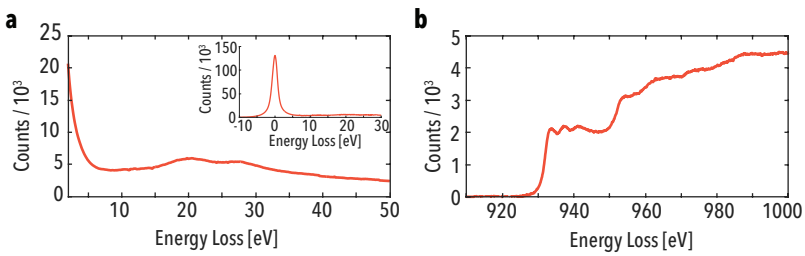

Figure 7.9: EEL spectra of Cu. *a) Cu low-loss spectrum with the surface and bulk plasmon resonance at around 20 and 30 eV loss, respectively. The zero-loss peak is included in the inset for reference. b) The Cu $L_{2,3}$ core-loss edge provides an example of the high-loss region. The spectra are from reference* [209].

In **Paper II**, we employ both the low-loss region of the EEL spectrum to quantify the LSPR shifts during the Cu nanoparticle oxidation, and the high-loss region of the Cu and O core-loss edges to characterize the chemical bonds in order to derive the oxidation state of the Cu atoms in the particle.

7.2.3 In situ TEM

By means of in situ TEM, structural and chemical changes in materials can be studied with high spatial resolution at elevated pressures, such as during a catalytic reaction. Therefore, in situ TEM can provide highly valuable information to the fields of heterogeneous catalysis, electrochemistry and material sciences, among others.[210] In situ TEM encompasses several concepts, including sample heating, imaging of reactions in the liquid or gas phase[210] and nanomechanical strength tests[211].

Here, I will mainly focus on the gas phase reaction aspect of in situ TEM, since it is of direct relevance for my thesis work, as we have used it in **Paper II**. To enable TEM studies at elevated gas pressures, there are two technical approaches; the environmental TEM (ETEM) and the closed-cell sample holder. In the ETEM, the column of the microscope is equipped with pressure-limiting apertures at the pole pieces surrounding the sample holder (7 mm apart[27]) to enable differential pumping and a higher pressure only in the volume surrounding the sample.[27] With this approach, it is possible to reach pressures up to a few millibar, above which the interaction between the beam and the gas molecules becomes too high to give any meaningful imaging.

The second approach, the closed-cell, is realized by sandwiching together two chips with electron transparent windows, which requires a specially designed sample holder.[212] In this way, the high pressure gases are contained within the sample holder and no modifications to the TEM are required. The closed-cell enables catalytic reactions to be studied at atmospheric pressures, which was first demonstrated by exposing a Cu/ZnO catalyst to 1.2 bar hydrogen[212]. Hence, this technique bridges the so-called pressure-gap in catalysis research. More recently, it also enables the study of reactions in liquids.[210] However, in the closed-cell approach, the image quality is not only reduced by the elevated pressure, but also the fact that the beam has to pass through two membranes, which decreases the resolution further. In both the closed-cell and ETEM setups, heating of the sample can be realized by a microelectromechanical system (MEMS)-type resistive heater on the backside of the sample.

With this fascinating development, the number of publications on in situ and operando TEM techniques has been increasing exponentially over the past ten years (evidenced by a search in Web of Science, > 10 000 publications in year 2020 compared to 3000 – 5000 per year between 2000 – 2010). We made use of the abilities of ETEM in **Paper II**, in order to investigate the oxidation process of single Cu nanoparticles. Using a combination of imaging and EELS, the ETEM investigation enabled us to generate mechanistic insights into the oxidation of nanoparticles at elevated pressures, from which we learned that multiple oxidation mechanisms can occur at different

stages of the oxidation process. To this end, only one in situ TEM study of the oxidation of Cu nanoparticles, conducted at an O_2 pressure of 2 Pa, has been reported previously.[115]

As the last point, I want to note that when conducting in situ TEM, as well as any other TEM studies, one has to be aware of potential beam damage to the specimen. In ordinary TEM, one may either experience beam effects by displacing atoms, so-called 'knock-on damage', or by radiolysis-type damage, in which chemical bonds in the sample are broken. When increasing the gas pressure around the specimen during imaging, a third type of beam effect may occur due to ionization of the gas molecules, which is increasing their reactivity.[27] Hence, when for instance studying catalytic reactions on nanoparticles using in situ TEM, extra care has to be taken to minimize or quantify the influence of the beam on the obtained results.

7.2.4 Scanning electron microscopy and transmission Kikuchi diffraction

Similar to STEM, scanning electron microscopy (SEM) operates by means of a focused electron beam raster-scanning the specimen surface. The main difference is that instead of transmitted, (back-)scattered electrons are detected. SEM operates at a lower acceleration voltage (usually up to 30 kV). Therefore, fewer and smaller lenses are can be used compared to TEM. SEM is useful to study surface and bulk specimens when resolution down to a few nanometers is required.[205]

As mentioned above, electrons from the probe can scatter backwards from interacting with atomic nuclei in the material - these are known as *backscattered electrons*. The amount of backscattering depends on the beam acceleration voltage and the atomic number(s) of the element(s) in the specimen. Thus, heavier atoms have a larger backscattering cross-section and a smaller penetration depth. The beam electrons can also interact inelastically with the specimen's electrons and result in secondary electrons as discussed above. The secondary electrons have a low kinetic energy, below 50 eV and typically peak at only a few eV.[213] Because of their low energy, the secondary electrons are useful to image the surface topography of the specimen, since they can only escape the material from a few nanometers below the surface due to their limited mean-free path in the sample material.[205]

Analogous to TEM, the backscattered electrons created in a SEM also experience diffraction from crystalline samples. In the diffraction pattern, there is a set of lines, known as Kikuchi lines, which hold information about the crystal lattice. Traditionally, the backscattered electrons from surfaces of bulk specimen were

detected by a technique that is known as electron backscatter diffraction (EBSD). More recently, EBSD has been developed to also operate in transmission mode to instead detect forward scattered electrons. This development, known as transmission Kikuchi diffraction (TKD), has enabled studies of nanocrystalline electron-transparent thin films with a spatial resolution down to 2 nm.[214] In recent years, the scope of TKD has been widened to also study the crystal grains in nanoparticles.[31] We exploit this new application of the TKD technique in **Paper III** to characterise the typical grain morphology in single Cu nanoparticles (**Fig. 7.10**). The TKD analysis both for the paper and for this figure was performed by Alice B. da Silva Fanta at the Technical University of Denmark, as part of our fruitful collaboration.

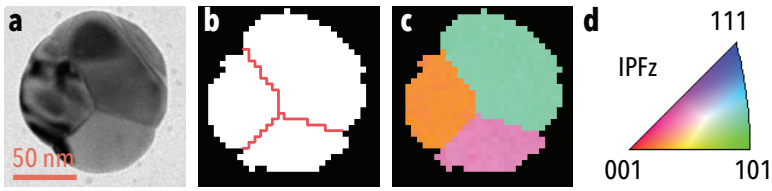

Figure 7.10: Crystal grain analysis of a Cu nanoparticle by TKD. *a) A single Cu nanoparticle imaged by TEM. b) The high-angle grain boundaries (red lines) and c) the crystallite orientation map of the same particle revealed by TKD. d) The inverse pole figure along the out-of-plane axis explaining the color-coding of the crystallite orientations in (c). Images are from the Supporting Information of Paper III.*

8 CORRELATIVE OPTICAL AND ELECTRON MICROSCOPY

In the previous Chapter, the general principles of microscopy, in particular dark-field scattering microscopy/spectroscopy and transmission electron microscopy, were introduced. In this Chapter, I will present the main steps of the correlative method I have developed based on these two techniques, and which I have applied in **Papers I, III and V**. The main steps of this experimental concept are the following; i) nanofabrication of a sample with a tailored array of single nanoparticles of choice (in my case Cu or Pd), ii) initial thermal annealing to achieve a distinct single nanoparticle grain morphology starting point, iii) TEM imaging of the particles to characterize the morphological starting point of each individual, iv) DFSS in situ experiment studying metal nanoparticle – gas interactions and v) post-experiment TEM imaging to assess structural changes and phase transitions that may have occurred.

Below, I will try to distinguish the importance of each step and also share some "tricks" that I have learnt along the way to be necessary for achieving a successful correlative DFSS and TEM experimental sequence. The fabrication of the sample will be excluded from this description. However, there are some features of the sample design that have implications for the experiment, hence, I will shortly mention them here as well. First of all, let us discuss the substrate used for the correlative experiments; a square electron transparent 25 nm thin SiN_x membrane with size 120 x 120 μm supported by a Si substrate. These TEM substrates were fabricated in-house[194] (thanks to Joachim Fritzsche) and cut in squares with a diagonal of 3 mm in order to fit in a standard TEM holder. The Cu particles were arranged in well defined regular arrays by means of electron-beam lithography. In the samples for the plasmonic scattering microscopy experiments in **Paper III and V**, an array of Au nanoparticles was also fabricated on the membrane to serve as an inert reference normalize for light intensity fluctuations during the measurement. Finally, since the SiN_x membranes are not only electron

transparent, but also transparent to optical photons, I placed a Si mirror underneath the chip in the reactor to avoid collecting light scattered from the sample holder.

8.1 THERMAL ANNEALING

As the first step after fabrication of the Cu nanoparticles, I annealed the sample in reducing environment (2 % H_2 mixed with Ar) at 400 °C. This was necessary for various reasons. i) In order to achieve a controlled grain morphology of the reduced nanoparticles. During evaporation of Cu onto the unheated substrate, the grown particles are highly polycrystalline with high defect concentration (**Fig. 8.1a**). ii) The samples were stored in air after fabrication. Hence, the annealing step provided a common reference point since it reduced the oxide formed, and samples that were at least up to a few months old seemed to acquire a grain morphology distribution equivalent to fresh ones after the annealing step. iii) Heating of the sample prior to TEM imaging reduced the carbon polymer deposition caused by the beam.[215] Since this carbon contamination can change the oxidation kinetics, as carbon coated Cu nanoparticles have been shown to be effectively protected from oxidation, it is important to minimize this effect.[216,217]

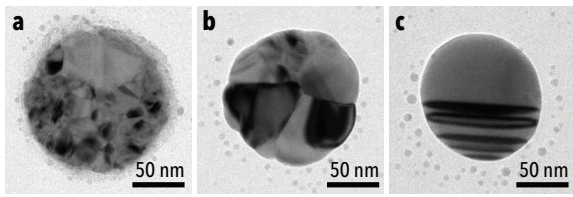

Figure 8.1: As-deposited and thermally annealed Cu nanoparticles. *a) A 120 nm Cu nanoparticle after lift-off, demonstrating the as-deposited grain morphology of ~ 30 small and one large grain. b) A polycrystal and c) a single crystal showing some diffraction contrast, possibly from strain or stacking faults. Both the particles in b) and c) are on the same sample and annealed simultaneously, still they exhibit different grain morphology.*

The annealing conditions used in **Paper I, III and V** varied between annealing for 1 h to 24 h at 400 °C in reducing environment achieved by mixing 2 or 4 % H_2 in Ar. Here, 2 % H_2 is enough and minimizes the heating of the reaction chamber and window due to the high thermal conductivity of hydrogen gas[218]. To be successful with the annealing step, it is crucial that the reactor is leak-tight, since only a few mbar O_2 partial pressure is enough to oxidize Cu nanoparticles at these high temperatures,[115] even in the presence of a reducing agent like H_2. For this reason, as well as to have the optical access of the microscope to monitor the annealing by means of the LSPR

scattering, I performed the annealing in the same reactor cell (Linkam THMS600) as the subsequent in situ experiments.

Concerning the annealing times, most of the recrystallization takes place already during the first hour of annealing.[47,48] Hence, already after two hours the grain morphology will not change significantly during further annealing (**Fig. 8.2**). It is rather the annealing temperature that should be increased to achieve further grain growth. To this end, I have found that annealing the evaporated Cu nanoparticles at 400 °C produces a relatively wide grain morphology distribution, exhibiting both a substantial fraction of single crystals and polycrystals with up to ~ 10 grains, depending on the particle size. Specifically, in experiments reported in **Paper III and V**, a wide grain boundary length distribution is desirable in order to study the dependence of the grain boundaries on the reaction under equivalent experimental conditions. To this end, the grain boundary density histogram depicted in **Fig. 8.2** was obtained by measuring the grain boundary length in pre-reaction TEM images and then normalizing it by the particle area measured from the same image.

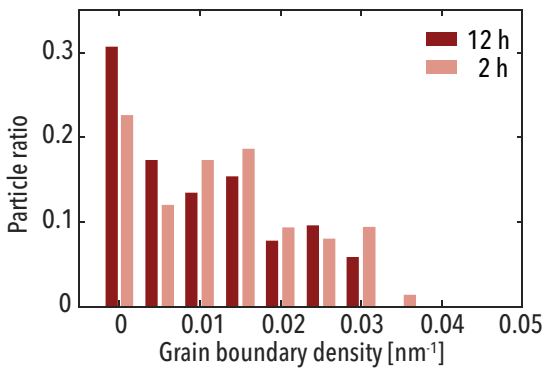

Figure 8.2: The grain boundary density distribution after annealing. *The grain boundary density is not substantially reduced by longer thermal annealing times after 2 hours, as seen for the corresponding grain boundary length distribution of 52 Cu nanoparticles thermally annealed for 12 hours (red) compared to 75 nanoparticles annealed for 2 hours (pink), both at 400 °C.*

8.2 PRE-REACTION TEM IMAGING

After the initial annealing step described in the previous Section, I took the sample immediately from the reactor cell, where it had been kept in the 2 % H_2 / 98 % Ar mixture to prevent oxidation and contamination by hydrocarbons, to insert it into the TEM. For the TEM imaging to establish the grain morphology starting point for the

correlative experiment, as described here, I used a FEI Tecnai T20 with LaB6 filament operated at 200 kV.

Even though the initial annealing step reduces the amount of carbon contamination on the particles, I experienced that the particles had slower oxidation kinetics if they had been imaged for longer times, say several minutes, compared to less than 30 s per particle, which was the typical time required for the pre-reaction morphology snapshots. I also noticed that the carbon contamination was more pronounced if the sample was not taken directly from the reducing environment of the thermal annealing, but had been kept in air for some hours or days. The carbon contamination was also the reason why the pre-reaction TEM imaging in the correlative-experiment sequence was done at low resolution, since acquiring high resolution images would have required longer focusing and acquisition times for each particle. After this quick initial "snapshot imaging", I usually did not observe any difference in the oxide shell growth at the next stage of the experimental sequence, and no slowing of the oxidation kinetics (**SI Paper III, Fig. S2.1**). However, in some cases I did observe a slight increase in the oxidation rate, which I think could be due to the increased ratio of charge-couples created by the electron beam, as we also note in **Paper II**.

Furthermore, during my early work I collected a single LSPR scattering spectrum of the particles after each step in the correlative-experiment sequence, since the LSPR peak position can be used as an indicator for changes in or around the nanoparticle. As a result of this, I could observe a small red-shift of the resonance peak after the initial TEM imaging step compared to before (**Fig. 8.3**). However, following the precautions described above, it did not seem to affect the following oxidation kinetics.

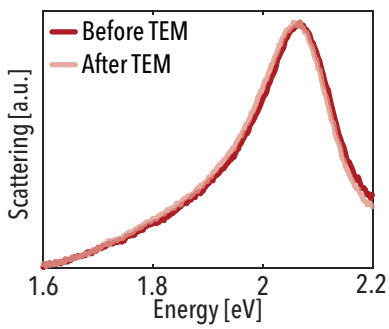

***Figure 8.3**: The scattering spectrum collected before and after the pre-reaction TEM imaging, where a slight red-shift of the resonance energy is observed.*

The observed red-shift probably was either due to a thin oxide shell growing in air during sample transport to or from the TEM, or due to minimal carbon deposition

during TEM imaging. However, during the snapshot imaging neither an oxide shell nor any carbon could be resolved. If there was any oxide, it was likely reduced while heating in reducing environment before the oxidation experiment. To this end, there are two reports of TEM-induced red-shifts (significantly larger than in **Fig. 8.3**)[219,220] observed in LSPR-TEM correlative studies. In one of the studies[219], the authors suggested that the reason for the observed red-shift was oxidation of the hollow Au-Ag particles during TEM imaging.

8.3 DFSS IN SITU EXPERIMENTS

The in situ DFSS and imaging experiments were carried out in a reaction chamber (Linkam THMS600) mounted on the stage of the upright microscope (Nikon Eclipse LV 150 N) equipped with a dark-field condenser (Nikon TU plan ELWD 50x). The reactor chamber was adapted with Swagelok gas connections through which the gas mixture was supplied by mass flow controllers (Bronkhorst, low-ΔP-flow). For oxidation experiments on Cu, it was crucial to not have any oxygen or water vapor in the gas flow. Hence, the carrier gas (Ar) was passed through a moisture and an oxygen filter. Furthermore, to enable thermal annealing and reaction conditions at elevated temperatures without substantial heating of the reactor itself, and subsequently the microscope objective, the built-in water cooling of the reactor was used.

For spectroscopic experiments, the light collected through the DF condenser was dispersed on the grating of the spectrometer (Andor SR193i) and collected by a CCD camera (Andor Newton 920) with 256 x 1024 pixels. A motorized stage (Prior Proscan) ensured that the microscope stage was stable during the experiment. However, the largest drift I observed was due to heat accumulation in the optical path during extended measurements. Hence, it was crucial to let the 50 W halogen lamp be turned on for at least 1 h before the experiment to enable the system to reach thermal equilibrium.

The Cu nanoparticles were fabricated by EBL in a pattern design that enabled easy recognition of the same particles in both TEM and DFSS analysis. The sample design varied depending on if the purpose was to conduct a spectroscopic analysis or an imaging experiment collecting only the intensity of the scattered light to enable multiplexing of more particles. For the spectroscopic experiment, the Cu particles were arranged in columns separated by 10 μm with 7 μm in between each row of particles, as visualized by an optical dark-field micrograph of a typical sample in **Fig. 8.4a**. This leaves enough space to acquire the background scattering in between the particles, as explained in the previous chapter. By this approach, the spectrum from ~ 15 particles could be analyzed during an in situ experiment.

The second approach that I applied, was the plasmonic nanoimaging where the light scattered from the particles was not dispersed onto the grating of the spectrometer but instead directly imaged with the CCD. With the current design, **Fig. 8.4b** displays one frame collected by the CCD, containing 225 Cu particles and 30 Au particles that can be probed simultaneously and used as optical reference. For a single image, the particle number is limited by a compromise between the size of the TEM membrane, the magnification of the microscope optical path and the size of the CCD chip. The Au nanoparticles are placed above and below the Cu nanoparticles on the CD, to help to normalize for light fluctuations and the upwards readout-smearing of the CCD chip.

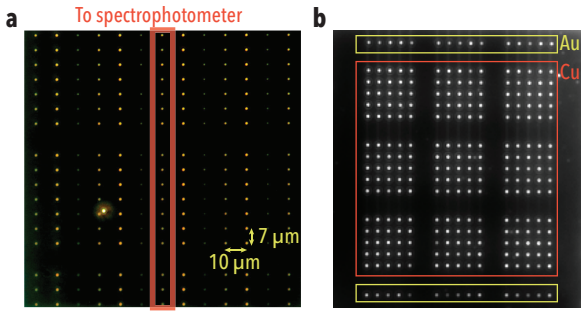

Figure 8.4: Sample designs for spectroscopy and imaging. *a) A dark-field scattering micrograph depicting the sample design applied in spectroscopic experiments, in which the light collected by the spectrometer through the opening slit stems from one column only, oriented parallel to the slit. b) An example of the sample design employed in the plasmon nanoimaging experiments with Au nanoparticles in the top and bottom of the array, were they serve as inert references used to account for light intensity fluctuations during an experiment.*

Typical integration times per frame were 10 s for spectroscopy and 0.25 s with 15 or 30 accumulations for the nanoimaging approach. This was enough to observe the chemical transitions on the particles that I studied. In order to improve the temporal resolution, one could for example use a faster camera with higher sensitivity. Furthermore, a dynamic narrow-band wavelength filter could be applied for faster spectroscopic analysis, however, with some loss of spectral resolution.[199,202]

8.4 POST-REACTION TEM ANALYSIS

After the in situ DFSS experiment, I again imaged the particles in the TEM to observe structural and chemical phase transitions that may have occurred as a result of the exposure to the reaction conditions, either during Cu nanoparticle oxidation or

during the CO oxidation reaction. For this step, I either used a Tecnai T20 to be able to quickly screen a large group of particles and obtain a large data set of structural changes (typically 50 - 100 particles per sample), or a FEI Titan 80-300 operated at 300 kV, to acquire STEM images with higher resolution and larger phase contrast, as well as to enable elemental mapping with high spatial resolution.

9 SUMMARY

By reading my thesis, I hope you are convinced that combining DFSS and TEM can improve our understanding of the interactions between individual nanoparticles and gas molecules. I have applied the correlative method in a couple of proof-of-concept studies, in an effort to shed light on Cu nanoparticle oxidation in pure O_2, as well as under catalytic CO oxidation reaction conditions. We have also applied the combined strength of TEM and plasmonic nanoimaging to reveal that the grain growth in Pd nanoparticles during hydrogen sorption cycling leads to slower hydrogen sorption kinetics.

I started out by developing the concept of the correlative method in **Paper I,** by studying the oxidation of individual single crystalline Cu nanoparticles. By the combination of the in situ DFSS experiment and the pre- and post-oxidation TEM imaging, we could corroborate that the LSPR mode-splitting observed was due to the enormous structural transformation the particles are going through during oxidation. To this end, the red-shift of the LSPR during the initial oxide layer growth had previously been studied in ensemble-type LSPR experiments[110,113]. However, in these experiments, the LSPR mode splitting upon Kirkendall void formation could not be resolved, as a consequence of the ensemble averaging effect. Therefore, when I first observed this unanticipated spectral feature it was surprising. However, with the help of thorough FDTD electrodynamic simulations I could conclude that the simple, yet beautiful, explanation for the occurrence of the mode splitting was the asymmetry introduced in the metallic Cu core by the Kirkendall void growth.

To further corroborate the mechanisms of oxidation, and investigate how they are reflected in the LSPR signature of single Cu nanoparticles, I studied the complete oxidation process by ETEM in collaboration with Shima Kadkhodazadeh and Monia Runge Nielsen at the Technical University of Denmark. This approach allowed us to track the evolution of the LSPR by EELS, while intermittently imaging the structural

transformations. This is reported in **Paper II**, where we map the entire oxidation process at temperatures between 50 – 200 °C. In this way, we were able to generate a holistic picture of the process and unravel that several nanoparticle oxidation mechanisms, which previously only had been observed independently, actually can occur simultaneously in a single nanoparticle. The observed competing mechanism were, oxide island nucleation and growth, the Cabrera-Mott mechanism (CM)[80], the Valensi-Carter mechanism (VC)[95] and the nanoscale Kirkendall effect (NKE)[99,103]. Specifically, at 50 °C, we observed oxide nucleation and self-limiting oxide shell growth to a thickness of about 5 nm, driven by the static electric field over the oxide, as suggested in the CM model. At higher temperatures, apart from the outward growing shell, we also observed temperature-activated inward oxide shell growth, which lead to two separate oxide shells spaced by a gap. The inward growing shell was in line with the VC mechanism. Finally, for all particles after about 20 – 30 % of the initial Cu volume was oxidized, we started to observe the nucleation of Kirkendall voids. In particles with radius < 40 nm, we only observed one void, expanding in such a way that interface energy associated with the metal-oxide interface was minimized. In larger particles, multiple voids formed simultaneously and expanded independently until they merged. I also modelled the observed structural evolution of the particles during oxidation by FDTD and was able to accurately reproduce the corresponding LSPR signatures obtained experimentally by EELS, thereby establishing that the LSPR signatures indeed originated directly from the observed structural transformation in the nanoparticles.

From these first two studies, I saw indications for particle-specific factors influencing the oxidation process, specifically in particles with more complex morphologies than the single crystals reported in **Paper I**. Therefore, I wanted to further investigate potential relations between the oxidation process and the grain morphology of the particles, as reported in **Paper III**. Interestingly, by monitoring the particles in situ during oxidation by STEM in **Paper II**, we observed that the Kirkendall voids actually expanded across grain boundaries almost without taking any notice of them. Therefore, I hypothesized that the grain boundaries instead could play a larger role in the early stages of oxidation, since grain boundaries are known to enhance diffusion rates.[65] Surprisingly, also this enhancement effect was absent in the intermediate temperature regime studied in **Paper III** (150 °C, 1 % O_2). In fact, the oxide shell was growing at the same rate on all particles, independent of grain boundary length. Intrigued by this finding at first, by resorting to density functional theory (DFT) calculations with the help of Alvaro Posada Borón, I could eventually conclude that the diffusion of Cu atoms or vacancies was not the rate limiting step of the process at

the present conditions but that it was the extraction of the Cu atoms from the lattice at the metal – oxide interface, which eliminated the impact of grain boundary diffusion.

One of the reasons that motivated us to work on generating better understanding of the oxidation process of (Cu) metal nanoparticles, is the importance of mapping and monitoring catalyst deactivation conditions in order to design strategies to avoid such deactivation during catalyst operation.[15] With this in mind, I take the step in summarizing my thesis work to applying the single particle plasmonic nanoimaging concept to operando/in situ catalyst monitoring in **Paper IV and V,** by focusing on CO oxidation over Cu catalysts as the model reaction. In the first study together with David Albinsson, we corroborated the CO oxidation reaction over Cu model catalysts in nanochannels, by probing in situ the Cu catalyst oxidation with the plasmonic nanoimaging approach. From the plasmonic readout, we concluded that the Cu catalyst oxidation was leading to decreased activity for the CO oxidation reaction. Furthermore, we observed particle-specific oxidation rates, and hypothesized that they were a consequence of different grain morphologies present in the lithographically fabricated particles. Unfortunately, since the nanofluidic reactors are not transparent to electrons, this hypothesis could not be verified in this work directly.

Nevertheless, this indication of particle-specific oxidation rates in **Paper IV** led me to study the potential impact of grain boundaries on Cu catalyst oxidation under CO oxidation reaction conditions in **Paper V**. However, instead of using the nanofluidic reactor platform, I utilized TEM-compatible substrates and a macroscopic reactor to be able to image the particles both before and after the CO oxidation reaction by applying the correlative plasmonic nanoimaging and TEM approach described in Chapter 8. As a main result, employing similar reaction conditions as in **Paper IV**, I studied the oxidation of the Cu nanoparticles at orders of magnitude lower O_2 partial pressure than in our previous studies (**Paper I-III**). Thereby, we entered another oxidation regime that is seemingly similar to that previously reported in a low O_2 pressure in situ STEM study.[115] At these conditions, we found that the oxide first nucleated only at a couple of sites, from where it grew into the Cu lattice. Consequently, the result was not a homogeneously thick oxide shell, but rather a few oxide fronts, which sometimes resembled “cake-pieces”, that grew into the particles. Interestingly, the nucleation sites for the oxide at these conditions were predominantly the intersections of grain boundaries with the particle surface, likely due to their more open structures, with a higher density of steps and defects, and consequently different energetics.

Finally, together with Svetlana Alekseeva, I applied the correlated TEM - plasmonic nanoimaging concept also to a different process than Cu oxidation, namely hydrogen sorption in Pd nanoparticles in **Paper VI**. In this work, we study the impact of grain

structure on hydrogen sorption kinetics and could connect the observed decreased rate of hydrogen sorption upon cyclic exposure of the sample to hydrogen with significant grain growth in the Pd nanoparticles. The hydrogen induced grain growth was observed with TEM imaging and X-ray diffraction of particles after hydrogen sorption cycling. Thereby, we were able to offer an explanation for the previously "mysterious" observation of sorption rate decrease with hydrogen cycling. In doing so, this study also sets a beautiful example for how increasing the size of a single particle data set can unravel intricate trends, where previously it was believed that no trends existed, and how it thereby can be used to identify physical reasons for kinetic compensation effects, which often are regarded as statistical artefacts .

9.1 OUTLOOK

To further scrutinize nanoparticle oxidation mechanisms, with Cu as the model system, I think the natural next step after studying vacancy accumulation in the grain boundaries would be to map the most probable sites for void formation. As the natural extension of the grain boundary vacancy accumulation, the Kirkendall voids are likely to nucleate at the grain boundary – oxide intersection. Moreover, strain-enhanced diffusion is suggested to be a factor influencing the oxidation mechanism in iron nanoparticles.[221] The mass transport of metal ions from the metal to the oxide is likely to result in tensile strain in the metal lattice and compressive strain in the oxide. Hence, a second interesting aspect about the void formation mechanism could potentially be to investigate how the void nucleation site is affected by lattice strain in the nanoparticles. Specifically, this could be inquired by comparing colloidal and lithographical particles, where the latter will likely have more lattice strain since they are grown on a substrate. This could potentially be an interesting in situ TEM experiment, i.e., to first map the strain in a Cu nanoparticle[222] and subsequently oxidize it while imaging to observe where the void is formed in correlation to the previously obtained strain map.

In the bigger picture, concerning how oxidation of Cu nanoparticles can be representative also for oxidation of other metal nanoparticles, comparing to Ni would be interesting, since it does also form a Kirkendall void upon oxidation. Nonetheless, the Ni oxide shell is not of homogeneous thickness but tends to grow asymmetrically. One likely reason is that there is a difference in the self-diffusion to metal-in-oxide-diffusion ratios, where the ratio is larger in Cu compared to Ni.[102] Furthermore, the grain boundary excess volume is larger in Cu compared to Ni, because of the difference in strain resistance in the bonds,[42] which also could influence the void nucleation. The oxidation of Ni is also interesting in itself and not only as a

benchmark, because Ni is suggested as a complement for the hydrogenation of CO_2 to methane.[223]

In the context of catalysis, we have not fully understood the preference for the oxide nucleation at the grain boundary – surface intersection during CO oxidation on Cu model catalysts at low O_2 pressure. Are the grain boundary sites more prone to oxidation or is the CO oxidation reaction more active at other surface sites and removes oxygen from the surface oxide? Joint efforts using DFT computations and correlative in situ plasmonic nanospectroscopy with STEM could potentially provide a way to shed some light onto this "what came first: the chicken or the egg?"-dilemma. A second interesting aspect to study of the CO oxidation, which is also relevant to other reactions under oxidizing environments, is how surface sensitive our plasmonic nanospectroscopy readout is to the formation of surface oxides. In low O_2 partial pressure, the oxidation is slow and it could be possible to probe very thin surface oxides. In **Paper III**, I observe about 20 % increase in scattering for a 5 nm thick oxide on 85 nm nanoparticles, it would perhaps be possible to probe even down to single oxide layers.

Furthermore, by means of in situ TEM, it would be possible to also study smaller Cu nanoparticles closer to industrially relevant sizes of a few nanometers. To correlate the results, it would be interesting to also enable the study of such small particles by plasmonic nanospectroscopy. An inert plasmonic antenna particle can be placed next to the catalyst particle of interest.[177,178] This indirect sensing approach could then likely by applied in the correlative measurement approach to study catalytically more relevant particles.

As a final aspect, I would like to note that I have applied the correlative method only for studying CO oxidation, and in a model reaction fashion. A next step could therefore be to apply the method I have developed to other industrially relevant reactions over Cu catalysts, such as the water gas shift reaction[127] or methanol synthesis[128,130]. Another suitable catalyst (model) system to investigate, thanks to the large optical scattering cross-section of its nanoparticles, is Ag, widely used for ethylene epoxidation.[224]

In summary, I am convinced that the concept of combining the strength of electron microscopy characterization with the non-invasive in situ plasmonic nanospectroscopy method for probing catalyst state under reaction conditions can be tuned and adapted to probe a wide range of structure – function relations. Not only within the catalysis fields, but possibly also for sensing applications, such as demonstrated here for Pd-based hydrogen sensing, or to study corrosion relevant in microelectronics, or the interaction between metal nanoparticles and biomolecules in the field of nanosafety.

10 ACKNOWLEDGEMENTS

First of all I would like to acknowledge the financial support to the project that I have been part of during my doctorate thesis studies, the Knut and Alice Wallenberg Foundation project 2015.0055 and the financial support to the MC2 cleanroom by the Knut and Alice Wallenberg foundation.

There are so many people that I would like to thank for supporting me during these years to reach this goal of writing my thesis, I cannot name everyone here, but to those that I have worked with throughout these nearly five years; I am grateful to all of you! With that said, there are a few people that deserve some extra acknowledgement.

Most of all, thanks to my supervisor Christoph, for giving me this opportunity and always believing that I can achieve this, for all the positive words and great ideas, and most of all believing anything is possible. I am truly grateful for your constant support and guidance during these years.

Thanks to my examiner Henrik Grönbeck, for providing feedback on this thesis and caring for our joint work-place and making us a thrive there.

Thanks also to my co-supervisors, Fredrik Westerlund and Anders Hellman.

I want to thank the MC2 cleanroom and the CMAL personnel. A special big thanks to Stefan Gustafsson and Ludvig de Knoop, for sharing your TEM expertise and for your never-ending willingness to help.

Thanks to all past and present members of Chemical Physics, for being such great colleges and for all the fun and interesting conversations in the lunch room. In particular, to the people in the Langhammer group for being such a fun and inspirational group to be a part of.

A special thanks to Joachim and David for providing me with infallible e-beam samples. Thanks to David and Christopher the time you spent in reading this thesis, to

all the discussions and great ideas, and for sharing all the fun and interesting conference experiences. ☺

Thanks to all co-authors; to Tomasz for the FDTD support, to Alvaro and Henrik for the collaboration on the Cu oxidation mechanism, and a special thanks to Shima, Alice, Monia and Jakob at DTU. I have enjoyed our collaborations so much! I have learnt a lot, and it has really enriched by PhD time. Thank you!

As customary last, but definitely not least, thanks to my friends, for your support, and all the fun times we share. To my family, for always supporting and believing in me. And to Erik, for your support, for giving me perspective, for all our fun adventures, big and small, and for just making life utterly enjoyable! You are everything to me.

REFERENCES

1. Maslin, M. *Global Warming : A Very Short Introduction*. (Oxford Univeristy Press, 2004).
2. Ian Sample. The father of climate change | Environment | The Guardian. Available at: https://www.theguardian.com/environment/2005/jun/30/climatechange.climatechangeenvironment2. (Accessed: 25th February 2021)
3. Lenton, T. M. *et al.* Climate tipping points — too risky to bet against. *Nature* ***575***, 592–595 (2019).
4. Randers, J. & Goluke, U. An earth system model shows self-sustained melting of permafrost even if all man-made GHG emissions stop in 2020. *Sci. Rep.* **10**, 18456 (2020).
5. US Department of Commerce, N. G. M. L. Global Monitoring Laboratory - Carbon Cycle Greenhouse Gases.
6. The Paris Agreement | UNFCCC. Available at: https://unfccc.int/process-and-meetings/the-paris-agreement/the-paris-agreement. (Accessed: 26th April 2021)
7. IEA - Data & Statistics: CO2 emissions. Available at: https://www.iea.org/data-and-statistics?country=WORLD&fuel=CO2emissions&indicator=CO2BySector. (Accessed: 23rd February 2021)
8. Álvarez, A. *et al.* Challenges in the Greener Production of Formates/Formic Acid, Methanol, and DME by Heterogeneously Catalyzed CO2 Hydrogenation Processes. *Chemical Reviews* **117**, 9804–9838 (2017).
9. The European Green Deal: hydrogen is a priority area for a clean and circular economy | www.fch.europa.eu. Available at: https://www.fch.europa.eu/news/european-green-deal-hydrogen-priority-area-clean-and-circular-economy. (Accessed: 23rd February 2021)
10. Q&A: A Hydrogen Strategy. Available at: https://ec.europa.eu/commission/presscorner/detail/en/QANDA_20_1257. (Accessed: 23rd February 2021)
11. Darmadi, I., Nugroho, F. A. A. & Langhammer, C. High-Performance Nanostructured Palladium-Based Hydrogen Sensors - Current Limitations and Strategies for Their Mitigation. *ACS Sensors* **5**, 3306–3327 (2020).
12. Hübert, T., Boon-Brett, L., Black, G. & Banach, U. Hydrogen sensors - A review. *Sensors and Actuators, B: Chemical* **157**, 329–352 (2011).

13. Laudenschleger, D., Ruland, H. & Muhler, M. Identifying the nature of the active sites in methanol synthesis over Cu/ZnO/Al2O3 catalysts. *Nat. Commun.* **11**, 3898 (2020).

14. Ruano, D. *et al.* Dynamic Structure and Subsurface Oxygen Formation of a Working Copper Catalyst under Methanol Steam Reforming Conditions: An in Situ Time-Resolved Spectroscopic Study. *ACS Catal.* **9**, 2922–2930 (2019).

15. Hartman, T., Geitenbeek, R. G., Wondergem, C. S., Van Der Stam, W. & Weckhuysen, B. M. Operando Nanoscale Sensors in Catalysis: All Eyes on Catalyst Particles. *ACS Nano* (2020).

16. *Operando Research in Heterogeneous Catalysis*. **114**, (Springer International Publishing, 2017).

17. Esposito, D. Mind the gap. *Nature Catalysis* **1**, 807–808 (2018).

18. Dou, J. *et al.* Operando chemistry of catalyst surfaces during catalysis. *Chem. Soc. Rev.* **46**, 2001–2027 (2017).

19. Sambur, J. B. & Chen, P. Approaches to single-nanoparticle catalysis. *Annu. Rev. Phys. Chem.* **65**, 395–422 (2014).

20. Alayoglu, S. *et al.* In situ surface and reaction probe studies with model nanoparticle catalysts. *ACS Catal.* **2**, 2250–2258 (2012).

21. Weckhuysen, B. M. Snapshots of a working catalyst: Possibilities and limitations of in situ spectroscopy in the field of heterogeneous catalysis. *Chem. Commun.* **2**, 97–110 (2002).

22. Bañares, M. A., Guerrero-Pérez, M. O., Fierro, J. L. G. & Cortez, G. G. Raman spectroscopy during catalytic operations with on-line activity measurement (operando spectroscopy): A method for understanding the active centres of cations supported on porous materials. *J. Mater. Chem.* **12**, 3337–3342 (2002).

23. Park, J. Y. & Somorjai, G. A. Bridging materials and pressure gaps in surface science and heterogeneous catalysis. in *Current Trends of Surface Science and Catalysis* 3–17 (Springer New York, 2014).

24. Wang, W. Imaging the chemical activity of single nanoparticles with optical microscopy. *Chem. Soc. Rev.* **47**, 2485–2508 (2018).

25. Erdamar, A. K., Malladi, S., Tichelaar, F. D. & Zandbergen, H. W. Closed Cell Systems for In Situ TEM with Gas Environments Ranging from 0.1 to 5 Bar. in *Controlled Atmosphere Transmission Electron Microscopy* 165–210 (Springer International Publishing, 2016).

26. Niu, Y. & Zhang, B. In situ investigation of nanocatalysts in gas atmosphere by transmission electron microscopy. *Current Opinion in Green and Sustainable Chemistry* **22**, 22–28 (2020).

27. Wagner, J. B., Cavalca, F., Damsgaard, C. D., Duchstein, L. D. L. & Hansen, T. W. Exploring the environmental transmission electron microscope. *Micron* **43**, 1169–1175 (2012).

28. Schlögl, R. Heterogeneous catalysis. *Angewandte Chemie - International Edition* **54**, 3465–3520 (2015).

29. Van Loon, J., Kubarev, A. V. & Roeffaers, M. B. J. Correlating Catalyst Structure and Activity at the Nanoscale. *ChemNanoMat* **4**, 6–14 (2018).

30. Zhong, J. H. *et al.* Probing the electronic and catalytic properties of a bimetallic surface with 3nm resolution. *Nat. Nanotechnol.* **12**, 132–136 (2017).

31. Alekseeva, S. *et al.* Grain boundary mediated hydriding phase transformations in individual polycrystalline metal nanoparticles. *Nat. Commun.* **8**, 1084 (2017).

32. Albinsson, D. *et al.* Operando detection of single nanoparticle activity dynamics inside a model pore catalyst material. *Sci. Adv.* **6**, 7678–7697 (2020).

33. Kittel, C. *Introduction to Solid State Physics*. (John Wiley & Sons, Ltd, 2005).

34. Hofmann & Philip. *Solid State Physics: An Introduction*. (John Wiley and Sons Inc., 2015).

35. Chorkendorff, I. & Niemantsverdriet, J. W. *Concepts of Modern Catalysis and Kinetics*. (Wiley-VCH Verlag GmbH & Co. KGaA, 2013).

36. Kim, T. H. *et al.* Structural dependence of grain boundary resistivity in copper nanowires. in *Japanese Journal of Applied Physics* **50**, (2011).

37. Suryanarayana, C. Nanocrystalline materials. *Int. Mater. Rev.* **40**, 41–63 (1995).

38. Yip, S. The strongest size. *Nature* **391**, 532–533 (1998).

39. Wolf, D. Correlation Between Structure, Energy, and Ideal Cleavage Fracture for Symmetrical Grain Boundaries in Fcc Metals. *J. Mater. Res.* **5**, 1708–1730 (1990).

40. Bulatov, V. V., Reed, B. W. & Kumar, M. Grain boundary energy function for fcc metals. *Acta Mater.* **65**, 161–175 (2014).

41. Brandon, D. 25 Year Perspective Defining grain boundaries: An historical perspective the development and limitations of coincident site lattice models. *Materials Science and Technology* **26**, 762–773 (2010).

42. Bean, J. J. & McKenna, K. P. Origin of differences in the excess volume of copper and nickel grain boundaries. *Acta Mater.* **110**, 246–257 (2016).

43. Brandon, D. . The structure of high-angle grain boundaries. *Acta Metall.* **14**, 1479–1484 (1966).

44. Randle, V. The coincidence site lattice and the 'sigma enigma'. *Mater. Charact.* **47**, 411–416 (2001).

45. Mishin, Y., Asta, M. & Li, J. Atomistic modeling of interfaces and their impact on microstructure and properties. *Acta Mater.* **58**, 1117–1151 (2010).

46. Raabe, D. Recovery and Recrystallization: Phenomena, Physics, Models, Simulation. in *Physical Metallurgy: Fifth Edition* **1**, 2291–2397 (Elsevier Inc., 2014).

47. Simões, S., Calinas, R., Vieira, M. T., Vieira, M. F. & Ferreira, P. J. *In situ* TEM study of grain growth in nanocrystalline copper thin films. *Nanotechnology* **21**, 145701 (2010).

48. Berg, J. *Post-Fabrication Engineering of Metal Nanoparticle Grain Structure and Faceting: For improving the fabrication of plasmonic nanoparticles for sensing and catalysis*. (2019).

49. Ames, M. *et al.* Unraveling the nature of room temperature grain growth in nanocrystalline materials. *Acta Mater.* **56**, 4255–4266 (2008).

50. Hillert, M. On the theory of normal and abnormal grain growth. *Acta Metall.* **13**, 227–238 (1965).

51. Farkas, D., Bringa, E. & Caro, A. Annealing twins in nanocrystalline fcc metals: A molecular dynamics simulation. *Phys. Rev. B - Condens. Matter Mater. Phys.* **75**, 184111 (2007).

52. Oh, S. J., Cook, D. C. & Townsend, H. E. Characterization of iron oxides commonly formed as corrosion products on steel. *Hyperfine Interact.* **112**, 59–66 (1998).

53. FitzGerald, K. P., Nairn, J., Skennerton, G. & Atrens, A. Atmospheric corrosion of copper and the colour, structure and composition of natural patinas on copper. *Corros. Sci.* **48**, 2480–2509 (2006).

54. Tuck, C. D. S., Powell, C. A. & Nuttall, J. 3.07 - Corrosion of Copper and its Alloys. *Shreir's Corros.* **3**, 1937–1973 (2010).

55. Kasap, S., Koughia, C. & Ruda, H. E. Electrical Conduction in Metals and Semiconductors. in *Springer Handbook of Electronic and Photonic Materials* (Springer International Publishing, 2017).

56. Jernigan, G. G. & Somorjai, G. A. Carbon Monoxide Oxidation over Three Different Oxidation States of Copper: Metallic Copper, Copper (I) Oxide, and Copper (II) Oxide - A Surface Science and Kinetic Study. *J. Catal.* **147**, *567–577* (1994).

57. Adams, B. D. & Chen, A. The role of palladium in a hydrogen economy. *Materials Today* **14**, 282–289 (2011).

58. Schneemann, A. *et al.* Nanostructured Metal Hydrides for Hydrogen Storage. *Chemical Reviews* **118**, 10775–10839 (2018).

59. Ross, J. *Heterogeneous catalysis: fundamentals and applications*. (Elsevier, 2012).

60. Lide, D. R. Bond Strengths in Diatomic Molecules. in *CRC Handbook of Chemistry and Physics* (CRC Press, Boca Raton, FL, 2005).

61. Zhu, Q., Zou, L., Zhou, G., Saidi, W. A. & Yang, J. C. Early and transient stages of Cu oxidation: Atomistic insights from theoretical simulations and in situ experiments. *Surf. Sci.* **652**, 98–113 (2016).

62. Wang, J., Chen, H., Hu, Z., Yao, M. & Li, Y. A Review on the Pd-Based Three-Way Catalyst. *Catal. Rev.* **57**, 79–144 (2015).

63. Chee, S. W., Arce-Ramos, J. M., Li, W., Genest, A. & Mirsaidov, U. Structural changes in noble metal nanoparticles during CO oxidation and their impact on catalyst activity. *Nat. Commun.* **11**, 1–9 (2020).

64. Gattinoni, C. & Michaelides, A. Atomistic details of oxide surfaces and surface oxidation: the example of copper and its oxides. *Surf. Sci. Rep.* **70**, 424–447 (2015).

65. Horváth, J., Birringer, R. & Gleiter, H. Diffusion in nanocrystalline material. *Solid State Commun.* **62**, 319–322 (1987).

66. Hauffe, K. *Oxidation of Metals*. (Springer US, 1995).

67. Paul, A., Laurila, T., Vuorinen, V. & Divinski, S. V. *Thermodynamics, diffusion and the kirkendall effect in solids*. *Thermodynamics, Diffusion and the Kirkendall Effect in Solids* (Springer International Publishing, 2014). doi:10.1007/978-3-319-07461-0

68. Shewmon, P. *Diffusion in Solids*. (Springer International Publishing, 2016).

69. Maier, K. Self-diffusion in copper at "low" temperatures. *Phys. Status Solidi* **44**, *567–576* (1977).

70. Suzuki, A. & Mishin, Y. Atomistic Modeling of Point Defects and Diffusion in Copper Grain Boundaries. *Interface Sci.* **11**, 131–148 (2003).

71. Sørensen, M. R. & Mishin, Y. Diffusion mechanisms in Cu grain boundaries. *Phys. Rev. B - Condens. Matter Mater. Phys.* **62**, 3658–3673 (2000).

72. Herzig, C. & Mishin, Y. Grain boundary diffusion in metals. in *Diffusion in Condensed Matter: Methods, Materials, Models* 337–366 (Springer Berlin Heidelberg, 2005).

73. Nakajima, H. The discovery and acceptance of the Kirkendall effect: The result of a short research career. *JOM* **49**, 15–19 (1997).

74. Smigelskas, A. D. & Kirkendall, E. O. Zinc diffusion in alpha brass. *Trans. AIME* **171**, (1947).

75. Meyer, B. K. *et al.* Binary copper oxide semiconductors: From materials towards devices. *Phys. Status Solidi Basic Res.* **249**, 1487–1509 (2012).

76. Zhu, Y., Mimura, K., Lim, J. W., Isshiki, M. & Jiang, Q. Brief review of oxidation kinetics of copper at 350 °C to 1050 °C. *Metallurgical and Materials Transactions A: Physical Metallurgy and Materials Science* **37**, 1231–1237 (2006).

77. Samal, S. & Mitra, S. K. Influence of Grain Shape, Size, and Grain Boundary Diffusion on High-Temperature Oxidation of Pure Metal Fe, Cu, and Zn. *Metall. Mater. Trans. A Phys. Metall. Mater. Sci.* **46**, 3324–3332 (2015).

78. Gulbransen, E. A., Copan, T. P. & Andrew, K. F. Oxidation of Copper between 250° and 450°C and the Growth of CuO "Whiskers". *J. Electrochem. Soc.* **108**, 119 (1961).

79. Xu, Z., Rosso, K. M. & Bruemmer, S. Metal oxidation kinetics and the transition from thin to thick films. *Phys. Chem. Chem. Phys.* **14**, 14534–14539 (2012).

80. Cabrera, N. & Mott, N. F. Theory of the Oxidation of Metals. *Rep. Prog. Phys.* **12**, (1949).

81. Fujita, K., Ando, D., Uchikoshi, M., Mimura, K. & Isshiki, M. New model for low-temperature oxidation of copper single crystal. *Appl. Surf. Sci.* **276**, 347–358 (2013).

82. Yang, J. C., Yeadon, M., Kolasa, B. & Gibson, J. M. Oxygen surface diffusion in three-dimensional Cu2O growth on Cu(001) thin films. *Appl. Phys. Lett.* **70**, 3522–3524 (1997).

83. Fanfoni, M. & Tomellini, M. The Johnson-Mehl-Avrami-Kolmogorov model: A brief review. *Nuovo Cim. della Soc. Ital. di Fis. D - Condens. Matter, At. Mol. Chem. Physics, Biophys.* **20**, 1171–1182 (1998).

84. Yang, J. C., Evan, D. & Tropia, L. From nucleation to coalescence of Cu2O islands during in situ oxidation of Cu(001). *Appl. Phys. Lett.* **81**, 241–243 (2002).

85. Khayati, G. R., Nourafkan, E., Karimi, G. & Moradgholi, J. Synthesis of cuprous oxide nanoparticles by mechanochemical oxidation of copper in high planetary energy ball mill. *Adv. Powder Technol.* **24**, 301–305 (2013).

86. Yang, J. C., Kolasa, B., Gibson, J. M. & Yeadon, M. Self-limiting oxidation of copper. *Appl. Phys. Lett.* **73**, 2841–2843 (1998).

87. Han, Z. *et al.* Comparison of the oxidation behavior of nanocrystalline and coarse-grain copper. *Oxid. Met.* **63**, 261–275 (2005).

88. Maack, B. & Nilius, N. Impact of Granularity on the Oxidation Kinetics of Copper. *Phys. status solidi* **257**, 1900778 (2020).

89. Zhou, G., Wang, L. & Yang, J. C. Effects of surface topology on the formation of oxide islands on Cu surfaces. *J. Appl. Phys.* **97**, 063509 (2005).

90. Zhang, X. Y. Understanding the corrosion resistance of nanocrystalline materials: the influence of grain size. in *Corrosion Protection and Control Using Nanomaterials* 34–58 (Elsevier, 2012).

91. Niu, Y. *et al.* The air oxidation of a nanocrystalline Cu-10 wt%Ni alloy at 800°C. *Corros. Sci.* **42**, 1763–1777 (2000).

92. Zhdanov, V. P. & Kasemo, B. Cabrera–Mott kinetics of oxidation of nm-sized metal particles. *Chem. Phys. Lett.* **452**, 285–288 (2008).

93. Railsback, J. G., Johnston-Peck, A. C., Wang, J. & Tracy, J. B. Size-Dependent Nanoscale Kirkendall Effect During the Oxidation of Nickel Nanoparticles. *ACS Nano* **4**, 1913–1920 (2010).

94. Ermoline, A. & Dreizin, E. L. Equations for the Cabrera-Mott kinetics of oxidation for spherical nanoparticles. *Chem. Phys. Lett.* **505**, 47–50 (2011).

95. Carter, R. E. Kinetic Model for Solid-State Reactions. *J. Chem. Phys.* **34**, 2010–2015 (1961).

96. Shimada, E., Yamashita, H., Matsumoto, S., Ikuma, Y. & Ichimura, H. Oxidation kinetics of spherically shaped palladium powder. *J. Mater. Sci.* **34**, 4011–4015 (1999).

97. Peterson, N. L. & Wiley, C. L. Diffusion and point defects in Cu2O. *J. Phys. Chem. Solids* **45**, 281–294 (1984).

98. Moore, W. J., Ebisuzaki, Y. & Sluss, J. A. Exchange and diffusion of oxygen in crystalline cuprous oxide. *J. Phys. Chem.* **62**, 1438–1441 (1958).

99. Yin, Y. *et al.* Formation of Hollow Nanocrystals Through the Nanoscale Kirkendall Effect. *Science (80-.).* **304**, 711–714 (2004).

100. Sun, Y. *et al.* Quantitative 3D evolution of colloidal nanoparticle oxidation in solution. *Science (80-.).* **356**, 303–307 (2017).

101. Cabot, A. *et al.* Vacancy coalescence during oxidation of iron nanoparticles. *J. Am. Chem. Soc.* **129**, 10358–10360 (2007).

102. Nakamura, R., Lee, J.-G., Mori, H. & Nakajima, H. Oxidation behaviour of Ni nanoparticles and formation process of hollow NiO. *Philos. Mag.* **88**, 257–264 (2008).

103. Tokozakura, D., Nakamura, R., Nakajima, H., Lee, J.-G. & Mori, H. Transmission electron microscopy observation of oxide layer growth on Cu nanoparticles and formation process of hollow oxide particles. *J. Mater. Res.* **22**, 2930–2935 (2007).

104. Fan, H. J., Gösele, U. & Zacharias, M. Formation of Nanotubes and Hollow Nanoparticles Based on Kirkendall and Diffusion Processes: A Review. *Small* **3**, 1660–1671 (2007).

105. El Mel, A.-A. *et al.* Highly ordered hollow oxide nanostructures: the Kirkendall effect at the nanoscale. *Small* **9**, 2838–43 (2013).

106. Wang, W., Dahl, M. & Yin, Y. Hollow Nanocrystals through the Nanoscale Kirkendall Effect. *Chem. Mater.* **25**, 1179–1189 (2013).

107. Anderson, B. D. & Tracy, J. B. Nanoparticle conversion chemistry: Kirkendall effect, galvanic exchange, and anion exchange. *Nanoscale* **6**, (2014).

108. Muzzio, M. *et al.* Monodisperse nanoparticles for catalysis and nanomedicine. *Nanoscale* **11**, 18946–18967 (2019).

109. Huang, C.-L., Weng, W.-L., Liao, C.-N. & Tu, K. N. Suppression of interdiffusion-induced voiding in oxidation of copper nanowires with twin-modified surface. *Nat. Commun.* **9**, 340 (2018).

110. Susman, M. D., Feldman, Y., Bendikov, T. A., Vaskevich, A. & Rubinstein, I. Real-time plasmon spectroscopy study of the solid-state oxidation and Kirkendall void formation in copper nanoparticles. *Nanoscale* **9**, 12573–12589 (2017).

111. Albinsson, D., Nilsson, S., Antosiewicz, T. J., Zhdanov, V. P. & Langhammer, C. Heterodimers for in Situ Plasmonic Spectroscopy: Cu Nanoparticle Oxidation Kinetics, Kirkendall Effect, and Compensation in the Arrhenius Parameters. *J. Phys. Chem. C* **123**, 6284–6293 (2019).

112. Nakamura, R., Tokozakura, D., Nakajima, H., Lee, J.-G. & Mori, H. Hollow oxide formation by oxidation of Al and Cu nanoparticles. *J. Appl. Phys.* **101**, 074303 (2007).

113. Rice, K. P., Paterson, A. S. & Stoykovich, M. P. Nanoscale Kirkendall Effect and Oxidation Kinetics in Copper Nanocrystals Characterized by Real-Time, In Situ Optical Spectroscopy. *Part. Part. Syst. Charact.* **32**, 373–380 (2015).

114. Lee, J.-G., Nakamura, R., Choi, Y.-S., Yu, J.-H. & Choi, C.-J. Formation of Hollow Copper Oxide by Oxidation of Cu Nanoparticles. *Curr. Nanosci.* **10**, 101–103 (2014).

115. LaGrow, A. P., Ward, M. R., Lloyd, D. C., Gai, P. L. & Boyes, E. D. Visualizing the Cu/Cu2O Interface Transition in Nanoparticles with Environmental Scanning Transmission Electron Microscopy. *J. Am. Chem. Soc.* **139**, 179–185 (2017).

116. Zhdanov, V. P. Kinetic model of oxidation of metal nanoparticles: Cabrera-Mott and Kirkendall effects. *Surf. Sci.* **684**, 24–27 (2019).

117. Susman, M. D., Vaskevich, A. & Rubinstein, I. A General Kinetic-Optical Model for Solid-State Reactions Involving the Nano Kirkendall Effect. The Case of Copper Nanoparticle Oxidation. *J. Phys. Chem. C* **120**, 16140–16152 (2016).

118. Schwarz, R. B. & Khachaturyan, A. G. Thermodynamics of open two-phase systems with coherent interfaces: Application to metal-hydrogen systems. *Acta Mater.* **54**, 313–323 (2006).

119. Wadell, C. *et al.* Hysteresis-Free Nanoplasmonic Pd–Au Alloy Hydrogen Sensors. *Nano Lett.* **15**, 3563–3570 (2015).

120. Nugroho, F. A. A., Darmadi, I., Zhdanov, V. P. & Langhammer, C. Universal Scaling and Design Rules of Hydrogen-Induced Optical Properties in Pd and Pd-Alloy Nanoparticles. *ACS Nano* **12**, 9903–9912 (2018).

121. Mütschele, T. & Kirchheim, R. Segregation and diffusion of hydrogen in grain boundaries of palladium. *Scr. Metall.* **21**, 135–140 (1987).

122. Fechete, I., Wang, Y. & Védrine, J. C. The past, present and future of heterogeneous catalysis. *Catal. Today* **189**, 2–27 (2012).

123. Berzelius, J. J. *Årsberättelsen om framsteg i fysik och kemi*. (1835).

124. Lindström, B. & Pettersson, L. J. A brief history of catalysis. *CATTech* **7**, 130–138 (2003).

125. Wisniak, J. The History of Catalysis. From the Beginning to Nobel Prizes. *Educ. Quim.* **21**, 60–69 (2010).

126. Royer, S. & Duprez, D. Catalytic Oxidation of Carbon Monoxide over Transition Metal Oxides. *ChemCatChem* **3**, 24–65 (2011).

127. Zhang, Z. *et al.* The most active Cu facet for low-temperature water gas shift reaction. *Nat. Commun.* **8**, 1–10 (2017).

128. Twigg, M. V. & Spencer, M. S. Deactivation of Copper Metal Catalysts for Methanol Decomposition, Methanol Steam Reforming and Methanol Synthesis. *Top. Catal.* **22**, 191–203 (2003).

129. Kuld, S. *et al.* Quantifying the promotion of Cu catalysts by ZnO for methanol synthesis. *Science (80-.).* **352**, (2016).

130. van den Berg, R. *et al.* Structure sensitivity of Cu and CuZn catalysts relevant to industrial methanol synthesis. *Nat. Commun.* **7**, 13057 (2016).

131. Behrens, M. *et al.* The active site of methanol synthesis over Cu/ZnO/Al2O 3 industrial catalysts. *Science (80-.).* **336**, 893–897 (2012).

132. Bu, Y., Niemantsverdriet, J. W. H. & Fredriksson, H. O. A. Cu Model Catalyst Dynamics and CO Oxidation Kinetics Studied by Simultaneous in Situ UV-Vis and Mass Spectroscopy. *ACS Catal.* **6**, 2867–2876 (2016).

133. Huang, T. J. & Tsai, D. H. CO oxidation behavior of copper and copper oxides. *Catal. Letters* **87**, 173–178 (2003).

134. Eren, B., Heine, C., Bluhm, H., Somorjai, G. A. & Salmeron, M. Catalyst Chemical State during CO Oxidation Reaction on Cu(111) Studied with Ambient-Pressure X-ray Photoelectron Spectroscopy and Near Edge X-ray Adsorption Fine Structure Spectroscopy. *J. Am. Chem. Soc.* **137**, 11186–11190 (2015).

135. Eren, B. *et al.* Activation of Cu(111) surface by decomposition into nanoclusters driven by CO adsorption. *Science (80-.).* **351**, 475–478 (2016).

136. Roiaz, M. *et al.* Roughening of Copper (100) at Elevated CO Pressure: Cu Adatom and Cluster Formation Enable CO Dissociation. *J. Phys. Chem. C* **123**, 8112–8121 (2019).

137. Luo, L. *et al.* Real-Time Atomic-Scale Visualization of Reversible Copper Surface Activation during the CO Oxidation Reaction. *Angew. Chemie Int. Ed.* **59**, 2505–2509 (2020).

138. Xu, F. *et al.* Redox-mediated reconstruction of copper during carbon monoxide oxidation. *J. Phys. Chem. C* **118**, 15902–15909 (2014).

139. Zhdanov, V. P. & Kasemo, B. Simulation of kinetic oscillations in the CO+O2/Pt reaction on the nm scale. *J. Catal.* **214**, 121–129 (2003).

140. Wu, L. N., Tian, Z. Y. & Qin, W. Mechanism of CO Oxidation on Cu2O (111) Surface: A DFT and Microkinetic Study. *Int. J. Chem. Kinet.* **50**, 507–514 (2018).

141. Wang, X., Ye, J., Zhang, L., Bu, Y. & Sun, W. Strain engineering to tune the performance of CO oxidation on Cu2O(1 1 1) surface: A theoretical study. *Appl. Surf. Sci.* **540**, 148331 (2021).

142. Freestone, I., Meeks, N., Sax, M. & Higgitt, C. The Lycurgus Cup — A Roman nanotechnology. *Gold Bull.* **40**, 270–277 (2007).

143. The British Museum. Available at: www.britishmuseum.org. (Accessed: 21st March 2019)

144. Maier, S. A. *Plasmonics: Fundamentals and Applications*. (Springer US, 2007).

145. Mayer, K. M. & Hafner, J. H. Localized Surface Plasmon Resonance Sensors. *Chem. Rev.* **111**, 3828–3857 (2011).

146. Mie, G. Beiträge zur Optik trüber Medien, speziell kolloidaler Metallösungen. *Ann. Phys.* **330**, 377–445 (1908).

147. Kreibig, U. & Vollmer, M. *Optical properties of metal clusters*. (Springer, 1995).

148. Johnson, P. B. & Christy, R. W. Optical constants of the noble metals. *Phys. Rev. B* **6**, 4370–4379 (1972).

149. Johnson, P. B. & Christy, R. W. Optical constants of transition metals: Ti, V, Cr, Mn, Fe, Co, Ni, and Pd. *Phys. Rev. B* **9**, 5056–5070 (1974).

150. McPeak, K. M. *et al.* Plasmonic Films Can Easily Be Better: Rules and Recipes. *ACS Photonics* **2**, 326–333 (2015).

151. Chen, K. P., Drachev, V. P., Borneman, J. D., Kildishev, A. V. & Shalaev, V. M. Drude relaxation rate in grained gold nanoantennas. *Nano Lett.* **10**, 916–922 (2010).

152. Nagpal, P., Lindquist, N. C., Oh, S.-H. & Norris, D. J. Ultrasmooth Patterend Metals for Plasmonics and Metamaterials. *Science (80-.).* **325**, 594–597 (2009).

153. Ringe, E. *et al.* Plasmon length: A universal parameter to describe size effects in gold nanoparticles. *J. Phys. Chem. Lett.* **3**, 1479–1483 (2012).

154. Mock, J. J., Barbic, M., Smith, D. R., Schultz, D. A. & Schultz, S. Shape effects in plasmon resonance of individual colloidal silver nanoparticles. *J. Chem. Phys.* **116**, 6755–6759 (2002).

155. Lopez, G. A., Estevez, M. C., Soler, M. & Lechuga, L. M. Recent advances in nanoplasmonic biosensors: Applications and lab-on-a-chip integration. *Nanophotonics* **6**, 123–136 (2017).

156. Taylor, A. B. & Zijlstra, P. Single-Molecule Plasmon Sensing: Current Status and Future Prospects. *ACS Sensors* **2**, 1103–1122 (2017).

157. Hecht, B. *et al.* Scanning near-field optical microscopy with aperture probes: Fundamentals and applications. *J. Chem. Phys.* **112**, 7761–7774 (2000).

158. Tanaka, Y. *et al.* Direct imaging of nanogap-mode plasmon-resonant fields. *Opt. Express* **19**, 7726–7733 (2011).

159. Ringe, E., Sharma, B., Henry, A. I., Marks, L. D. & Van Duyne, R. P. Single nanoparticle plasmonics. *Physical Chemistry Chemical Physics* **15**, 4110–4129 (2013).

160. Cinchetti, M. *et al.* Photoemission electron microscopy as a tool for the investigation of optical near fields. *Phys. Rev. Lett.* **95**, 047601 (2005).

161. Gómez-Medina, R., Yamamoto, N., Nakano, M. & García de Abajo, F. J. Mapping plasmons in nanoantennas via cathodoluminescence. *New J. Phys.* **10**, 105009 (2008).

162. Kuttge, M. *et al.* Loss mechanisms of surface plasmon polaritons on gold probed by cathodoluminescence imaging spectroscopy. *Appl. Phys. Lett.* **93**, 113110 (2008).

163. Colliex, C., Kociak, M. & Stéphan, O. Electron Energy Loss Spectroscopy imaging of surface plasmons at the nanometer scale. *Ultramicroscopy* **162**, A1–A24 (2016).

164. García De Abajo, F. J. & Kociak, M. Probing the photonic local density of states with electron energy loss spectroscopy. *Phys. Rev. Lett.* **100**, 106804 (2008).

165. Boyer, D., Tamarat, P., Maali, A., Lounis, B. & Orrit, M. Photothermal Imaging of Nanometer-Sized Metal Particles Among Scatterers. *Science2* **297**, 1160–1163 (2002).

166. Kumar, C. S. S. R. (Challa S. S. R. . *Raman spectroscopy for nanomaterials characterization*. (Springer, 2012).

167. Kleinman, S. L., Frontiera, R. R., Henry, A. I., Dieringer, J. A. & Van Duyne, R. P. Creating, characterizing, and controlling chemistry with SERS hot spots. *Physical Chemistry Chemical Physics* **15**, 21–36 (2013).

168. George H. Chan, Jing Zhao, Erin M. Hicks, Schatz, G. C. & Duyne, R. P. Van. Plasmonic Properties of Copper Nanoparticles Fabricated by Nanosphere Lithography. *Nano Lett.* **7**, 1947–1952 (2007).

169. Langhammer, C., Yuan, Z., Zorić, I. & Kasemo, B. Plasmonic Properties of Supported Pt and Pd Nanostructures. *Nano Lett.* **6**, 833–838 (2006).

170. Langhammer, C., Schwind, M., Kasemo, B. & Zorić, I. Localized Surface Plasmon Resonances in Aluminum Nanodisks. *Nano Lett.* **8**, 1461–1471 (2008).

171. Biggins, J. S., Yazdi, S. & Ringe, E. Magnesium Nanoparticle Plasmonics. *Nano Lett.* **18**, 3752–3758 (2018).

172. Langhammer, C., Zorić, I., Kasemo, B. & Clemens, B. M. Hydrogen Storage in Pd Nanodisks Characterized with a Novel Nanoplasmonic Sensing Scheme. *Nano Lett.* **7**, 3122–3127 (2007).

173. Nugroho, F. A. A. *et al.* Metal–polymer hybrid nanomaterials for plasmonic ultrafast hydrogen detection. *Nat. Mater.* 1 (2019).

174. Darmadi, I., Nugroho, F. A. A., Kadkhodazadeh, S., Wagner, J. B. & Langhammer, C. Rationally Designed PdAuCu Ternary Alloy Nanoparticles for Intrinsically Deactivation-Resistant Ultrafast Plasmonic Hydrogen Sensing. *ACS Sensors* **4**, 1424–1432 (2019).

175. Rice, K. P., Walker, E. J., Stoykovich, M. P. & Saunders, A. E. Solvent-Dependent Surface Plasmon Response and Oxidation of Copper Nanocrystals. *J. Phys. Chem. C* **115**, 1793–1799 (2011).

176. Syrenova, S. *et al.* Hydride formation thermodynamics and hysteresis in individual Pd nanocrystals with different size and shape. *Nat. Mater.* **14**, 1236–1244 (2015).

177. Liu, S. *et al. In Situ* Plasmonic Nanospectroscopy of the CO Oxidation Reaction over Single Pt Nanoparticles. *ACS Nano* **13**, 6090–6100 (2019).

178. Albinsson, D. *et al.* Shedding Light on CO Oxidation Surface Chemistry on Single Pt Catalyst Nanoparticles Inside a Nanofluidic Model Pore. *ACS Catal.* **11**, 2021–2033 (2021).

179. Zeng, Z., Liu, Y. & Wei, J. Recent advances in surface-enhanced raman spectroscopy (SERS): Finite-difference time-domain (FDTD) method for SERS and sensing applications. *TrAC - Trends in Analytical Chemistry* **75**, 162–173 (2016).

180. Yang, W. H., Schatz, G. C. & Van Duyne, R. P. Discrete dipole approximation for calculating extinction and Raman intensities for small particles with arbitrary shapes. *J. Chem. Phys.* **103**, 869–875 (1995).

181. Draine, B. T. & Flatau, P. J. Discrete-Dipole Approximation For Scattering Calculations. *J. Opt. Soc. Am. A* **11**, 1491 (1994).

182. Taflove, A., Hagness, S. C. & Piket-May, M. Computational electrodynamics: the finite-difference time-domain method. in *The Electrical Engineering Handbook* (ed. Chen, W.-K.) 629–670 (Elsevier, 2013).

183. Brock, D. C. & Moore, G. E. Understanding Moore's law : four decades of innovation. in *Understanding Moore's law : four decades of innovation* 122 (Chemical Heritage Foundation, 2006).

184. Feynman, R. P. There's plenty of room at the bottom [data storage]. *J. Microelectromechanical Syst.* **1**, 60–66 (1992).

185. Lambert, L. & Mulvey, T. Ernst Ruska (1906–1988), Designer Extraordinaire of the Electron Microscope: A Memoir. *Adv. Imaging Electron Phys.* **95**, 2–62 (1996).

186. Binnig, G. & Rohrer, H. Scanning tunneling microscopy. *IBM J. Res. Dev.* **44**, 279–293 (2000).

187. Fredriksson, H. *et al.* Hole–Mask Colloidal Lithography. *Adv. Mater.* **19**, 4297–4302 (2007).

188. Nugroho, F. A. A., Albinsson, D., Antosiewicz, T. J. & Langhammer, C. Plasmonic Metasurface for Spatially Resolved Optical Sensing in Three Dimensions. *ACS Nano* **14**, 2345–2353 (2020).

189. Syrenova, S., Wadell, C. & Langhammer, C. Shrinking-Hole Colloidal Lithography: Self-Aligned Nanofabrication of Complex Plasmonic Nanoantennas. *Nano Lett.* **14**, 2655–2663 (2014).

190. Susarrey-Arce, A. *et al.* A nanofabricated plasmonic core-shell-nanoparticle library. *Nanoscale* **11**, 21207–21217 (2019).

191. Cheng, X. Nanostructures: fabrication and applications. *Nanolithography* 348–375 (2014).

192. Tseng, A. A. *Nanofabrication: Fundamentals and Applications*. (WORLD SCIENTIFIC, 2008).

193. Fritzsche, J. *et al.* Single Particle Nanoplasmonic Sensing in Individual Nanofluidic Channels. *Nano Lett.* **16**, 7857–7864 (2016).

194. Grant, A. W., Hu, Q.-H. & Kasemo, B. Transmission electron microscopy windows for nanofabricated structures. *Nanotechnology* **15**, 1175–1181 (2004).

195. Nguyen, N.-T. & Nguyen, N.-T. Fabrication technologies. *Micromixers* 113–161 (2012).

196. Shibata, N. *et al.* Electric field imaging of single atoms. *Nat. Commun.* **8**, 1–7 (2017).

197. Boyes, E. D., Ward, M. R., Lari, L. & Gai, P. L. ESTEM imaging of single atoms under controlled temperature and gas environment conditions in catalyst reaction studies. *Ann. Phys.* **525**, 423–429 (2013).

198. Meyer, J. C., Girit, C. O., Crommie, M. F. & Zettl, A. Imaging and dynamics of light atoms and molecules on graphene. *Nature* **454**, 319–322 (2008).

199. Kirchner, S. R. *et al.* Snapshot Hyperspectral Imaging (SHI) for Revealing Irreversible and Heterogeneous Plasmonic Processes. *J. Phys. Chem. C* **122**, 6865–6875 (2018).

200. Wang, H., Zhang, T. & Zhou, X. Dark-field spectroscopy: development, applications and perspectives in single nanoparticle catalysis. *J. Phys. Condens. Matter* **31**, 473001 (2019).

201. Pini, V. *et al.* Spatially multiplexed dark-field microspectrophotometry for nanoplasmonics. *Sci. Rep.* **6**, 1–10 (2016).

202. Zopf, D. *et al.* Hyperspectral imaging of plasmon resonances in metallic nanoparticles. *Biosens. Bioelectron.* **81**, 287–293 (2016).

203. Williams, D. B. & Carter, C. B. *Transmission Electron Microscope*. *Transmission Electron Microscopy* (Springer US, 2009).

204. Kirkland, A. I. & Haigh, S. J. *Nanocharacterisation*. (Royal Society of Chemistry, 2015).

205. Egerton, R. F. *Physical Principles of Electron Microscopy*. (Springer International Publishing, 2016).

206. Yu, Z., Muller, D. A. & Silcox, J. Study of strain fields at a-Si/c-Si interface. *J. Appl. Phys.* **95**, 3362–3371 (2004).

207. Tanaka, N. *Electron Nano-Imaging*. (Springer Japan, 2017).

208. Smith, D. J. Characterization of nanomaterials using transmission electron microscopy. in *Nanocharacterisation* (eds. Kirkland, A. I. & Haigh, S. J.) 1–29 (Royal Society of Chemistry, 2015).

209. Ngantcha, J. P., Gerland, M., Kihn, Y. & Riviere, A. Correlation between microstructure and mechanical spectroscopy of a Cu-Cu2O alloy between 290K and 873K. *Eur. Phys. J. Appl. Phys.* **29**, 83–89 (2005).

210. Su, D. Advanced electron microscopy characterization of nanomaterials for catalysis. *Green Energy and Environment* **2**, 70–83 (2017).

211. Yu, Q., Legros, M. & Minor, A. M. In situ TEM nanomechanics. *MRS Bulletin* **40**, 62–68 (2015).

212. Creemer, J. F. *et al.* Atomic-scale electron microscopy at ambient pressure. *Ultramicroscopy* **108**, 993–998 (2008).

213. Erdman, N. & Bell, D. C. Scanning electron and ion microscopy of nanostructures. in *Nanocharacterisation* (eds. Kirkland, A. I. & Haigh, S. J.) 300–350 (Royal Society of Chemistry, 2015).

214. Sneddon, G. C., Trimby, P. W. & Cairney, J. M. Transmission Kikuchi diffraction in a scanning electron microscope: A review. *Materials Science and Engineering R: Reports* **110**, 1–12 (2016).

215. Egerton, R. F., Li, P. & Malac, M. Radiation damage in the TEM and SEM. *Micron* **35**, 399–409 (2004).

216. Li, J. & Liu, C. Carbon-coated copper nanoparticles: synthesis, characterization and optical properties. *New J. Chem.* **33**, 1474 (2009).

217. Cure, J. *et al.* Remarkable Decrease in the Oxidation Rate of Cu Nanocrystals Controlled by Alkylamine Ligands. *J. Phys. Chem. C* **121**, 5253–5260 (2017).

218. Coker A.Kayode. Appendix C: Physical Properties of Liquids and Gases. in *Ludwig's Applied Process Design for Chemical and Petrochemical Plants* (Elsevier, 2007).

219. Yang, L., Yan, B. & Reinhard, B. M. Correlated Optical Spectroscopy and Transmission Electron Microscopy of Individual Hollow Nanoparticles and their Dimers. *J. Phys. Chem. C* **112**, 15989–15996 (2008).

220. Henry, A.-I. *et al.* Correlated Structure and Optical Property Studies of Plasmonic Nanoparticles. *J. Phys. Chem. C* **115**, 9291–9305 (2011).

221. Pratt, A. *et al.* Enhanced oxidation of nanoparticles through strain-mediated ionic transport. *Nat. Mater.* **13**, 26–30 (2014).

222. Nilsson Pingel, T., Jørgensen, M., Yankovich, A. B., Grönbeck, H. & Olsson, E. Influence of atomic site-specific strain on catalytic activity of supported nanoparticles. *Nat. Commun.* **9**, 1–9 (2018).

223. Mutz, B., Carvalho, H. W. P., Mangold, S., Kleist, W. & Grunwaldt, J.-D. Methanation of CO2: Structural response of a Ni-based catalyst under fluctuating reaction conditions unraveled by operando spectroscopy. *J. Catal.* **327**, 48–53 (2015).

224. Pu, T., Tian, H., Ford, M. E., Rangarajan, S. & Wachs, I. E. Overview of Selective Oxidation of Ethylene to Ethylene Oxide by Ag Catalysts. *ACS Catal.* 10727–10750 (2019).